



HAL
open science

Photoacoustic imaging: contributions to optical-resolution photoacoustic endoscopy and experimental investigation of thermal nonlinearity

Olivier Simandoux

► **To cite this version:**

Olivier Simandoux. Photoacoustic imaging: contributions to optical-resolution photoacoustic endoscopy and experimental investigation of thermal nonlinearity. Physics [physics]. Université Paris Diderot Paris 7, 2015. English. NNT: . tel-01121119

HAL Id: tel-01121119

<https://hal.science/tel-01121119>

Submitted on 27 Feb 2015

HAL is a multi-disciplinary open access archive for the deposit and dissemination of scientific research documents, whether they are published or not. The documents may come from teaching and research institutions in France or abroad, or from public or private research centers.

L'archive ouverte pluridisciplinaire **HAL**, est destinée au dépôt et à la diffusion de documents scientifiques de niveau recherche, publiés ou non, émanant des établissements d'enseignement et de recherche français ou étrangers, des laboratoires publics ou privés.

**THÈSE DE DOCTORAT DE L'UNIVERSITÉ PARIS.DIDEROT
(Paris 7) SORBONNE PARIS CITÉ**

Spécialité

**Matière condensée et interfaces
ED 564 - Physique en Île-de-France**

Préparée à l'INSTITUT LANGEVIN - ONDES ET IMAGES

Présentée par

Olivier SIMANDOUX

Pour obtenir le grade de

DOCTEUR de l'UNIVERSITÉ PARIS 7

Sujet de la thèse :

**Photoacoustic imaging:
contributions to optical-resolution photoacoustic
endoscopy and experimental investigation of thermal
nonlinearity**

Soutenue le 14 janvier 2015

Devant le jury composé de :

Pr. BEARD	Paul	Rapporteur
Dr. BOSSY	Emmanuel	Directeur de thèse
Pr. CLEVELAND	Robin	Rapporteur
Pr. DERODE	Arnaud	Examineur
Pr. MOSER	Christophe	Examineur

Remerciements

Ces trois années de thèse ont été pour moi une très belle aventure aussi bien scientifique qu'humaine grâce à l'excellente ambiance qui règne à l'Institut Langevin ainsi qu'à la qualité et la diversité des recherches qui y sont effectuées. Je remercie la direction générale de l'armement de m'avoir fait confiance et permis par son financement de réaliser cette thèse.

Je remercie tout d'abord mon directeur de thèse, Emmanuel Bossy, rencontré lors d'un cours puis d'un examen à l'ESPCI sur l'imagerie médicale. Sa pédagogie, sa rigueur et ses grandes qualités scientifiques et humaines qui m'avaient poussé à faire une thèse avec lui ne se sont pas démenties au cours de ce travail de recherche et j'espère m'inspireront. J'ai particulièrement apprécié de travailler avec lui et je le remercie chaleureusement pour tout ce qu'il m'a appris, les sujets passionnants et originaux sur lesquels il m'a permis de travailler, sa bienveillance et toute l'aide qu'il m'a apportée jusqu'à la fin de la thèse.

J'aimerais également remercier les professeurs Paul Beard et Robin Cleveland pour le temps qu'ils ont pris pour rapporter mon manuscrit et venir assister à ma soutenance de thèse depuis l'Angleterre, ainsi que les professeurs Christophe Moser et Arnaud Derode pour avoir accepté de faire partie de mon jury de thèse.

Une partie des travaux présentés dans ce manuscrit sont le fruit d'une collaboration fructueuse avec les professeurs Demetri Psaltis et Christophe Moser, les docteurs Salma Farahi et Ioannis Papadopoulos, Nicolino Stasio qui est encore en thèse, et Jean-Pierre Huignard qui a été à l'origine de cette collaboration. Je les remercie tous pour les très bons moments que j'ai passés à Lausanne, dans et hors du laboratoire, grâce à l'accueil particulièrement chaleureux qui m'y a toujours été réservé.

Je remercie Olivier, Claire, Ros, Juliette, Rémi, Romain et Baptiste au laboratoire qui ont pris le temps de répondre à mes plus ou moins nombreuses questions de physique

chacun dans des domaines bien différents. Mon travail de recherche et mes nombreux voyages professionnels à l'étranger n'auraient également pas pu se dérouler de manière aussi favorable sans l'aide précieuse de personnes essentielles au laboratoire : Patricia, Emmanuel, Lorraine, Christelle, Khadija, Laurine, Khadija et Abdelhak.

Je remercie également toute l'équipe de photoacoustique. Tout d'abord Amaury avec qui j'ai partagé bureau, salle de manip et débats sur tout un ensemble de sujets à des heures plus ou moins avancées du jour ou de la nuit, ainsi que d'excellents moments en conférence à Munich et Prague par exemple. Jérôme, l'expert en photoacoustique et imagerie médicale à qui j'ai posé d'innombrables questions auxquelles il a toujours répondu avec bonne humeur. Ma thèse a largement bénéficié de son aide précieuse, ses commentaires et de la vision nouvelle de la photoacoustique qu'il a apportée à l'équipe. Florian, toujours disponible, avec qui j'ai pris un grand plaisir à discuter de photoacoustique, de physique, mais surtout du reste, et qui m'a bien aidé lors de la rédaction pour certaines expériences. Mickael et Tanguy pour leur aide sur les expériences lors de leurs stages. Thomas, qui fait également partie d'une autre équipe mais qui travaille aussi sur la photoacoustique et avec qui j'ai passé de très bons moments en conférence et en soirée, et qui a pris le temps de répondre à toutes mes questions concernant le façonnage de front d'onde.

Je remercie tous mes voisins de bureaux : Aniss, l'expert en Matlab, Mickael, l'aventurier, Amaury, le photoacousticien, Daria, la partenaire de voyage italienne, Ariadna, la danseuse catalane, Maxime, le petit nouveau, Jérôme, le capoeiriste, Nicolas, le sage, Benoit, le littéraire, Ibrahim, le supporter du Bayern de Munich, et Bastien, le PCéen. Je n'oublie pas non plus ceux des bureaux voisins : Marc, Fabien, Pierre, Amir, etc.

Un grand merci, à mes deux colocataires pendant 4 ans, qui sont toutes les deux devenues docteurs avant moi, pour les excellents moments passés ensemble.

Enfin, pour finir, merci à tous mes amis, à ma soeur et à ma mère dont le soutien et la présence sont inestimables, à toute ma famille, des plus jeunes aux moins jeunes, à Michel et Hervé qui m'ont fortement incité à faire une thèse, et à Sophie qui me remplit de joie.

Résumé

L'imagerie photoacoustique est une technique hybride qui permet d'obtenir à plusieurs centimètres de profondeur dans les tissus biologiques des images de l'absorption optique avec la résolution des ultrasons. Des agents de contraste peuvent être utilisés pour améliorer le contraste ou imager des récepteurs spécifiques de maladies, mais il existe un compromis entre résolution et profondeur d'imagerie. Cependant, la détection spécifique d'agents de contraste peut nécessiter l'utilisation de l'imagerie multispectrale qui reste un défi à cause de la propagation complexe de la lumière dans les tissus biologiques. Cette thèse propose une nouvelle approche pour la microscopie photoacoustique à résolution optique (OR-PAM) de l'ordre du micron à plusieurs centimètres de profondeur dans les tissus, et étudie expérimentalement la possibilité d'améliorer la détection de nanosphères d'or grâce à la non-linéarité photoacoustique d'origine thermique. Il est d'abord montré que des images OR-PAM peuvent être générées à l'extrémité distale d'une fibre optique multimode grâce à la conjugaison de phase numérique. Il est ensuite montré que des images OR-PAM peuvent être transmises à travers les tissus en les guidant acoustiquement dans un capillaire de silice. Des expériences préliminaires suggèrent que les deux approches précédentes pourraient être combinées pour acquérir des images OR-PAM à travers plusieurs centimètres de tissus via un unique capillaire de silice. Enfin, il est montré que des solutions aqueuses de colorant et de nanosphères d'or peuvent être discriminées grâce à la non-linéarité thermique et la dépendance de l'amplitude photoacoustique avec la fluence ou la température.

Mots-clés : imagerie photoacoustique, résolution optique, endoscopie photoacoustique, conjugaison de phase numérique, guide d'onde, nanoparticules d'or, non-linéarité d'origine thermique, coefficient de dilatation thermique

Abstract

Photoacoustic imaging is a new hybrid imaging technique that provides images of optical absorption at centimeters depth in biological tissues with the resolution of ultrasound. Exogenous contrast agents such as gold nanoparticles can also be used to enhance image contrast and image disease-specific receptors. However, there is a trade-off between resolution and imaging depth. Moreover, specific detection of exogenous contrast agents often requires the use of multispectral imaging which can be challenging because of the complex propagation of light in biological tissues. This thesis presents a new approach to micron-scale optical-resolution photoacoustic microscopy (OR-PAM) at centimeters depth based on a minimally-invasive endoscope, and experimentally investigates the possibility of improving gold nanospheres detection based on thermal nonlinear photoacoustic generation. It is first shown that OR-PAM images can be generated at the distal tip of a multimode fiber by use of digital phase conjugation. It is then shown that OR-PAM images can be transmitted through tissue in a silica-capillary acoustic waveguide for remote detection at the tissue surface. Preliminary experiments suggest that the two previous approaches could be combined in a setup based on a unique silica capillary acting both as an optical and an acoustic waveguide to acquire OR-PAM images at centimeters depth in tissues. Finally, it is shown that organic-dye and gold-nanospheres aqueous solutions can be discriminated thanks to thermal nonlinearity, based on the dependence of the photoacoustic amplitude with fluence or temperature.

Keywords: photoacoustic imaging, optical resolution, photoacoustic endoscopy, digital phase conjugation, waveguide, gold nanoparticles, thermal nonlinearity, thermal expansion coefficient

Contents

Introduction	viii
1 Background and objectives	1
1.1 Principles of photoacoustic imaging	2
1.1.1 Optical propagation in biological tissues	2
1.1.2 Basic theory of photoacoustic generation	7
1.1.3 Photoacoustics applied to imaging	16
1.1.4 Imaging setups	19
1.2 Structure and objectives of the thesis	22
1.2.1 New approaches in optical-resolution photoacoustic micro-endoscopy	22
1.2.2 Acoustic-resolution sensing and photoacoustic thermal nonlinearity	27
I Optical-resolution photoacoustic endoscopy	29
2 Photoacoustic excitation through a multimode fiber	30
2.1 Background and principles	31
2.1.1 Digital holography	31
2.1.2 Phase conjugation by use of an SLM	34
2.1.3 Focusing and scanning through a multimode fiber	38
2.1.4 Optical-resolution photoacoustic microscopy	42
2.2 Materials and methods	44
2.2.1 Experimental setup	44
2.2.2 Procedure	46
2.3 Results	47
2.3.1 Photoacoustic images	47

2.3.2	Estimation of the resolution	48
2.4	Conclusion	49
3	Photoacoustic sensing through a water-filled capillary	51
3.1	Background and principles	53
3.1.1	Acoustic attenuation	53
3.1.2	A silica capillary as an acoustic guide	57
3.2	Proof of principle	61
3.2.1	Materials and methods	61
3.2.2	Results	64
3.2.3	Conclusion	66
3.3	Some properties of the capillary as an acoustic waveguide	66
3.3.1	Materials and methods	67
3.3.2	Results	69
3.3.3	Discussion	73
3.4	Current work and perspectives	81
3.4.1	A silica capillary as an optical waveguide	81
3.4.2	Experimental Setup	84
3.4.3	Results	85
3.5	Conclusion	86
II	Acoustic-resolution photoacoustic sensing	89
4	Experimental setups for acoustic-resolution photoacoustic imaging	90
4.1	Raster-scanned focused transducer	91
4.1.1	Imaging system	91
4.1.2	Phantom images	93
4.2	Linear array probe and commercial ultrasound scanner	94
4.2.1	Imaging system	94
4.2.2	In vivo imaging of mice tumors after injection of gold nanoparticles	96
4.3	Conclusion	100
5	Experimental investigation of photoacoustic thermal nonlinearity	102
5.1	Background and principle	103

5.1.1	Photoacoustic generation by a gold nanosphere	103
5.1.2	Photoacoustic generation by a collection of gold nanospheres	109
5.2	Materials and methods	114
5.2.1	Experimental setup	114
5.2.2	Practical considerations	116
5.3	Results	118
5.3.1	Results as a function of fluence	118
5.3.2	Influence of the equilibrium temperature	120
5.4	Conclusion	121
Conclusion		123
A Publications and communications		127
A.1	Publications in international peer-reviewed journals	127
A.2	International conferences as speaker	127
A.3	International conferences as co-author	128
A.4	National conference as speaker	128
A.5	National conference, poster	129
Bibliography		130

Introduction

Medical imaging has become an essential tool in today's medicine. The most commonly used or effective techniques include ultrasonography, magnetic resonance imaging, X-ray based imaging and nuclear medicine imaging. Each of these techniques are used for specific applications and in specific contexts, providing different and potentially complementary information. Optical imaging can provide a precious new information, both anatomical and functional, with a strong contrast, in a non-ionizing way. The optical properties of biological tissues are indeed very dependent on the tissue type and the optical wavelengths (wavelengths that are on the order of several hundreds of nanometers to a micrometer). Optical imaging is however little used in medical imaging because of the strong optical scattering properties of biological tissues that limit high resolution imaging to shallow imaging depths. Indeed, optical imaging techniques that can provide resolution on the order of the wavelength, based on ballistic or quasi-ballistic photons, can only provide images at depths no greater than several hundred micrometers. Purely optical techniques based on diffuse photons enable to image deeper in biological tissues, up to a few centimeters, but with a resolution of the order of the imaging depth.

Photoacoustic imaging is a biomedical imaging technique introduced in the nineties, with the objective to improve the resolution of optical imaging at depth in biological tissue. Photoacoustic imaging relies on the photoacoustic effect, which was discovered in 1880 by Alexander Graham Bell and consists in the conversion of optical energy into acoustic energy through thermoelastic stress generation. Although photoacoustics was investigated for biomedical imaging only recently comparatively to its discovery, photoacoustic imaging has now become a very fast growing field of research [[Beard, 2011](#); [Wang and Hu, 2012](#)]. The sample is usually illuminated by a light pulse and the acoustic waves generated due to the photoacoustic effect in the optically absorbing illuminated regions of the sample are detected to form an image of the sample. The image contrast is predominantly based on

the optical absorption properties of the imaged sample. The light pulse used to illuminate the sample can either be tightly focused and scanned in the imaged region, to provide an image resolution that is on the order of the optical wavelength, or distributed on a large area of the imaged sample, in which case the resolution is dictated by acoustics. While the penetration depth of optical-resolution photoacoustic imaging is limited to about a few hundreds of micrometers, that of acoustic-resolution photoacoustic imaging depends in particular on the central frequency and the bandwidth of the acoustic detection device and can reach up to several centimeters with a depth-to-resolution ratio that is of the order of one hundred. Photoacoustic imaging can provide both structural and functional images, in a non-ionizing way, based on endogenous or exogenous absorbers, with the potential ability to achieve molecular imaging, at scales that range from the organelles to the organs through cells and tissues, and can be used in a wide variety of applications in both biology, pre-clinical research and clinical medicine [Beard, 2011; Wang and Hu, 2012].

The PhD work reported in this manuscript is presented in two independent parts, preceded by a first introductory chapter which provides both the fundamental principles of photoacoustic imaging and the objectives and structure of the thesis (chapter 1).

The first part deals with optical-resolution photoacoustic endoscopy. Phase conjugation is first used to generate an optical-resolution photoacoustic image at the distal tip of a multimode fiber (chapter 2). A water-filled capillary is then studied as a mean to transmit optical-resolution images through biological tissues (chapter 3).

The second part deals with acoustic-resolution photoacoustic sensing. Two acoustic-resolution photoacoustic imaging setups that were built are presented along with some images acquired on phantoms and living mice (chapter 4). Thermal based nonlinear photoacoustic generation phenomenon are then investigated experimentally using a modified version of one the previous chapter setups and the obtained results are compared with numerical simulation predictions of a recent PhD thesis of our group (chapter 5).

Chapter 1

Background and objectives

Contents

1.1 Principles of photoacoustic imaging	2
1.1.1 Optical propagation in biological tissues	2
1.1.2 Basic theory of photoacoustic generation	7
1.1.3 Photoacoustics applied to imaging	16
1.1.4 Imaging setups	19
1.2 Structure and objectives of the thesis	22
1.2.1 New approaches in optical-resolution photoacoustic micro-endoscopy	22
1.2.2 Acoustic-resolution sensing and photoacoustic thermal nonlinearity	27

Optical imaging of biological tissues can provide precious information. Unfortunately, traditional high resolution optical imaging techniques penetration depths are limited to only a few hundreds of micrometers because of the strong optical scattering properties of biological tissues. Photoacoustic imaging is a new hybrid imaging modality that has the ability to provide optical absorption-based contrast images at significant depths in biological tissues. Thanks to its unique advantages it has become one of the fastest growing field in biomedical imaging. The main objective of this chapter is to provide the essential information to understand the work presented later in this thesis. We first present the principles of photoacoustic imaging and then explain the structure and the objectives of this thesis.

1.1 Principles of photoacoustic imaging

1.1.1 Optical propagation in biological tissues

Optical propagation in biological tissue is usually described by a few parameters related to optical absorption and scattering properties, described in this section.

Optical absorption

Optical absorption is described by the optical absorption coefficient μ_a . If one considers a collimated beam propagating in a non scattering and homogeneously absorbing medium, the intensity of the collimated beam will decay along its propagation in the medium according to the following law:

$$I_c(z) = I_c(0)e^{-\mu_a z} \quad (1.1)$$

where $I_c(z)$ is the intensity of the collimated beam at position z along its propagation axis, expressed in power per unit surface, and μ_a is the absorption coefficient expressed per unit

length.

The following equivalent law is also often used:

$$I_c(z) = I_c(0)10^{-ODz} \quad (1.2)$$

where OD is the optical density, usually expressed in cm^{-1} , and related to the absorption coefficient μ_a by:

$$OD = \frac{\mu_a}{\ln(10)} \approx \frac{\mu_a}{2.3} \quad (1.3)$$

Based on equation 1.1 one can define a characteristic length $l_a = \frac{1}{\mu_a}$ called the optical absorption mean free path.

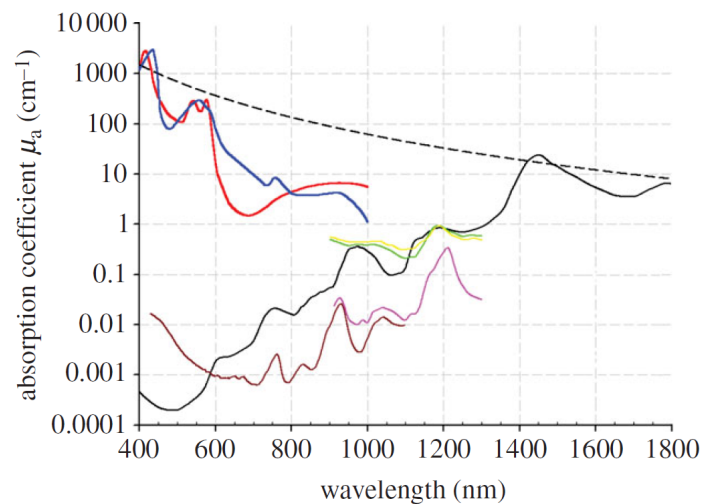


Figure 1.1 – Optical absorption coefficient spectra of endogenous tissue chromophores. Oxyhaemoglobin (HbO_2) at 150 g L^{-1} (average haemoglobin concentration in an adult man), red line; deoxyhaemoglobin (HHb) at 150 g L^{-1} , blue line; water, black line; lipids, brown and pink lines; melanin, black dashed line; collagen, green line and elastin, green line. Compilation from the literature. Taken from [Beard, 2011].

As can be seen on figure 1.1 optical absorption in biological tissues is highly dependent on the tissue type and the optical wavelength. It is however usually considered to be minimum in the so-called optical or therapeutic window ranging from about 600 to 900 nm. In this spectral domain, the optical absorption coefficient in biological tissues is on the order of 0.1 cm^{-1} . This corresponds to an absorption mean free path of about 100 mm.

Optical scattering

Optical scattering is described by the optical scattering coefficient μ_s . If one considers a collimated beam propagating in a non absorbing and homogeneously scattering medium, the intensity of the collimated beam will decay along its propagation in the medium according to the following law:

$$I_c(z) = I_c(0)e^{-\mu_s z} \quad (1.4)$$

where $I_c(z)$ is the intensity of the collimated beam at position z along its propagation axis, expressed in power per unit surface, and μ_s is the optical scattering coefficient expressed per unit length.

Based on equation 1.4 one can define a characteristic length $l_s = \frac{1}{\mu_s}$ called the optical scattering mean free path.

In biological tissues, the optical scattering coefficient is usually on the order of 100 cm^{-1} . This corresponds to an optical scattering mean free path of about 0.1 mm.

Optical scattering events are also described by the anisotropy factor g , defined as the average of the cosine of the scattering events angles θ :

$$g = \langle \cos(\theta) \rangle \quad (1.5)$$

If $g = 0$, the scattering is isotropic, while if g is close to 1, the scattering occurs mainly in the forward direction. In biological tissues, the value of g is typically about 0.9. To take into account both the optical scattering coefficient and the anisotropy factor, optical scattering is often described by the *reduced* optical scattering coefficient μ'_s :

$$\mu'_s = \mu_s(1 - g) \quad (1.6)$$

Based on this equation one can define the optical transport mean free path $l_{tr} = \frac{1}{\mu'_s} = \frac{l_s}{1-g}$. It can be qualitatively understood as the distance over which light loses the memory of its initial propagation direction. In biological tissues, μ'_s is typically about 10 cm^{-1} , and l_{tr} is thus typically about 1 mm.

Optical extinction

The optical extinction is defined as the total attenuation coefficient of a collimated beam, i.e. by $\mu_{ext} = \mu_a + \mu_s$. If one considers a collimated beam propagating in a homogeneously absorbing and scattering medium, the intensity of the collimated beam will decay along its propagation in the medium according to the following law:

$$I_c(z) = I_c(0)e^{-\mu_{ext}z} \quad (1.7)$$

where $I_c(z)$ is the intensity of the collimated beam at position z along its propagation axis, expressed in power per unit surface, and μ_{ext} is the optical extinction coefficient expressed per unit length.

Based on equation 1.7 one can define a characteristic length $l_s = \frac{1}{\mu_{ext}}$ called the optical extinction mean free path.

Effective optical attenuation of diffused light

For optical propagation in biological tissues at depth beyond several optical transport mean free path ($l_{tr} \approx 1$ mm), the intensity of an incident collimated beam becomes much smaller than that of the diffused light. The propagation of the diffuse light beyond typically one mean free path can be described by an effective optical attenuation coefficient $\mu_{eff} = \sqrt{3\mu_a(\mu_a + \mu'_s)}$ derived from the diffusion theory. For 1D propagation, the diffusive intensity decays according to the following law:

$$I(z) = I(0)e^{-\mu_{eff}z} \quad (1.8)$$

where $I(z)$ is the optical intensity at depth $z \gg l_{tr}$, expressed in power per unit surface, and μ_{eff} is the effective optical attenuation coefficient expressed per unit length.

Based on equation 1.8 one can define a characteristic length $l_{eff} = \frac{1}{\mu_{eff}}$. It is the length over which, in the diffusive regime, the intensity of an optical plane wave incident on the tissue has decay by $\frac{1}{e}$ and thus represents the optical penetration depth.

For near-infrared light in biological tissue, the optical scattering coefficient is usually on the order of 1.7 cm^{-1} . This corresponds to an optical penetration depth of about 6 mm.

Consequences on optical imaging of biological tissue

Two important remarks can be made based on the coefficients introduced above. First, optical propagation at depth in biological tissues is dominated by optical scattering as can be seen from the values of the scattering coefficients μ_s and μ'_s as compared to that of the optical absorption coefficient μ_a . As the penetration depth increases, there is a progressive transition from a ballistic optical propagation regime in the first hundred microns to a diffusive optical propagation regime beyond typically one millimeter.

Second, two different depth limits can be defined for optical imaging of biological tissues. The first one, about one optical transport mean free path ($l_{tr} \approx 1$ mm), is related to the attenuation of the ballistic or quasi-ballistic photons. High resolution optical imaging of biological tissues based on these photons, for example by use of confocal microscopy, two-photon microscopy, or optical coherence tomography, is only possible at depths below this first limit, sometimes referred to as the soft limit for high resolution optical imaging. The second one, about ten times the optical penetration depth $l_{eff} \approx 5.7$ mm, thus about 60 mm, is related to the attenuation of the diffuse light. Optical imaging up to such depths in biological tissues is possible by use of diffuse optical tomography but with resolutions still limited to at least several millimeters. Optical imaging beyond this second limit, sometimes referred to as the hard limit of optical imaging, is only possible by use of endoscopy because of the extremely low number of photons that can propagate up to such depths.

High resolution optical contrast images of biological tissues at significant depths up to or beyond the hard limit of optical imaging are highly desirable because of the precious information optical contrast images can provide about biological tissues. Photoacoustic imaging is an imaging modality that has been introduced to beat the resolution limit imposed for purely optical techniques by optical scattering. It is introduced in the following three sections, starting with the basic theory of the photoacoustic effect on which photoacoustic imaging is based in section 1.1.2, then explaining how it can be used for optical contrast imaging of biological tissues in section 1.1.3, and finally presenting the general principles underlying the practical implementation of photoacoustic imaging in section 1.1.4.

1.1.2 Basic theory of photoacoustic generation

The photoacoustic effect refers to the generation of acoustic waves in matter due to the absorption of electromagnetic waves. It was first observed by Alexander Graham Bell in 1880 [Bell, 1880]. In this section, we will limit our discussion to the photoacoustic effect taking place in liquids with potentially heterogeneous optical properties but homogeneous acoustic and thermal properties. This is justified by the fact that, as a first approximation, the thermal and acoustic properties of biological tissues can be modeled as being those of water.

Mathematical description

A mathematical description of the photoacoustic effect is given by the following set of equations:

$$\rho_0 c_p \frac{\partial T}{\partial t}(\mathbf{r}, t) = \kappa \Delta T(\mathbf{r}, t) + P_V(\mathbf{r}, t) \quad (1.9)$$

$$\Delta p(\mathbf{r}, t) - \frac{1}{c_s^2} \frac{\partial^2 p}{\partial t^2}(\mathbf{r}, t) = -\rho_0 \frac{\partial}{\partial t} \left(\beta(T) \frac{\partial T}{\partial t}(\mathbf{r}, t) \right) \quad (1.10)$$

where ρ_0 is the liquid volumetric mass density, c_p is the liquid heat capacity at constant pressure, $T(\mathbf{r}, t)$ is the temperature field in the liquid, κ is the liquid heat conductivity, P_v is a heat source term, $p(\mathbf{r}, t)$ is the pressure field in the liquid, c_s is the speed of sound in the liquid, and β is the liquid coefficient of thermal expansion at constant pressure.

The first equation is a heat diffusion equation with a heat source term and the second equation is an acoustic wave equation with an acoustic source term arising from time variations of the temperature field.

Before getting into the details of these equations, it is important to stress the conditions of their validity. These conditions can easily be seen by working on the fundamentals equations to establish equations 1.9 and 1.10. Such a derivation is out of the scope of this thesis but can be found for example in [Prost, 2014]. Equations 1.9 and 1.10 rely on the following approximations:

- $c_p \approx c_v$
- ρ_0 , c_p , c_v , and κ are constants

- β may vary as a function of temperature
- viscosity is neglected
- the acoustic propagation is linear

where c_v is the liquid specific heat capacity at constant volume.

The first approximation is well justified in condensed state matter such as liquids for which $\gamma - 1 = \frac{c_p}{c_v} - 1 \ll 1$. It is thanks to this approximation that the thermal equation 1.9 can be decoupled from the acoustic pressure dictated by eq. 1.10.

Section 1.2.2 and chapter 5 will take into account the temperature-dependence of the thermal expansion coefficient. Everywhere else in the manuscript, $\beta(T)$ will be considered to be constant $\beta(T) = \beta(T_0) = \beta_0$ where T_0 is the equilibrium temperature in the medium.

In the context of photoacoustic imaging, the heat source term in equations 1.9 and 1.10 arises from light absorption by the medium and can thus be written as:

$$P_V(\mathbf{r}, t) = \mu_a(\mathbf{r})\Phi_r(\mathbf{r}, t) \quad (1.11)$$

where $\mu_a(\mathbf{r})$ is the medium optical absorption coefficient at position \mathbf{r} and $\Phi_r(\mathbf{r}, t)$ is the fluence rate (power per unit surface) in the medium at position \mathbf{r} and time t .

The photoacoustic effect is fully described by equations 1.9, 1.10 and 1.11. However, there is in general no analytic solutions to this set of equations and thus additional approximations are often used. Going back to equation 1.10, we can see, as mentioned earlier, that the acoustic source term arises from temporal variations of the temperature. This will for example be the case if the sample is illuminated by a light source which intensity is rapidly modulated. This can be achieved by using pulsed or intensity-modulated laser sources. Although both types of sources can be used for biological tissue imaging, pulsed illumination is often preferred because of the more efficient photoacoustic generation it provides. Moreover, for reasons that will be explained later in this chapter, pulses duration are usually in the nanosecond range for photoacoustic imaging, and only such pulses duration will be considered in this thesis.

Depending on the pulse duration and the medium parameters, three different photoacoustic generation regimes can be distinguished. For two of these regimes additional approximations can be made concerning 1.9, 1.10, and 1.11 that further simplify their resolutions.

Before moving on to the description of the different photoacoustic generation regimes, we give the values of the water parameters relevant to the photoacoustic generation problem. These values are given at 20 °C and will be approximated as being those of biological tissues:

- $c_s \approx 1500 \text{ m s}^{-1}$
- $\rho_0 \approx 1000 \text{ kg m}^{-3}$
- $c_p \approx 4200 \text{ J kg}^{-1} \text{ K}^{-1}$
- $\beta \approx 2 \times 10^{-4} \text{ K}^{-1}$
- $\kappa \approx 0.6 \text{ W K}^{-1} \text{ m}^{-1}$

The heat diffusion coefficient $\chi = \frac{\kappa}{\rho_0 c_p}$ and the dimensionless Grüneisen parameter $\Gamma = \frac{\beta_0 c_s^2}{c_p}$ are also two important parameters in photoacoustics. Their values for water at 20 °C are:

- $\chi \approx 1.4 \times 10^{-7} \text{ m}^2 \text{ s}^{-1}$
- $\Gamma \approx 0.1$

Confinement regimes

Let us consider an absorbing inclusion of characteristic dimension D_a . The speed of sound in the medium is c_s and its heat conductivity is χ . The absorbing inclusion is illuminated by a light pulse of characteristic duration τ_p and emits acoustic waves according to the photoacoustic effect. The generated acoustic waves are often called photoacoustic waves.

By comparing the characteristic duration τ_p of the light pulse to two other important time scales of the problem, three photoacoustic generation regimes can be defined. The first time scale is the time needed for heat to diffuse on a distance that is on the order of the characteristic dimension D_a of the absorbing inclusion :

$$\tau_{th} = \frac{D_a^2}{\chi} \tag{1.12}$$

If $\tau_p \ll \tau_{th}$ the photoacoustic generation regime is called the **heat or thermal confinement regime**. In this regime there is no significant heat diffusion during light absorption.

Therefore the light absorption and the heat diffusion phase can be considered to be uncoupled and during the light absorption phase equation 1.9 can be written by neglecting the diffusion term as:

$$\frac{\partial T}{\partial t}(\mathbf{r}, t) = \frac{P_V(\mathbf{r}, t)}{\rho_0 c_p} \quad (1.13)$$

The acoustic wave equation 1.10 can thus be simplified and directly written as a function of the absorbed power density $P_v(\mathbf{r}, t)$:

$$\Delta p(\mathbf{r}, t) - \frac{1}{c_s^2} \frac{\partial^2 p}{\partial t^2}(\mathbf{r}, t) = -\frac{\Gamma}{c_s^2} \frac{\partial P_V}{\partial t}(\mathbf{r}, t) \quad (1.14)$$

where $\Gamma = \frac{\beta_0 c_s^2}{c_p}$ is the Grüneisen parameter introduced above.

For a typical $\tau_p = 5$ ns pulse, the heat confinement regime is reached if the absorbing inclusion characteristic dimension D_a is much greater than about 27 nm. Therefore, apart from the situations where nanoscale absorbing objects are considered, the assumption of thermal confinement usually holds in photoacoustic imaging of tissue.

The second time scale is the time needed for the generated photoacoustic waves to propagate on a distance of the order of the absorbing inclusion characteristic dimension D_a :

$$\tau_{ac} = \frac{D_a}{c_s} \quad (1.15)$$

The regime where $\tau_p \ll \tau_{ac}$ is called the stress confinement regime. If both $\tau_p \ll \tau_{th}$ and $\tau_p \ll \tau_{ac}$, the photoacoustic generation takes place under both the heat and stress confinement regimes. In this regime there is neither significant heat diffusion nor acoustic propagation during light absorption so that the light pulse characteristic duration is not a parameter of the problem anymore and the absorbed power density can be written as:

$$P_V(\mathbf{r}, t) = E_V(\mathbf{r})\delta(t) = \mu_a(\mathbf{r})\Phi(\mathbf{r})\delta(t) \quad (1.16)$$

where $E_V(\mathbf{r}) = \int P_V(\mathbf{r}, t) dt$ is the absorbed energy density in the medium at position \mathbf{r} and $\Phi(\mathbf{r})$ is the fluence in the medium at position \mathbf{r} . The acoustic wave equation 1.10 can

thus be even further simplified and written:

$$\Delta p(\mathbf{r}, t) - \frac{1}{c_s^2} \frac{\partial^2 p}{\partial t^2}(\mathbf{r}, t) = -\frac{\Gamma}{c_s^2} E_V(\mathbf{r}) \frac{d\delta(t)}{dt} \quad (1.17)$$

It can be shown that the problem described by the above acoustic wave equation 1.17 with a source term can also be described by the following set of acoustic equation without source term but with initial conditions:

$$\Delta p(\mathbf{r}, t) - \frac{1}{c_s^2} \frac{\partial^2 p}{\partial t^2}(\mathbf{r}, t) = 0 \quad \forall \mathbf{r}, t > 0 \quad (1.18a)$$

$$p(\mathbf{r}, t = 0) = p_0(\mathbf{r}) = \Gamma E_V(\mathbf{r}) = \Gamma \mu_a(\mathbf{r}) \Phi(\mathbf{r}) \quad \forall \mathbf{r} \quad (1.18b)$$

$$\frac{\partial p}{\partial t}(\mathbf{r}, t = 0) = 0 \quad \forall \mathbf{r} \quad (1.18c)$$

This set of equations is very often used and cited in photoacoustic imaging works. It shows that, in the heat and stress confinement regime, the generation of photoacoustic waves can be seen as the relaxation of an initial instantaneous pressure rise $p_0(\mathbf{r}) = \Gamma \mu_a(\mathbf{r}) \Phi(\mathbf{r})$. This initial pressure rise is thus equal to the Grüneisen parameter times the density of absorbed energy.

For a typical $\tau_p = 5$ ns pulse, the heat and stress confinement regime is reached if the absorbing inclusion characteristic dimension D_a is much greater than about 7.5 μm .

In fluids and biological tissues assimilated as water τ_{ac} is much smaller than τ_{th} provided that D_a is much bigger than about 0.1 nm. As this is always the case in photoacoustic imaging, the stress confinement regime implies the heat confinement regime. Therefore, the heat and stress confinement regime will equivalently be referred to as the stress confinement regime further in this chapter.

The resolution of equations 1.9, 1.10 and 1.11 may be carried out using the Green's function approach, however even in the most simplified context of the heat and stress confinement regime no analytic solutions necessarily exist because of the potentially complex distribution of $\mu_a(\mathbf{r}) \Phi(\mathbf{r})$.

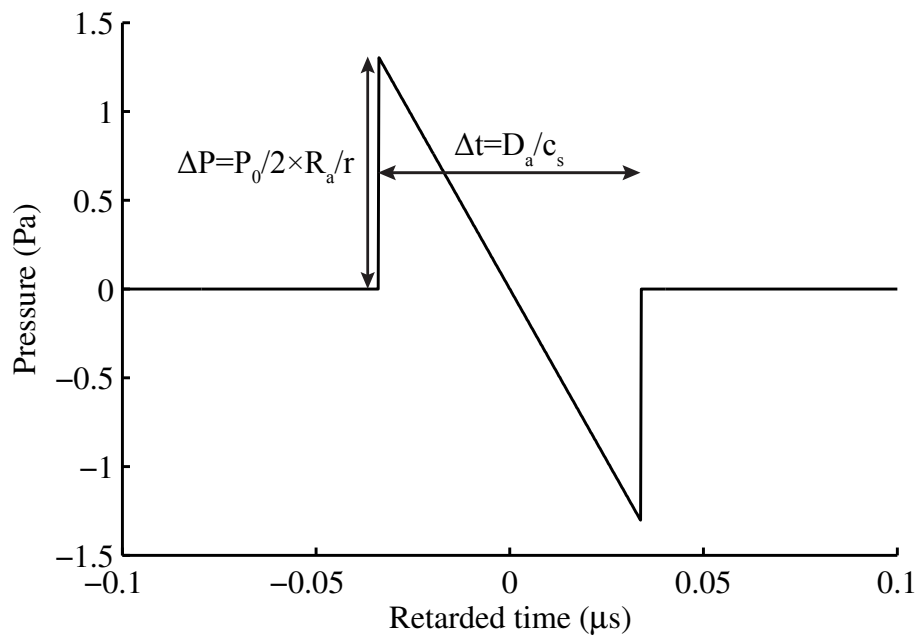


Figure 1.2 – Photoacoustic pressure wave generated by a homogeneously absorbing sphere, with the following parameters: $\mu_a = 1 \text{ cm}^{-1}$, $D_a = 100 \text{ }\mu\text{m}$ sphere, illuminated by a $\Phi = 5 \text{ mJ cm}^{-2}$ light pulse, detected at a distance $r = 10 \text{ mm}$, as a function of the retarded time $t_r = t - \frac{r}{c_s}$. The considered medium is water ($c_s = 1500 \text{ m s}^{-1}$).

The homogeneously absorbing sphere

One particular problem can quite easily be solved analytically and is often referred to as a simple and useful model in photoacoustic imaging publications. This problem is that of a homogeneously absorbing spherical inclusion of optical absorption coefficient μ_a and diameter D_a illuminated by a light pulse of characteristic duration τ_p in the heat and stress confinement regime. The sphere optical absorption is assumed to be small compared to $\frac{1}{D_a}$ so that the illumination Φ and the volumetric absorbed energy $E_v = \mu_a \Phi$ can be considered homogeneous inside the sphere. For simplicity reasons the sphere surrounding medium is assumed to be non absorbing. In the situation described above it can quite easily be shown that the generated photoacoustic pressure wave *outside* the sphere can be written as:

$$p(r, t) = \frac{p_0}{2r} \times (r - c_s t) \quad (1.19)$$

for

$$r - c_s t \in \left[-\frac{D_a}{2}, \frac{D_a}{2} \right]$$

$$p_0 = \mu_a \Phi$$

and zero otherwise. This function describes a typical "N" shape pressure wave that is represented on figure 1.2 for $\mu_a = 1 \text{ cm}^{-1}$, $D_a = 100 \text{ }\mu\text{m}$ sphere, $\Phi = 5 \text{ mJ cm}^{-2}$ illumination, and $r = 10 \text{ mm}$ detection distance.

The corresponding spectrum is given by:

$$\tilde{p}(r, \hat{q}) = \frac{i p_0 D_a^2}{4 r c_s} e^{-i \hat{q} \frac{2r}{D_a}} \left[\frac{\sin(\hat{q})}{\hat{q}^2} - \frac{\cos(\hat{q})}{\hat{q}} \right] \quad (1.20)$$

where $\hat{q} = \frac{\pi \nu D_a}{c_s}$.

The spectrum maxima positions are given by the solutions \hat{q} of the following equation:

$$\tan(\hat{q}) = \frac{-2\hat{q}}{\hat{q}^2 - 2} \quad (1.21)$$

The normalized amplitude of the function $\tilde{p}(r, \hat{q})$ is represented on figure 1.3 as a function

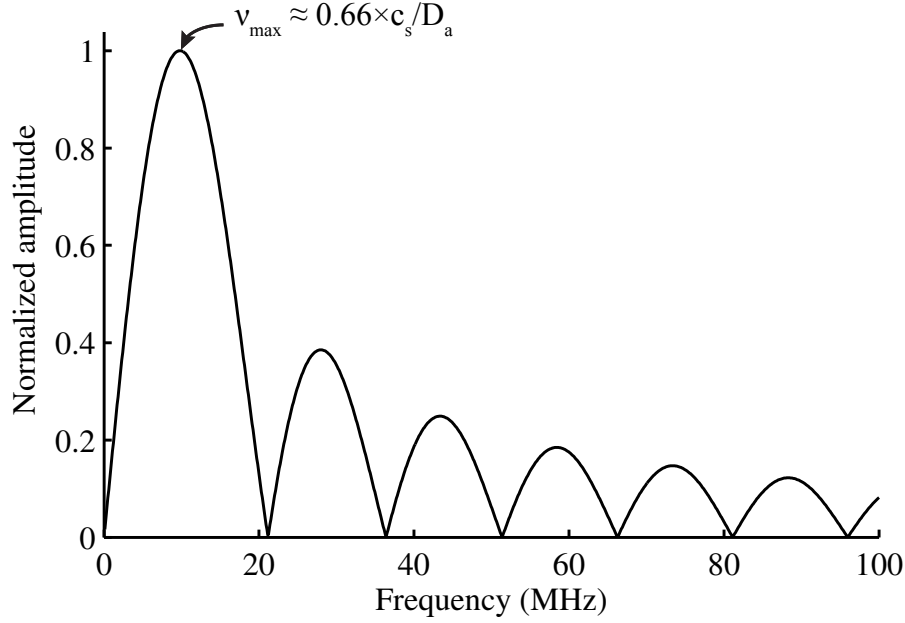


Figure 1.3 – Spectrum normalized amplitude of the photoacoustic signal generated by a $D_a = 100 \mu\text{m}$ sphere considering a speed of sound $c_s = 1500 \text{ m s}^{-1}$.

of the frequency ν in the case of a sphere of diameter $D_a = 100 \mu\text{m}$ and a speed of sound $c_s = 1500 \text{ m s}^{-2}$.

As can be seen on figures 1.2 and 1.3 and equations 1.19 and 1.20 the duration $\Delta t = \frac{D_a}{c_s}$ and the dominant frequency $\nu_{\max} \approx 0.66 \frac{c_s}{D_a}$ are dictated by the sphere characteristic dimension D_a and the speed of sound inside the sphere c_s .

The amplitude $\Delta P(r)$ of the generated photoacoustic wave is given by the following equation:

$$\Delta P(r) = \frac{p_0}{2} \frac{R_a}{r} = \frac{\Gamma E_v}{2} \frac{R_a}{r} = \frac{\Gamma \mu_a \Phi}{2} \frac{R_a}{r} \quad (1.22)$$

where $R_a = \frac{D_a}{2}$.

It is interesting to do a simple computation to have an order of magnitude of the initial temperature and pressure rises respectively ΔT_0 and p_0 . For $\Gamma = 0.1$, $\mu_a = 1 \text{ cm}^{-1}$, $\Phi = 1 \text{ mJ cm}^{-2}$, $\rho_0 = 1000 \text{ kg m}^{-3}$ and $c_p = 4200 \text{ J kg}^{-1} \text{ K}^{-1}$, one obtains $\Delta T_0 = 0.25 \text{ mK}$, $p_0 = 100 \text{ Pa}$. This means that for every mJ cm^{-3} of absorbed optical energy, there will be initial temperature and pressure rises of respectively 0.25 mK and 100 Pa .

When the stress confinement regime is not valid anymore, the finite duration τ_p of the light pulse has to be taken into account. In the heat confinement regime, this can straightforwardly be achieved by a convolution of the pressure field generated in the stress confinement regime with a function describing the temporal profile of the light pulse. Let $\frac{1}{\tau_p}f(\frac{t}{\tau_p})$ be such a function, defined here by the following equation $\int_{-\infty}^{\infty} \frac{1}{\tau_p}f(\frac{t}{\tau_p}) dt = 1$.

In the case of a Gaussian temporal profile light pulse, the function $f(\frac{t}{\tau_p})$ would be written as:

$$f\left(\frac{t}{\tau_p}\right) = \frac{2\sqrt{\ln(2)}}{\sqrt{\pi}} e^{-4\ln(2)t^2/\tau_p^2} \quad (1.23)$$

where τ_p is the full width at half maximum.

The effect of the convolution with such a light pulse will be to decrease the amplitude, increase the duration, and low-pass filter the spectrum of the generated photoacoustic waves compared to that obtained in the stress confinement regime. If $\tau_p \ll \tau_{ac}$ then the light pulse is similar to a Dirac distribution and the resulting pressure wave tends towards that of the heat and stress confinement regime. If $\tau_{ac} \ll \tau_p$ then the "N" shape waveform acts in the convolution as the derivative of a Dirac pulse and the resulting pressure wave is proportional to the derivative of the temporal profile of the light pulse $p(r, t) \sim f(\hat{\tau}) * \frac{d}{dt}\delta(t) = \frac{d}{d\hat{\tau}}f(\hat{\tau})$, where $\hat{\tau} = \frac{t-r}{c_s}$.

It should be noticed that the approach described here, based on the temporal convolution of the wave function obtained within the heat and stress confinement regime pressure with the function describing the temporal profile of the light pulse, is only possible if (as was implicitly assumed in the previous description) the volumetric absorbed optical power $P_v(r, t)$ is a separable function that can be written $P_v(r, t) = E_v(r)\frac{1}{\tau_p}f(\frac{t}{\tau_p})$. If that is not the case, then the photoacoustic generation and propagation problem in the heat confinement regime has to be directly solved by use of the Green function approach for example, but cannot benefit from the solution of the problem in the stress (and therefore heat) confinement regime.

In the situation where $\tau_p \geq \tau_{th}$, the resolution of the photoacoustic generation problem is much more complex and requires first solving the heat diffusion equation 1.9, before the temperature field can then be used as a source term for the acoustic wave equation 1.10. This regime is encountered with nanoseconds pulses when the absorbers dimensions are

about or smaller than a few tens of nanometers as previously mentioned. Such a situation will be encountered and described in more details in chapter 5 of this thesis dealing with the photoacoustic generation by gold nanoparticles.

The resolution of the photoacoustic problem has been briefly described in the few previous pages in the very simple context of a uniform volumetric absorbed optical power $P_v(t) = \mu_a \Phi(t)$ limited to a spherical volume. In a more realistic photoacoustic problem with a complex volumetric absorbed optical power distribution $P_v(\mathbf{r}, t) = \mu_a(\mathbf{r})\Phi(\mathbf{r}, t)$ the same principles remain valid, however the resolution of the photoacoustic problem is of course much more complicated in general as previously mentioned. In such a situation, as with any wave generation problem, the time and space distribution of the volumetric absorbed optical power will also impact the distribution of the generated photoacoustic waves in the different space directions.

It is worth noticing that it has been considered until now, and further in this thesis as well, that the absorbed optical energy was entirely converted into heat. Although this is only an approximation, it is a good one both in biological tissues [Li and Wang, 2009] and for gold nanoparticles [Govorov and Richardson, 2007].

1.1.3 Photoacoustics applied to imaging

Although the photoacoustic effect was discovered more than a century ago by Alexander Graham Bell, it was not until quite recently that it was exploited for biological tissues imaging. The first industrial and scientific applications began to emerge short after the development of the laser, in the 1970s and the 1980s, but were limited to gas, liquid and solid characterization and non-destructive testing of solids. Its exploitation for biological tissues imaging was not investigated until the mid-1990s, when the first images began to appear. The first high quality *in vivo* images appeared in the early to mid-2000s, when photoacoustic imaging became a very active and fast-growing field of research in biomedical imaging.

It is interesting to understand how the photoacoustic effect can be used for biological tissues imaging and why it is a promising biomedical imaging modality. Indeed it took such a long time before being exploited for biomedical imaging and then quickly became a fast-growing field of research.

As explained in section 1.1.1 light propagation in biological tissues is dominated by optical scattering. This induces a strong degradation of the resolution with the penetration depth. Indeed the photons trajectories quickly become quite complex and therefore the spatial encoding in the information they convey about the different illuminated regions of the imaged biological tissue becomes difficult to read.

This is not the case for acoustic waves with frequencies in the MHz range as the acoustic scattering coefficient at these frequencies is two to three orders of magnitude lower in biological tissues than the optical scattering coefficient [Wang and Wu, 2007]. In practice, ultrasound waves propagate ballistically up to several centimeters in depth. Thus it can be interesting to combine optical and acoustic waves to benefit both from the optical image contrast provided by the interaction of optical waves with biological tissues and the resolution and penetration depth provided by acoustic waves. Such a strategy is often used in photoacoustic imaging where biological tissues are illuminated and the photoacoustic waves generated by the biological tissues illumination are detected are their surfaces.

Within the heat and stress confinement regime, ideal (i.e, free from reconstruction artifacts) photoacoustic images represent the initial pressure rise distribution inside biological tissues due to the photoacoustic effect, $p_0(\mathbf{r}) = \Gamma\mu_a(\mathbf{r})\Phi(\mathbf{r})$. The Grüneisen parameter is often considered to be a constant. In this case the photoacoustic images represent the absorbed optical energy. They are however not the representation of the optical absorption coefficient because the light distribution inside the biological tissue $\Phi(\mathbf{r})$ is a complex function that depends in particular on the optical absorption and scattering properties of the illuminated regions within biological tissue. Thanks to the fact that the optical absorption properties of tissues are very dependent on both the tissue type and the optical wavelength, as can be seen on figure 1.1, photoacoustic images benefit from high images contrasts and can provide useful physiological and functional information on biological tissue. The temperature dependence of the Grüneisen parameter is sometimes taken into account for photoacoustic temperature measurements. Blood flow velocities can also be measured by techniques similar to the ones used in Doppler ultrasound.

Photoacoustic imaging depth is ultimately limited by the ability to irradiate the tissue at depth with a sufficient amount of light and to detect the generated photoacoustic waves. Thus it is limited by both optical and acoustic attenuation. Optical attenuation in biological tissues was briefly described in section 1.1.1 and can be characterized at depths greater than several optical transport mean free paths by the optical effective extinction coefficient

$\mu_{eff} \approx 1.7 \text{ cm}^{-1}$ or equivalently by the optical penetration depth $l_{eff} = \frac{1}{\mu_{eff}} \approx 5.8 \text{ mm}$. Acoustic attenuation is very dependent on the biological tissue type and state but can be considered to be of the order of $\mu_{att} \approx 1 \text{ dB cm}^{-1} \text{ MHz}^{-1} \approx 0.12 \text{ Np cm}^{-1} \text{ MHz}^{-1}$ [Szabo, 2004] or equivalently the acoustic attenuation length to be about $l_{eff} = \frac{1}{\mu_{eff}} \approx 8.7 \text{ cm MHz}$. Thus optical attenuation dominates at low frequencies in the several MHz range but not at higher frequencies in the several tens of MHz range where optical and acoustic attenuations are of the same order of magnitude or at even higher frequencies in the several hundreds of MHz range where acoustic attenuation dominates. In practice, a penetration depth of about 4 cm has been achieved *in vivo* in a human breast [Kruger et al., 2010]. At such depth however resolution is limited to several hundreds micrometers for reasons that will be explained in the following paragraph.

Photoacoustic imaging techniques can be divided in two categories based on the origin of their images spatial resolution. In the first category, light propagates diffusively and the image resolution is ultimately dictated by the frequency content of the detected photoacoustic waves. This category is called acoustic-resolution photoacoustic imaging. The nanoseconds light pulses generally used in photoacoustic imaging enable the generation of high frequencies broadband pressure waves and thus the factor limiting the bandwidth of the detected photoacoustic waves is in practice the low pass filtering due to the frequency dependent acoustic attenuation of biological tissues. The spatial resolution therefore degrades with the imaging depth. In practice, the limited detection apertures, detectors sizes, sensitivities and bandwidths, and the safety maximum illumination powers restrictions can further limit the spatial resolution. The typical depth-to-resolution ratio achieved in biological tissues is on the order of 100 in the acoustic-resolution regime, for depth ranging from a few centimeters to a few hundreds micron.

In the second category, tight optical focusing is achieved inside the tissue into one or multiple diffraction limited spots and the spatial resolution is mostly dictated by the focused spots dimension. This second category is called optical-resolution photoacoustic imaging or equivalently optical-resolution photoacoustic microscopy (OR-PAM). A microscope objective is generally used to focus and scan the illumination beam and the image of the biological tissue is acquired by the detection of the photoacoustic wave generated at each scanning position. The lateral resolution is thus defined by the dimension of the focused optical beam and the axial resolution by the bandwidths of the detected photoacoustic waves and the detection device. Penetration depths in biological tissues are limited by op-

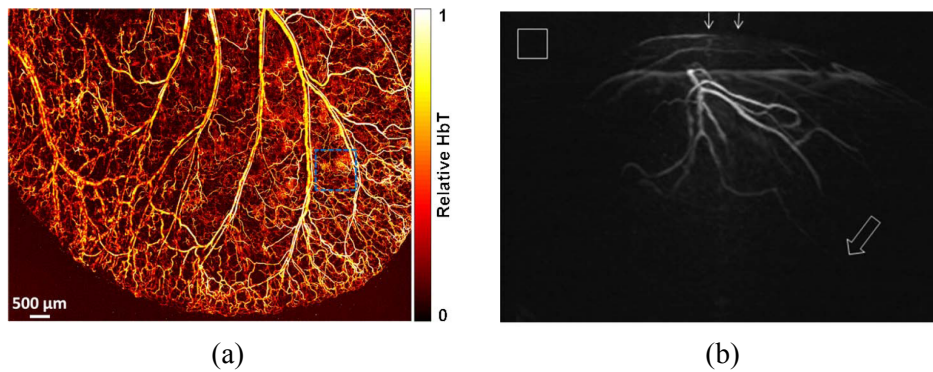


Figure 1.4 – (a) Optical-resolution photoacoustic image of relative hemoglobin concentration (HbT) in a living mouse ear, taken from [Hu et al., 2011]. (b) Acoustic-resolution photoacoustic image of a human breast. Arrows at top indicate the direction of the incident excitation light. Hollow arrow marks the position of a vessel at a depth of 40 mm. The hollow box represents $1 \times 1 \text{ cm}^2$. The excitation wavelength is 800 nm. Taken from [Kruger et al., 2010].

tical scattering to about a few scattering mean free path ($l_s \approx 100 \mu\text{m}$). At such depths, lateral resolutions on the micrometer scale can be achieved. It should however be noted that these high lateral resolutions occur at the depth of the optical focus and degrade rapidly elsewhere. Micrometer scale lateral resolution could also be achieved by acoustic-resolution photoacoustic imaging but would require the detection of several hundreds of MHz photoacoustic waves and thus would be limited by acoustic attenuation to penetration depth on the order of $100 \mu\text{m}$ [Maslov et al., 2008].

Figure 1.4 illustrates optical and acoustic resolution photoacoustic images taken from the literature.

1.1.4 Imaging setups

There are a lot of different commonly used setup types in photoacoustic imaging. Their detailed description as well as the one of all their potential applications is out of the scope of this thesis, and can be found in photoacoustic imaging reviews such as [Beard, 2011] and [Wang and Hu, 2012]. Only a very general description of the underlying principles of the practical implementations of photoacoustic imaging experiments is given here. There are at least three fundamental elements in every photoacoustic imaging experiment: a sample of interest, a light source and an acoustic wave detector. Each of these three elements may

be characterized by a set a of parameters that may vary from one photoacoustic imaging experiment to another. These parameters are described in the following paragraphs.

The sample may be characterized by its type, state, size, shape, the use of contrast agents, the invasiveness of the imaging process and the modification of its state during the imaging process. The different sample types might be tissue phantoms, biological tissues from different animals, biological tissues from different body parts, etc. The different sample states might for example be *in vivo*, *ex vivo*, *in vitro*, its temperature, etc. The samples sizes and shapes might be very different for example for a mouse, a human forearm, and a human breast. The use of contrast agents can provide enhanced signal from biological tissues, with disease specific photoacoustic contrast for example. Commonly used contrast agents includes organic dye such as ICG [Kim et al., 2010b], Evans blue [Song et al., 2009], and methylene blue [Song et al., 2008] that are composed of large organic molecules on the nanometer scale, and gold nanoparticles which dimensions range from a few tens of nanometers to a few hundreds of nanometers. The use of endoscopic imaging can significantly improve the achievable imaging depth, at the cost of invasiveness. The sample state might be modified during the imaging process, for example during photoacoustic temperature monitoring experiments [Larina et al., 2005; Shah et al., 2008; Pramanik and Wang, 2009].

The light source may be characterized by its wavelength, intensity, modulation type, pulse duration and pulse repetition rate in the case of pulsed sources, the light distribution and incidence angle on the sample, the way the light is brought in contact with the sample, and possible light scanning during the imaging process. The light wavelength may for example be tuned for optimal penetration depth inside a sample or optimal photoacoustic generation by a given absorber. The light intensity will impact the amplitude of the generated photoacoustic waves and thus the acoustic waves detection signal-to-noise ratio. The optical fluence or fluence rates that can be used to illuminate biological tissues without any damages are limited. Specific rules applies to computes such maximum permissible exposure (MPE). On skin for wavelengths in the visible range, such rules often reduces to limiting the fluence of one of the illumination pulse to no more than 20 mJ cm^{-2} . Because the generated photoacoustic waves are orders of magnitude lower than those used for example in ultrasound imaging, usually lower than 10 kPa against sometimes more than 1 MPa in ultrasound imaging, potential damages due to ultrasound exposure are not of concern in photoacoustic imaging. Photoacoustic generation requires the modulation of the optical

absorbed energy (see Eqs. 1.9 and 1.10). This can be achieved by use of amplitude modulated continuous-wave lasers or pulsed lasers. The latter solution is often preferred for the broadband photoacoustic waves and higher photoacoustic waves signal-to-noise ratio detection provided at the MPE illumination. In photoacoustic imaging, the light pulse duration is chosen sufficiently short for the generation of high frequencies photoacoustic waves and for an efficient photoacoustic generation, and sufficiently long for the safety standard to allow the delivery of significant optical energies on the absorbers. All in all, the chosen laser pulses durations are generally of the order of nanoseconds. The light spreading and incidence angle on the sample is quite important as it can for example be tuned to provide optimal light delivery in a specific region of the sample, minimize the photoacoustic waves generated at the sample surface by dark-field illumination, or provide optical-resolution photoacoustic imaging with diffraction-limited focused spot inside the sample (micrometer scale). The light may be brought in contact with the sample for example through free space propagation, thanks to optical lenses and mirrors orientation or optical waveguide such as optical fibers and fiber bundles. Light scanning relative to the sample might be used for example to ensure identical illumination of the different imaged regions and to reduce the necessary total light power, or to provide optical-resolution photoacoustic images.

The acoustic waves detector may be characterized by its frequency response, sensitivity, position compared to the sample, distribution in space, the number of detectors used, the physical principle on which it relies for acoustic waves detection, the way it interacts with the sample, the fact that it is scanned during the imaging process, its directivity, and the data processing algorithm used. The acoustic detector frequency response plays a significant role in dictating the achieved resolution of the system. It is usually adapted to the frequency content of photoacoustic waves to be detected, thus for example to the absorbers sizes and the imaging depth in the case of samples such as biological tissues that have frequency dependent acoustic attenuation. The sensitivity of the detector is of course a crucial point for the detection of low amplitude photoacoustic waves with a good signal-to-noise ratio. The different acoustic detector positions relatively to the sample might for example be away from the sample, in contact to the sample surface, or even inside the sample in the case of photoacoustic endoscopy. The distribution in space of the acoustic waves detector determines the aperture of the detection and might for example be described by portion of a plane, of a cylinder, or of a sphere. The chosen geometry is often dictated by the size and shape of the sample. The use of several detector is often a mean to parallelize the

detection and thus increase the imaging speed. This can for example be achieved by the use of linear or two-dimensional array probes resembling those used in conventional ultrasound imaging, or arc or hemispherical array detectors. The physical principles that are used for the detection of the acoustic waves may for example range from the piezoelectric effect to the optical detection via the thickness modulation of a Fabry-Perot etalon [Beard et al., 1999; Zhang et al., 2008]. The interaction between the detector and the sample might be contact-less, require direct contact with the sample, or the presence of a coupling medium such as water or an ultrasound gel. The detector might be fixed or scanned compared to the sample. The reasons for scanning the detector depend on the setup parameters but may include the fact that it is necessary for the imaging process itself, that it can provide increased detection aperture, imaging field of view, or detection sensitivity homogeneity. The directivity of the acoustic detector is an important parameter as well but its role largely depends on the type of setup used. It can for example be required that the detectors have a very low directivity in some setups based on a large number of detectors idealized as being point-like, or that the detector has a strong directivity to provide image resolution by scanning of the detector or enhanced sensitivity. Once the photoacoustic waves have been detected, the acquired data can be processed, for example to reconstruct the initial pressure rise distribution inside the sample by different types of algorithms, depending on the available information about the elements of the experiment, the required imaging performance and the available computing power.

Figure 1.6 provides a few examples from the literature of photoacoustic images illustrating a wide a variety of the possible approaches and samples mentioned previously.

1.2 Structure and objectives of the thesis

1.2.1 New approaches in optical-resolution photoacoustic micro-endoscopy

Part I of this thesis deals with optical-resolution photoacoustic imaging and more specifically new approaches for micro-endoscopy.

As introduced in section 1.1.3, there are two factors that limit the penetration depth of photoacoustic imaging in biological tissues: optical and acoustic attenuation. The penetra-

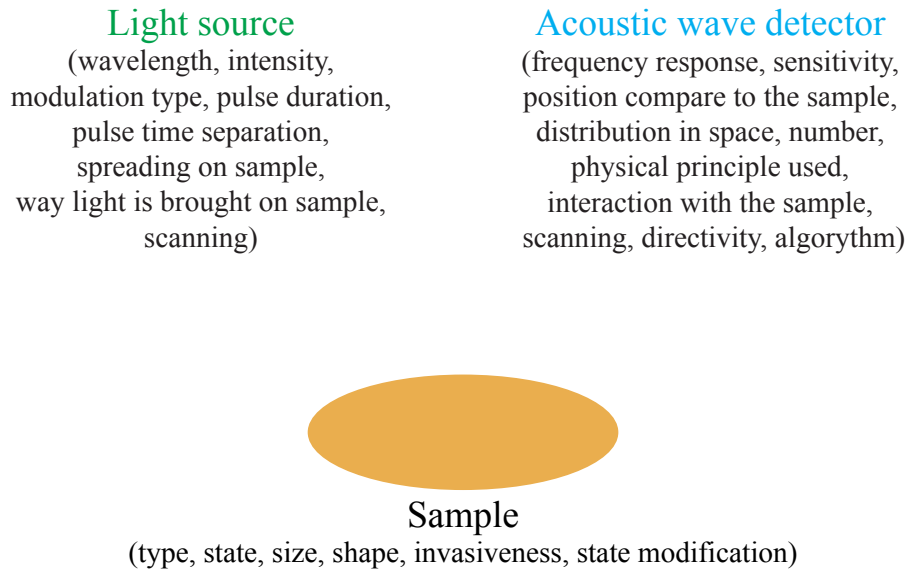


Figure 1.5 – Fundamental elements and parameters of a photoacoustic imaging setup.

tion depth of optical-resolution photoacoustic imaging is usually only limited by optical scattering to no more than a few scattering mean free path ($l_s \approx 100 \mu\text{m}$), less than one transport mean free path ($l_{tr} \approx 1 \text{ mm}$) as it relies on the ability to focus light inside the tissue. It is therefore a photoacoustic modality limited to superficial imaging of biological tissues, quite alike optical microscopy, although it provides a unique absorption-based image contrast that no other microscopy techniques are currently able to provide. To overcome this quite restrictive imaging depth limitation of optical-resolution photoacoustic imaging, one would need to be able to focus and scan an optical spot at large optical depths. To do so two different approaches are possible: wavefront shaping, and endoscopy. The first one tries to compensate for optical scattering to focus light inside or behind a scattering media [Chaigne et al., 2014]. Although promising research is being done in this field, light focusing inside a biological tissue has not yet been achieved and would probably be limited to depths of a few millimeters. The second approach is more intuitive and simply relies on the ability to directly and invasively guide light inside tissue. Optical endoscopy can be achieved by four main approaches. The first one relies on the use of fiber bundles composed of single-mode or almost single-mode fibers, each of them carrying some part of the final image and representing one of its pixels [Göbel et al., 2004]. Although these types

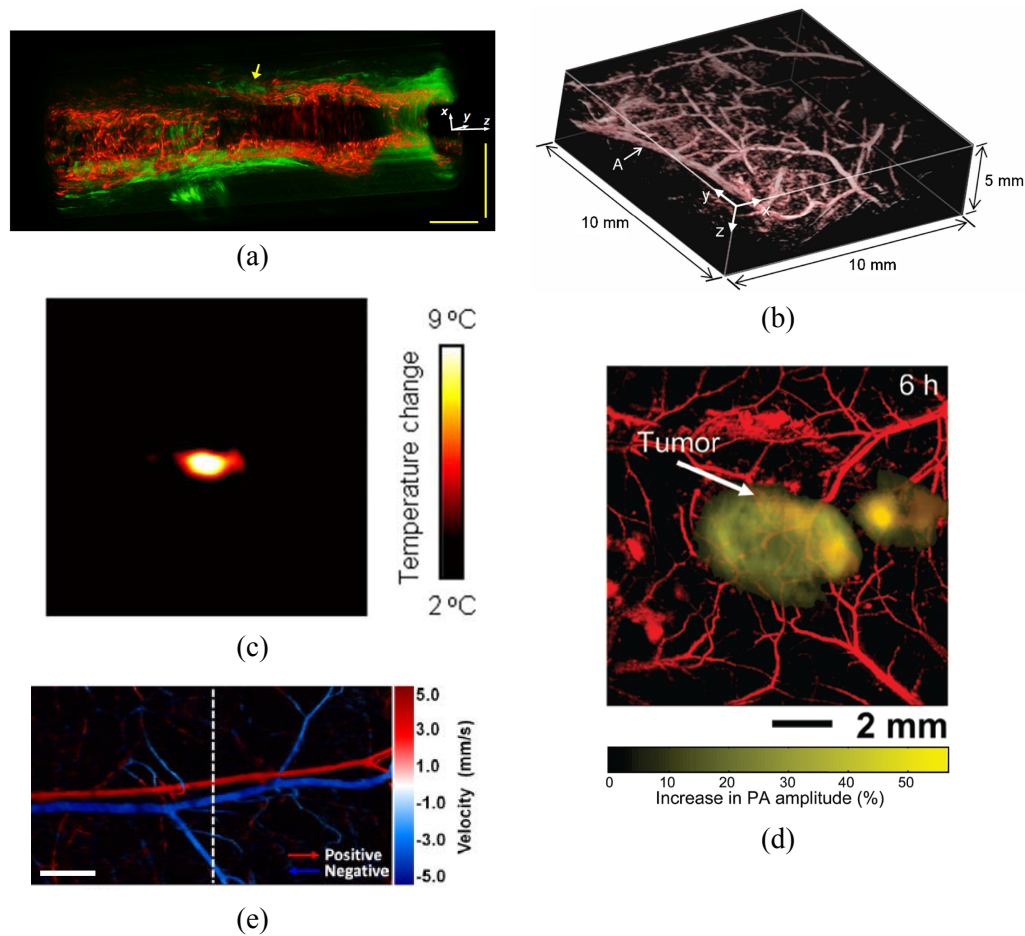


Figure 1.6 – (a) Dual mode photoacoustic (in red) and ultrasound (in green) endoscopy images acquired *in vivo* in a rat colon. The arrow indicates a $x - y$ slice not represented here. The horizontal and vertical scale bars represent 5 mm. Taken from [Yang et al., 2012]. (b) Photoacoustic image of the vasculature in the skin around the abdomen of a mouse acquired *ex vivo*. The generated photoacoustic waves were detected optically by a system based on a Fabry-Perot etalon. Taken from [Zhang et al., 2009]. (c) Photoacoustic image for the monitoring of a photothermal therapy conducted *ex-vivo* in a porcine muscle with injected gold nanoparticles. The image was acquired 240 s after the beginning of the therapy. The color bar indicates the temperature change since the beginning of the therapy based on a prior calibration. The image cover a 20×20 mm field of view. Taken from [Shah et al., 2008]. (d) Photoacoustic image of a melanoma on the back of a living mouse acquired 6 h after intravenous injection through the tail vein of targeted gold nanocages. The background vasculature image was obtained using a 570 nm excitation wavelength and a 50 MHz frequency transducer. The melanoma image was obtained using a 778 nm excitation wavelength and a 10 MHz transducer. Color schemes: red for blood vessels and yellow for the increase in photoacoustic amplitude in the melanoma image compared to the melanoma image acquire before the gold nanocages injection. Taken from [Kim et al., 2010a]. (e) Optical-resolution Doppler flowmetry photoacoustic image of a mouse ear. The dashed line indicates a velocity profile not represented here. The scale bar represents $250 \mu\text{m}$. Taken from [Yao et al., 2010].

of endoscopes are flexible and quite easy to use once fabricated, their image resolution is limited by the distance between two fibers that must be large enough to prevent coupling between the fibers that would degrade the image, and their diameter usually range from 1 to a few millimeters as high quality images requires the use of a significant amount of fibers inside the bundle thus increasing its diameter. The second approach is to use miniature optical components such as gradient index lenses. The main drawbacks of these devices are that they are rigid and that their lengths are limited by the strong optical aberrations introduced in long device by the miniaturized optical elements. Thus their imaging depth is in practice limited to a few millimeters for high quality images [Jung and Schnitzer, 2003; Levene et al., 2004]. The third approach is based on the combination of optical elements such as mirrors, gradient index lenses, and single-mode optical fibers and miniature mechanical elements integrated inside the endoscope to scan the optical focused beams. These designs can provide flexible endoscopes with high images quality but diameters still limited to more than about 2 mm [Myaing et al., 2006; Rivera et al., 2011]. The fourth approach is based on the use of multimode optical fibers. These fibers can benefit from small diameters in the hundred of micrometers range, high numerical apertures, and a large number of supported modes, thus transmitting dense optical information within reduced diameters. However, because of the large number of supported modes, the light propagation inside the fiber resembles that in a scattering media and the transmitted information is scrambled along its propagation. It has been shown recently [Papadopoulos et al., 2012] that digital phase conjugation could be used to control the input beam wavefront in order to scan a focused spot at the output of a multimode fiber despite the complex optical propagation in such fibers. In chapter 2, in collaboration with Dr. Ioannis Papadopolous, Dr. Salma Farahi, Prof. Demetri Psaltis, and Prof. Christophe Moser from École Polytechnique Fédérale de Lausanne in Switzerland, the feasibility of using these techniques for the generation of optical-resolution photoacoustic images at the distal tip of a multimode optical fiber is investigated.

Provided that an optical focused spot can be scanned at depth inside a biological tissue, for example thanks to the use of digital phase conjugation through a multimode fiber, the acoustic attenuation in biological tissues might prevent detecting the high frequency photoacoustic waves generated by the small optical focused spot by detectors located outside the tissue. One of the possible approaches to address this issue is to directly detect the generated photoacoustic waves inside the biological tissues. One solution to do this consists

in the miniaturization of the acoustic detectors, thus reducing their sensitivities, especially for piezoelectric transducers, and demanding dedicated technological developments [Sheaff and Ashkenazi; Zhang and Beard, 2011]. In chapter 3 we introduce and study the use of a fluid-filled capillary to guide high frequency photoacoustic waves through biological tissues for the remote detection of optical-resolution photoacoustic images, thus avoiding the acoustic attenuation in biological tissues and the reduced sensitivity of the miniaturized acoustic detectors.

Photoacoustic endoscopes have been developed and used *in vivo*, for example in rats, but with acoustic lateral resolution limited to about 58 μm and diameters greater than about 2 mm. Optical-resolution photoacoustic endoscope solutions have been proposed however none of the developed systems are currently able to achieve both optical focusing and scanning of an optical beam and detection of the generated photoacoustic waves in biological tissues at depths greater than a few millimeters. The most advanced devices rely on a photoacoustic detection outside the imaged sample and are thus limited to non acoustically absorbing phantoms or very thin biological tissues such as mice ears [Hajireza et al., 2013]. Photoacoustic wave guidance has already been proposed, by use of optical fibers, but not in a photoacoustic endoscopic imaging context, at low photoacoustic waves frequencies in the MHz range [Yapici et al., 2012]. The objective was to achieve multichannel photoacoustic imaging with a single transducer and single-channel data acquisition electronics by temporally separating the contribution of each channel thanks to optical fibers parallel delay lines. Acoustic wave guidance have also been considered for medical ultrasonics but at low acoustic waves frequencies in the few MHz range and inside a solid core or solid shell, thus having to deal with a transmission that is limited by the acoustic impedance mismatches at the waveguide extremities (amplitude transmission of about 12 %, for example, for a water-stainless steel-water boundary at 20 °C) [Nicholson et al., 1989; Nicholson and McDicken, 1991].

The approaches proposed in part I of the thesis are expected to pave the way for the development of minimally invasive optical-resolution photoacoustic endoscopes that could provide micrometer scale resolution absorption based images at centimeters depths inside biological tissues.

1.2.2 Acoustic-resolution sensing and photoacoustic thermal nonlinearity

Part II of this thesis deals with acoustic-resolution photoacoustic imaging, and in particular with the experimental investigation of theoretical predictions on photoacoustic thermal nonlinearity.

As introduced in section 1.1.4, there is a wide variety of photoacoustic imaging setups that can be used. In chapter 4, the development of two acoustic-resolution photoacoustic imaging setups, based respectively on the use of a single high frequency piezoelectric focused transducer and a commercially available ultrasound scanner, is described. The first one is used to image phantoms, while the second one is used for the *in vivo* preliminary studies of tumors distributions of gold nanoparticles injected in mice. The first setup is then used in chapter 5 to study the nonlinear photoacoustic generation by gold nanospheres.

It is often considered that there is a linear relationship between the amplitude of the photoacoustic waves generated by a given absorber and the incident fluence on the absorber. However, when the considered absorber contains for instance gold nanoparticles, such a relationship may not be verified at high incident fluences, and nonlinear photoacoustic generation might be observed due to various effects such as the formation of nano or microbubbles [Zharov, 2011], the saturation of the absorbed optical energy [Zharov, 2011], the aggregation of nanoparticles by endocytosis [Nam et al., 2012], or the temperature dependence of the different mechanical and thermodynamic parameters [Calasso et al., 2001; Egerev and Oraevsky, 2008]. In chapter 5 we are interested in the nonlinear photoacoustic generation due to the temperature-dependence of the thermal expansion coefficient, to which we will refer to as thermal nonlinearity, and that may arise when gold nanoparticles are illuminated by nanoseconds pulses at quite low fluences, typically on the order of or below the MPE on skin. Thermal nonlinearity has been studied theoretically by [Calasso et al., 2001] in a point-like absorber model, by [Inkov et al., 2001] in a model taking into account the finite size of the absorber but with very specific assumptions that do not hold for gold nanospheres, and more recently in our group by Dr. Amaury Prost during his PhD work [Prost, 2014]. This nonlinearity is due to the significant temperature rise that may take place in the vicinity of gold nanospheres illuminated by nanoseconds light pulses [Egerev and Oraevsky, 2008], because of both the strong optical absorption cross-sections of gold nanospheres [Jain et al., 2006] and the fact that almost all the optical

energy absorbed by the gold nanospheres is converted into heat [Govorov and Richardson, 2007]. Therefore, the values of the temperature dependent mechanical and thermodynamic parameters are significantly affected by the important temperature rises in and around the gold nanospheres during the photoacoustic generation. Thermal nonlinearity was observed experimentally in a photoacoustic experiment which objective was to detect 200 nm diameter gold nanospheres in a highly diluted aqueous solution [Egerv and Oraevsky, 2008]. Gold nanoparticles are often used as contrast agents in photoacoustic imaging, for example for tumor targeting. Yet, the use of multispectral photoacoustic imaging is often required to improve the specificity of their detection, which can be challenging because of the complex relationship between the detected photoacoustic signal amplitude and the optical absorption coefficient as explained in section 1.1.3. In chapter 5, we propose to use the thermal nonlinearity to discriminate between two solutions of gold nanospheres and molecular absorbers that may have the same macroscopic optical properties. This could for example lead to new ways to discriminate gold nanoparticles in biological tissues. One of the setup described in chapter 4 was used for the experiments of chapter 5 as it was well adapted to the detection of high frequencies photoacoustic waves for which it was predicted by [Prost, 2014] that the thermal nonlinearity effects would be the most significant.

Part I

Optical-resolution photoacoustic endoscopy

Chapter 2

Photoacoustic excitation through a multimode fiber

Contents

2.1	Background and principles	31
2.1.1	Digital holography	31
2.1.2	Phase conjugation by use of an SLM	34
2.1.3	Focusing and scanning through a multimode fiber	38
2.1.4	Optical-resolution photoacoustic microscopy	42
2.2	Materials and methods	44
2.2.1	Experimental setup	44
2.2.2	Procedure	46
2.3	Results	47
2.3.1	Photoacoustic images	47
2.3.2	Estimation of the resolution	48
2.4	Conclusion	49

As introduced in the previous chapter, although optical-resolution photoacoustic microscopy can provide micrometer resolution images, its penetration depth is limited by optical scattering in biological tissues to less than 1 mm. One solution to overcome this issue is to use an endoscopic approach to scan an optical focused spot directly inside the sample to image. The objective of this chapter is to demonstrate the ability to use digital phase conjugation to generate optical-resolution photoacoustic images at the distal tip of a multimode fiber, thus paving the way for the development of minimally invasive photoacoustic endoscopes.

We first introduce the principles of digital phase conjugation through a multimode fiber and describe how this approach can be used for optical-resolution photoacoustic imaging. The proposed setup is described, and photoacoustic images of absorbing phantoms are presented. The results presented in this chapter were obtained at École Polytechnique Fédérale de Lausanne as a collaborative work during two visits, with Dr. Ioannis Papadopoulos, Dr. Salma Farahi, Prof. Demetri Psaltis and Prof. Christophe Moser. A pre-existing setup for phase conjugation through multimode fiber was adapted to perform optical-resolution photoacoustic imaging.

2.1 Background and principles

2.1.1 Digital holography

Holography principles were first discovered by D. Gabor in 1948, discovery for which he was awarded the nobel prize in physics in 1971. It was then first implemented by E. Leith and J. Upatnieks in 1962 at the University of Michigan, thanks to development of lasers that provided the necessary coherent sources. Unlike photography, holography was able to reconstruct the amplitude and phase of a coherent optical field that comes from an object and not only its intensity. In order to do so, the optical field coming from the object was mixed with a reference beam. The resulting interference pattern was recorded on a

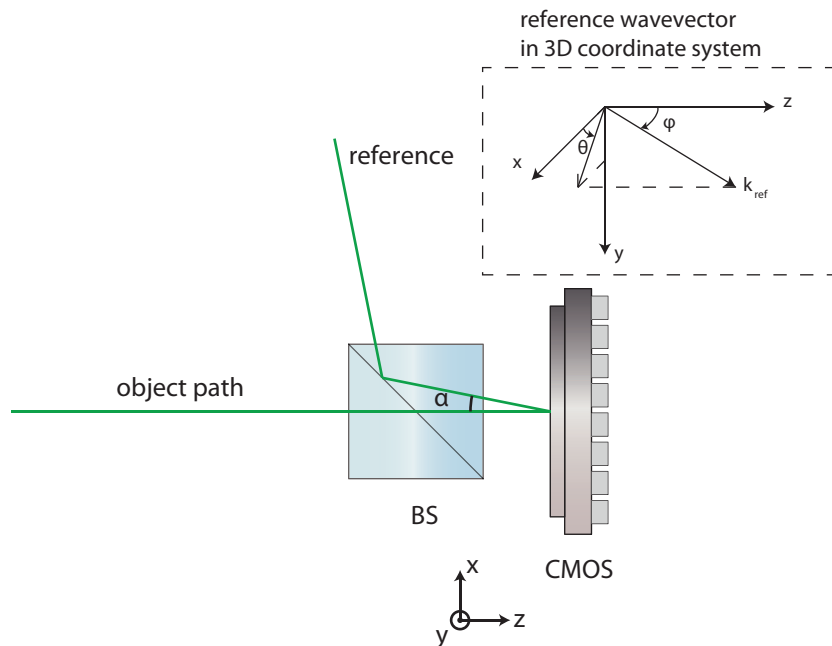


Figure 2.1 – Off-axis digital holography setup, taken from [Papadopoulos, 2014].

photographic plate, and then read-out with the same reference beam. A 3D image of the object was produced from this read-out phase.

In conventional holography, the hologram, i.e. the interference pattern of the object and reference beam, is recorded on a physical support. With the development of computers, a new type of holography emerged at the beginning of the 70s, called digital holography, where the hologram is both recorded and read numerically. At the very beginning, the holograms were first recorded conventionally and then digitized. Nowadays, the holograms are directly digitized, by use of CCD or CMOS sensors. The holograms are numerically treated inside a computer and the object field is reconstructed. Let us see how the holograms are recorded and how the object field can be numerically reconstructed from these holograms. Using the axes depicted on figure 2.1, let us consider two coherent monochromatic fields, object and reference fields, on a CMOS sensor:

$$E_o(x, y) = A_o(x, y)e^{i\phi_o(x, y)} \quad (2.1)$$

$$E_r(x, y) = A_r(x, y)e^{i\phi_r(x, y)} \quad (2.2)$$

The intensity of the hologram pattern on the sensor can be written as:

$$I = |E_o + E_r|^2 = (E_o + E_r)(E_o + E_r)^* = I_o + I_r + E_o E_r^* + E_o^* E_r \quad (2.3)$$

Because the reference beam used experimentally is a large collimated beam it can be considered as an incident plane wave on the sensor surface. Using the axis system shown on figure 2.1, and assuming a small angle is introduced between the reference beam and the object beam, we can write:

$$\begin{aligned} E_o(x, y) &= A_o(x, y) e^{i\phi_o(x, y)} \\ E_r(x, y) &= A_r e^{i\phi_r} e^{-i(k_{r,x}x + k_{r,y}y)} \end{aligned} \quad (2.4)$$

where $k_{r,x}$ and $k_{r,y}$ are reference wavevector projections on the x and y axes. $k_{r,x} = k \sin(\phi) \cos(\theta)$, $k_{r,y} = k \sin(\phi) \sin(\theta)$, with $k = \frac{2\pi}{\lambda}$, ϕ the polar angle between the wavevector of the reference and the z axis, and θ the azimuthal angle. The intensity of the hologram pattern can be written:

$$\begin{aligned} I(x, y) &= I_o(x, y) + I_r \\ &+ A_r A_o(x, y) e^{i\phi_o(x, y)} e^{i(k_{r,x}x + k_{r,y}y)} \\ &+ A_r A_o(x, y) e^{-i\phi_o(x, y)} e^{-i(k_{r,x}x + k_{r,y}y)} \end{aligned} \quad (2.5)$$

where the term $e^{i\phi_r}$ has been dropped as it only express a constant phase factor. Taking the 2D Fourier transform of the previous equation, this yields:

$$\begin{aligned} \tilde{I}(k_x, k_y) &= \mathcal{F}\{I_o(x, y) + I_r\} \\ &+ A_r \cdot \mathcal{F}\{A_o(x, y) e^{i\phi_o(x, y)}\}(k_x - k_{r,x}, k_y - k_{r,y}) \\ &+ A_r \cdot \mathcal{F}\{A_o(x, y) e^{-i\phi_o(x, y)}\}(k_x + k_{r,x}, k_y + k_{r,y}) \end{aligned} \quad (2.6)$$

The Fourier transform of the hologram intensity contains three terms. The term we are interested in is the second term that contains the information on the object field and that is translated in the Fourier plan by a spatial frequency $\mathbf{k}_{\text{off-axis}} = k_{r,x}\tilde{\mathbf{x}} + k_{r,y}\tilde{\mathbf{y}}$. The spatial separation of the three orders in the Fourier domain is achieved thanks to the off-axis configuration. The Fourier transform can thus easily be filtered to only select the second term, and we can then reconstruct the object field on the CMOS sensor by applying

an inverse Fourier transform:

$$E_{reconstruct}(x, y) = A_r \cdot A_o(x, y) e^{i\phi_o(x, y)} e^{i(k_{r,x} \cdot x + k_{r,y} \cdot y)} \quad (2.7)$$

From this reconstructed field we can extract the reconstructed amplitude and phase of the object field:

$$\begin{aligned} A_{reconstruct}(x, y) &= A_r \cdot A_o(x, y) \\ \phi_{reconstruct}(x, y) &= \phi_o(x, y) + k_{r,x} \cdot x + k_{r,y} \cdot y \end{aligned} \quad (2.8)$$

The amplitude of the reconstructed field has to be divided by $A_r = \sqrt{I_r}$ to be equal to the amplitude of the object field on the sensor. This can easily be achieved by measuring the intensity of the reference beam on the sensor, by blocking the object beam and acquiring an image on the sensor to measure its intensity. The phase of the reconstructed object field is composed by the phase of the object field with an added grating defined by the angle introduced on the reference beam. The grating component could be eliminated, to recover the exact phase of the object (see figure 2.6), however we will see in that in practice we can take advantage of it to facilitate the digital phase conjugation system alignment.

2.1.2 Phase conjugation by use of an SLM

We consider a linear, isotropic, lossless dielectric media through which an electromagnetic wave propagates. In such media, the wave equation for the electric field $\mathbf{E}(\mathbf{r}, t)$ can be written as:

$$\Delta \mathbf{E}(\mathbf{r}, t) - \frac{\epsilon(\mathbf{r})}{c^2} \frac{\partial^2 \mathbf{E}(\mathbf{r}, t)}{\partial t^2} = \mathbf{0} \quad (2.9)$$

where $\epsilon(\mathbf{r})$ is the relative permittivity at position \mathbf{r} and c is the speed of light in vacuum.

Assuming linearly polarized monochromatic waves,

$$E(\mathbf{r}, t) = \mathcal{A}(\mathbf{r}) e^{i\omega t} \quad (2.10)$$

with $\mathcal{A}(\mathbf{r}) = A(\mathbf{r}) e^{i\phi(\mathbf{r})}$.

Equation 2.9, can be written as:

$$\Delta \mathcal{A}(\mathbf{r}) + \frac{\epsilon(\mathbf{r})\omega^2}{c^2} \mathcal{A}(\mathbf{r}) = 0 \quad (2.11)$$

Taking the complex conjugate of this equation gives:

$$\Delta \mathcal{A}^*(\mathbf{r}) + \frac{\epsilon(\mathbf{r})\omega^2}{c^2} \mathcal{A}^*(\mathbf{r}) = 0 \quad (2.12)$$

$\mathcal{A}(\mathbf{r})$ and $\mathcal{A}^*(\mathbf{r})$ are solutions to the same Helmholtz equation, thus the fields $E(\mathbf{r}, t) = \mathcal{A}(\mathbf{r})e^{i\omega t}$ and $E_c(\mathbf{r}, t) = \mathcal{A}^*(\mathbf{r})e^{i\omega t}$ are solutions to the same wave equation 2.9. E_c is called the phase-conjugate field of the field E , it can be created from the field E by using what is called a phase conjugating mirror. Physically, the fact that E and E_c are solutions to the same wave equation means that, if E_c is created from the reflection of E on a phase conjugating mirror, it will back-propagate following the exact same path as E and have at every point in space the same complex amplitude.

We now write the full expression of both fields to get a better understanding of the physical meaning of both fields. $E(\mathbf{r}, t)$ can be written as,

$$E(\mathbf{r}, t) = A(\mathbf{r})e^{i\phi(\mathbf{r})}e^{i\omega t} \quad (2.13)$$

and $E_c(\mathbf{r}, t)$,

$$E_c(\mathbf{r}, t) = A(\mathbf{r})e^{-i\phi(\mathbf{r})}e^{i\omega t} \quad (2.14)$$

$E_c(\mathbf{r}, t)$ and $E(\mathbf{r}, t)$ are very similar fields. They have an opposite phase, but similar circular frequencies and amplitudes. Thus they correspond to counter-propagating fields, that have the same amplitude and overlapping wave-front at every space location. $E_c(\mathbf{r}, t)$ can simply be obtained from $E(\mathbf{r}, t)$ by changing the time variable sign, i.e. t into $-t$, as can be seen from equations 2.10 and 2.14. Phase conjugation is therefore also often referred to as time reversal. The fact that $E(\mathbf{r}, t)$ and $E_c(\mathbf{r}, t)$ are solutions to the same wave equation can be very useful. A field propagating in a turbid media can indeed be phase conjugated at the exit of the turbid media so that it will back-propagate inside, and yields after back-propagation the exact same field as the field that was originally input at the entrance of

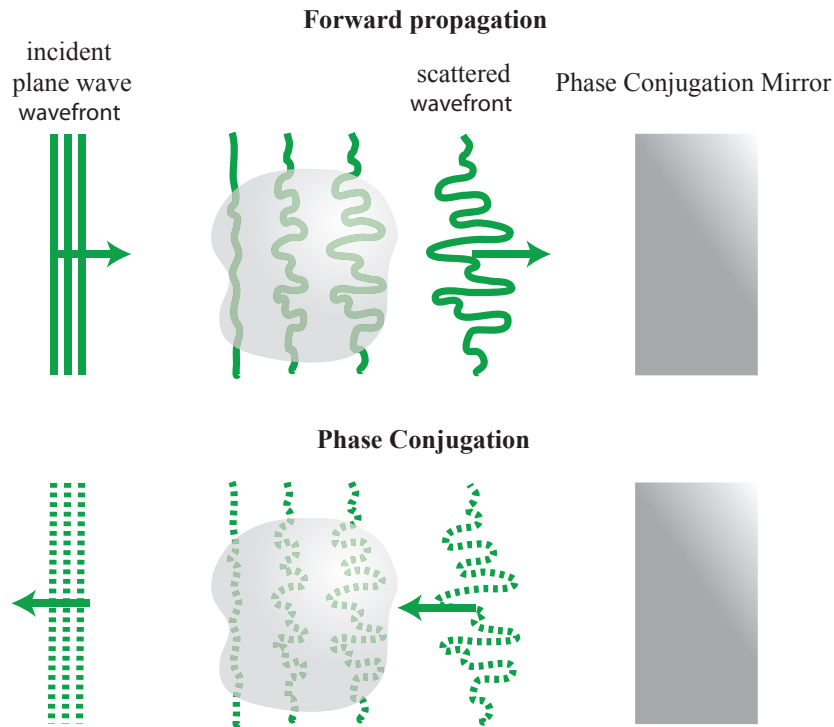


Figure 2.2 – Phase conjugation principle, taken from [Papadopoulos, 2014].

the turbid media (see figure 2.13).

Digital phase conjugation (DPC) is the digital implementation of phase conjugation. It can be achieved by the combination of digital holography, and the use of a phase-only reflection spatial light modulator (SLM). A phase-only reflection SLM can be used to create a wave with the desired phase pattern. In order to do so, the desired 2D phase pattern is assigned to the SLM, a plane wave is reflected upon it, so that the phase of the reflected wave is the phase that was assigned to the SLM. Phase modulation on the SLM is achieved by liquid crystal-based pixels, usually at least 512 by 512 pixels. The plane wave used is the reference beam that was used to create the hologram, and the phase assigned to the SLM is the opposite of the phase of the reconstructed object beam, see Eq. 2.8.

The implementation of the phase conjugation setup is depicted on figure 2.3. The reference beam is divided into two beams thanks to a non-polarizing beamsplitter and one of the beam is sent and reflected on the SLM. The x,y,z axis of figure 2.3 corresponds to the 90° tilted version of the x,y,z axis of figure 2.1 along the y axis. The SLM is tilted slightly so that its surface is perpendicular to the incoming reference beam. The x',y',z' axis is the axis attached to the SLM surface.

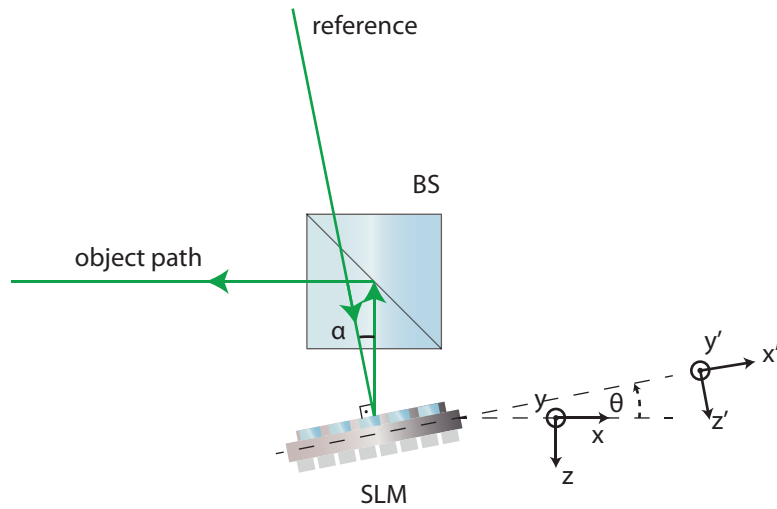


Figure 2.3 – Phase-modulation setup, taken from [Papadopoulos, 2014].

After reflection of the reference beam on the SLM surface, the reflected field can be written:

$$E_{conjugate}(x', y') = A_r e^{-i\phi_o(x', y') - k_{r,x}x' - k_{r,y}y'} \quad (2.15)$$

This is the reflected field on the surface of the SLM. It corresponds to a field propagating with an angle to the SLM surface normal equals to the angle introduced on the reference beam during hologram recording process. Thus the reflected field is propagating in the $-z$ direction, with a phase that is the opposite of the object field phase.

To create a phase conjugated beam that will back propagate as shown by equations 2.11 and 2.12, the phase conjugated beam has to be created at the exact location of the original beam. This means that the SLM has to be at the exact same location as the CMOS sensor. Thus the SLM has to be aligned so that each of its pixel match the pixels on the CMOS sensor. This alignment is very crucial and is made easier by the fact that the phase projected on the SLM still contains the information on the angle introduced during the off-axis digital holography recording. Indeed the alignment is then based on the angular alignment of the SLM perpendicular to the reference beam which can quite easily be done using an iris and the back-reflection of the reference beam on the unmodulated SLM surface. A detailed description of the alignment process can be found in [Papadopoulos, 2014].

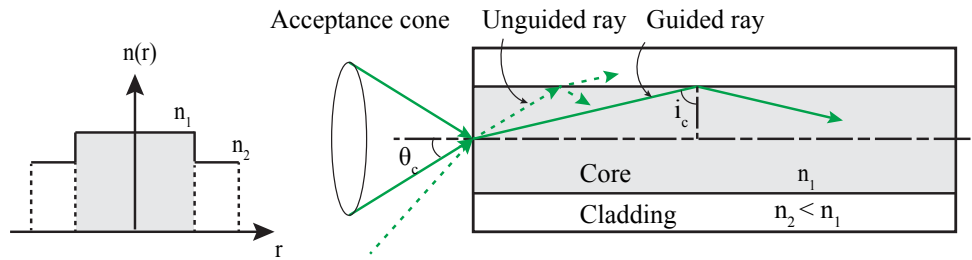


Figure 2.4 – Step-index fiber principle.

2.1.3 Focusing and scanning through a multimode fiber

Optical fibers are dielectric cylindrical optical waveguides. They are typically composed of a core, with a refractive index n_1 , and a surrounding cladding, with a refractive index $n_2 < n_1$. The optical fibers considered in this chapter, unless otherwise stated are step-index fibers. The two refractive indexes in a step-index fiber are homogeneous in both the core and the cladding.

To correctly describe the wave propagation of the electromagnetic field in an optical fiber, one should write the Maxwell's equations in the guide, both in the core and in the cladding, and apply the appropriate boundary conditions. The corresponding derivation can be found in most optics books dealing with optical fibers, such as [Saleh and Teich, 2007], and will not be given here. Solving the corresponding equations shows that in an optical fiber, light propagates as modes. Each mode is characterized by its propagation constant, its transverse spatial distribution of the electromagnetic field, and its polarization.

Although the exact description of the propagation of an optical field requires the use of the electromagnetic theory, a simple geometrical approach can give some useful results and a basic understanding of the propagation of waves inside an optical fiber (see figure 2.4). An optical wave is guided and trapped inside the core of an optical fiber thanks to total internal reflection at the core-cladding interface. This occurs if the incident angle of a light ray at the core-cladding interface is greater than the critical angle $i_c = \arcsin(\frac{n_2}{n_1})$. For smaller incidence, the light rays are partially reflected and partially transmitted, and are thus not confined in the core. This conditions for total internal reflection can be written for the incident angle of a light ray on the input facet of an optical fiber and indicate that only light rays with incident angle *smaller* than $\theta_c = \arcsin(\sqrt{n_1^2 - n_2^2})$ will be guided by

the optical fiber. Thus we can easily define the numerical aperture of the fiber as

$$\text{NA} = \sqrt{n_1^2 - n_2^2} \quad (2.16)$$

The number of modes that can be guided by an optical fiber depends on a dimensionless parameter V , defined as

$$V = 2\pi \frac{a}{\lambda_0} \text{NA} \quad (2.17)$$

where a is the optical fiber core radius. It can be shown, [Saleh and Teich, 2007], that the number of supported modes, provided it is big enough, can be written as:

$$M \approx \frac{4}{\pi^2} V^2 \quad (2.18)$$

What was detailed above is the number of modes an optical fiber can support. However, each incident optical field at the input of the fiber will be coupled differently to the different modes, depending on the spatial overlap between the optical field and the mode.

Optical fibers that support only one mode are called single mode fibers. Optical fibers that support more than one mode are called multimode fibers. single mode fibers are well suited for communications purpose, optical propagation inside them is easier and they dominate the optical fiber market. However, the use of single mode fibers for imaging purpose is limited to the use of optical fiber bundle, that are limited in term of miniaturization and resolution as discussed in the first chapter of this manuscript (see chap.1). Multimode fibers have the ability to be used as high resolution miniature imaging device, however this require some extra work as the optical propagation inside multimode fiber is quite complex.

In a multimode fiber each mode has its own propagation constant. Therefore the propagating wave is modified during its propagation and projecting the output of the fiber on a screen one would generally see a speckle-like pattern due to phase differences between the interfering modes. In an ideal multimode fiber, each mode propagates independently and one could imagine building a device that would be able to compensate the phase of the different modes. However in real-life multimode optical fiber, energy from one mode can be transferred to an other mode due to random impurities in the fiber, fiber bending

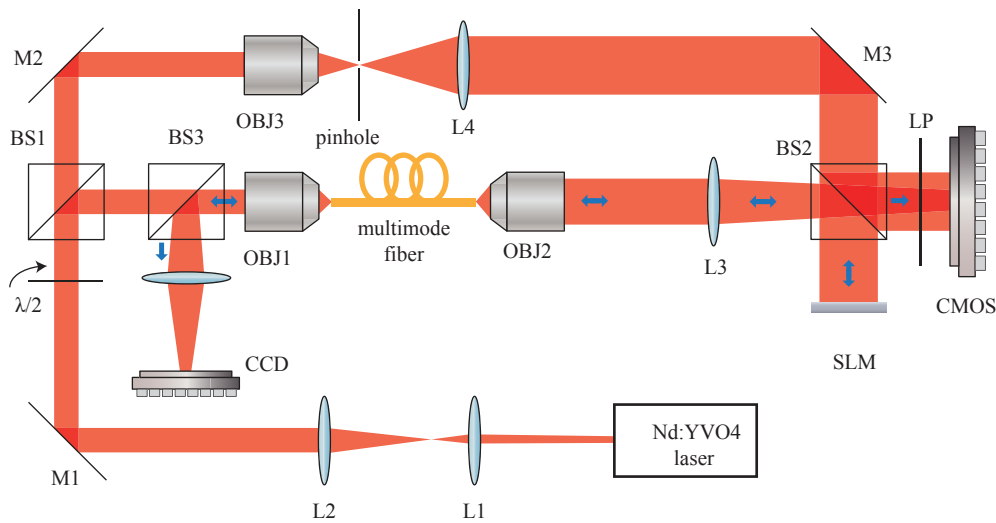


Figure 2.5 – Experimental setup for the implementation of DPC for light focusing through a multimode fiber, taken from [Papadopoulos et al., 2012].

or temperature changes. This mode coupling is also called mode mixing. The output of a real-life multimode fiber is thus a speckle-like pattern that depends on a great number of parameters related to mode mixing (see figure 2.6).

This multimode propagation and mode mixing can be "undone" by the digital phase conjugation (DPC) approach that was presented in the previous section, for example to focus and scan a small optical spot at one end of the fiber. The setup is presented in details in [Papadopoulos et al., 2012] and depicted in figure 2.5. The general idea of the setup will be presented here. The output of a laser is separated in two beams by a polarizing beamsplitter, a reference beam, and an object beam. The object beam is focused by a microscope objective close to the facet of a multimode fiber, and then propagates through the fiber. After propagation through the fiber, the object and reference beam are recombined to interfere on a CMOS sensor where the off-axis hologram is recorded, treated and stored inside a computer, as described in the previous section. This can be done for different positions of the focused spot at the optical fiber facet. This is called the calibration phase. Once this has been done, one can focus light through the multimode fiber on any of the positions for which a digital hologram had been stored. To do so, the SLM is assigned the correct phase pattern, and the phase conjugated beam is created by reflecting the reference on the SLM as described in. This is called the focusing and scanning phase.

In the setup depicted in figure 2.5, a half-wave plate is placed before the polarizing beam-

splitter (BS1) to control the power ratio between the reference and the object beam. The combination of a microscope objective (OBJ3), a lens (L4), and a pinhole is used to filter and expand the reference beam. Combined with the focusing objective (OBJ1), a non-polarizing beamsplitter (BS3), a lens (L5), and a CCD sensor are used to observe the input plane of the multimode fiber and thus the quality of the focused spot. An objective (OBJ2) combined with a lens (L3) is used to image the output facet of the multimode fiber on the CMOS sensor, and the SLM surface on that same output facet. A linear polarizer (LP) is placed in front of the CMOS sensor to optimize the contrast of the hologram. Two lenses (L1, and L2) are used to expand the output beam of the laser.

The output of a multimode fiber is usually a speckle-like pattern, as explained earlier in this section. However, based on the setup just described, one can focus an optical spot at the output of a multimode fiber (see figure 2.6). The size of the smallest spot that can be achieved as well as the amount of energy concentrated in the spot location depends on two different but related parameters. As with any imaging device, the spot size is limited by the numerical aperture of the fiber.

$$\text{minimum spot FWHM} = \frac{0.51\lambda}{\text{NA}} \quad (2.19)$$

This minimum spot FWHM is approximately $0.5 \mu\text{m}$ for the laser and the fiber used in this chapter experiments ($\lambda = 532 \text{ nm}$, 0.53 NA). The effective numerical aperture of the fiber depends on the focusing position so that as this position is moved away from the fiber facet, and towards the edges of the fiber acceptance cone, the minimum focused spot size achievable increases (see [Papadopoulos et al., 2013b]).

The focusing efficiency, defined as the amount of optical energy concentrated in the focused spot region compare to the amount of optical energy in the background, is dictated among others, by the number of degrees of freedom of the system. In our experiment, where the SLM and the CMOS sensor have much more pixels (more than 1 million each) than the number of supported modes in the fiber (about 190000 for a 532 nm laser, $220 \mu\text{m}$ diameter, 0.53 NA fiber, based on equations 2.17 and 2.18), this was defined by the number of excited modes in the fiber. This number depends on the incident optical field sent into the fiber, and has an upper limit given by the number of supported modes in the fiber (see [Papadopoulos et al., 2012, 2013a]).

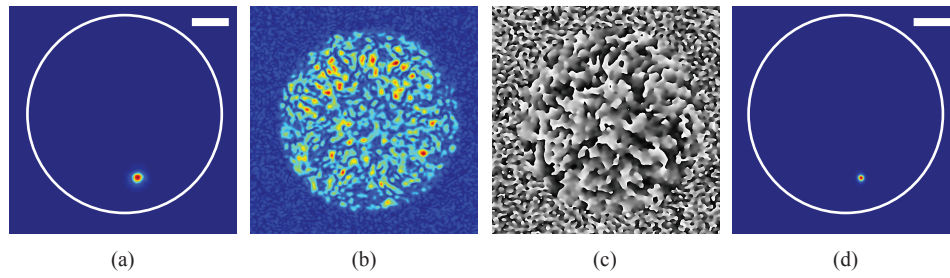


Figure 2.6 – Demonstration of DPC for light focusing through a multimode fiber. (a) Calibration phase excitation focused spot, (b) speckle pattern at fiber output, (c) calculated phase (phase grating due to off-axis digital holography configuration removed), (d) phase-conjugated focused spot on the fiber facet input. Scale bar in (a) and (d) is $20\ \mu\text{m}$. The white circle defines the fiber core outline and the images are normalized to their maximum value. Taken from [Papadopoulos et al., 2012].

2.1.4 Optical-resolution photoacoustic microscopy

As introduced in the first chapter, photoacoustic imaging can provide optical-resolution images of tissue, with a micron scale resolution, and is often referred to in this regime as OR-PAM, for optical-resolution photoacoustic microscopy. However, OR-PAM relies on the ability to focus light in the imaging plane of interest to a diffraction limited spot, typically with diameters of a few microns. Thus, the imaging depth of OR-PAM is limited to less than typically 1 mm because of light scattering in tissues. To overcome the issue of light focusing and scanning at depth in tissue, one approach is to insert a multimode fiber deep in the tissue. If a proper calibration has been done before the insertion of the fiber in the tissue, the light can be focused and scanned at the distal tip of the fiber deep in tissue by DPC, with no need for any optical lenses or mechanical actuator. This process would require the optical fiber to undergo minimum bending during the insertion in the tissue. This could be solved by fixing the fiber inside a needle, and then carefully inserting the needle inside the tissue, see [Papadopoulos et al., 2013b]. This needle-type endoscope would be minimally invasive as the fiber diameter is quite small, about $200\ \mu\text{m}$. In the proposed configuration the acoustic waves could be detected by a transducer placed outside the tissue. More details on the acoustic detection will be given in the following chapter (see chap. 3).

In this chapter we demonstrate the feasibility of using DPC to scan and focus light through a multimode fiber to generate an OR-PAM image at the distal tip of the multimode fiber.

Now that most of the physical principle underlying the experiments described in this chapter have been presented, we make a few remarks concerning the difference between the phase conjugation setup used in this chapter and the ideal phase conjugation principle presented at the beginning of section 2.1.2. There are three main remarks that can be made here and that are worth bearing in mind.

1. An ideal phase conjugation setup would phase conjugate both polarization components of the optical field. In the setup depicted in figure 2.5, only one polarization component of the optical field is phase conjugated. This is due to the fact that the SLM used is only able to achieve phase-only modulation on a linearly polarized optical field. This is part of the reason why phase conjugation was explained in the previous section 2.1.2 assuming a linearly polarized optical field. In the setup described in figure 2.5, the reference and the object beam, although created with orthogonal polarization, can interfere on the CMOS sensor because of the depolarization effect of multimode fiber. Phase conjugation of both polarization components would improve the phase conjugation efficiency [McMichael et al., 1987] but would require to double the digital holography and phase conjugation part of the setup.
2. If one looks at the definition of a phase conjugated field given in section 2.1.2 and the expression of the phase conjugated field created on the SLM surface in equation 2.15, one would remark that the amplitude of the phase conjugate field created is the amplitude of the reference beam reflecting on the SLM and not the amplitude of the object beam as it should be. This is due to the fact the SLM is used to achieve phase-only modulation but not to modulate the amplitude. Once again, amplitude modulation combined with phase modulation would improve the phase conjugation efficiency but would require more material [Shibukawa et al., 2014].
3. An optical field propagating in an optical fiber undergoes dispersion. More explanation about dispersion in an optical fiber can be found in [Saleh and Teich, 2007]. However, the main idea is that in an optical fiber, the different modes and frequency components of the optical field might propagate with different propagation constants. One of the consequence of this effect is that the dispersion has to stay small enough compare to the coherence length of the optical field. This conditions has to be verified for a contrasted speckle pattern to be obtained at the output of the optical fiber. In a multimode fiber the dispersion is mainly due to the modal dispersion. Going back to the geometrical approach of optical propagation in multimode fibers,

the dispersion can easily be estimated by the difference in path length between the first order mode that propagates along a straight line and the highest order mode that enters the fiber with the maximum angle supported by the numerical aperture. A simple geometrical computation shows that the difference between these two path length is given by:

$$\Delta z = n_1 L_{fiber} \left(\frac{1}{\cos(\arcsin(\frac{NA}{n_1}))} - 1 \right) \quad (2.20)$$

where L_{fiber} is the fiber length.

Taking $n_1 = 1.46$, $L_{fiber} = 1$ m and $NA = 0.53$ yields that the coherence length of the laser has to be greater than $\Delta z \approx 0.1$ m which is a reasonable coherence length for a diode-pumped solid-state laser source and which was the case in our experiments.

2.2 Materials and methods

2.2.1 Experimental setup

The setup used to demonstrate OR-PAM imaging by use of a multimode fiber (220 μm diameter, 0.53 NA multimode fiber, Ceramoptec, USA) is depicted in figure 2.7. It is a modified version of the setup of figure 2.5. On figure 2.7 only the focusing and scanning part is represented, not the calibration phase. In this setup the distal tip of a multimode fiber is inserted through the bottom of a specially designed water tank.

The initial step is the calibration phase as explained earlier in this chapter. A high numerical aperture objective (40x, 0.65 NA, OBJ1 of figure 2.5, not shown on figure 2.7) is used to focus the output of a Q-switched Nd:YVO4 laser (wavelength 532 nm and pulse width of 5 ns, NL-201, EKSPLA, Lithuania) on a diffraction limited spot 250 μm away from the distal tip of the fiber. The optical field then propagates inside the fiber and generates a speckle pattern at the output of the fiber. This speckle pattern is imaged by a high numerical aperture objective (40x, 0.65 NA, OBJ2) and a lens (20 cm focal length, L3) on the CMOS sensor (MV1-D1312(IE)-G2, CMOS camera, Photonfocus, Switzerland) and analyzed by digital holography as described earlier so the associated phase is retrieved and stored in a computer. This process is repeated for 17956 positions of the focused spot

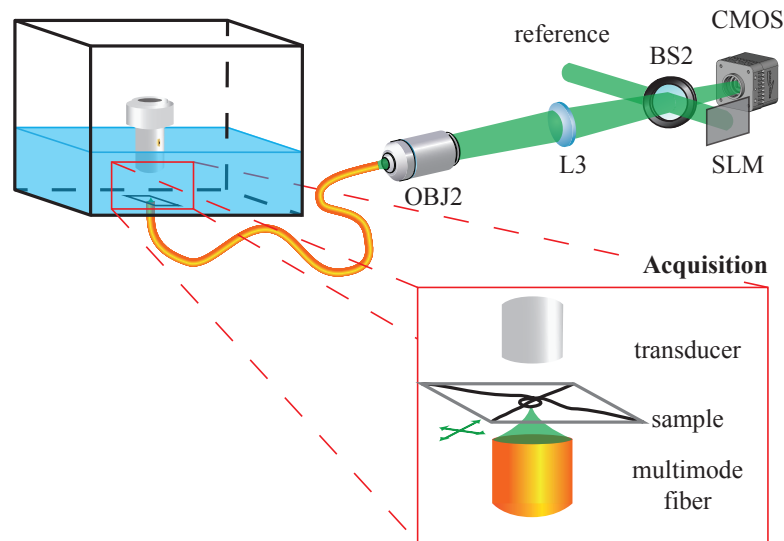


Figure 2.7 – Experimental setup for OR-PAM imaging using a multimode fiber.

spread over a 134 by 134 positions grid. The grid step is $1.5\ \mu\text{m}$ thus yielding a 201 by 201 μm grid. The spot size at each position is about $1.2\ \mu\text{m}$, and the energy per pulse was measured at 20 nJ/pulse.

The next step is the imaging step where the focused spot is raster scanned over the 201 by 201 μm grid by $1.5\ \mu\text{m}$ steps by successively applying the previously stored phase patterns on the SLM (Pluto-NIR II, Holoeye, Germany). For the imaging part of the experiment, the water tank is filled with degassed water and the microscope objective is replaced by a spherically focused high frequency transducer (20 MHz, spherically focused, 12.7 mm focal distance, 6.3 mm diameter, PI20-2-R0.50, Olympus, Japan). The transducer is kept fixed during the OR-PAM imaging part of the experiment. Acoustic focusing is here only used to enhance sensitivity, not to define the image resolution. The presence of water at the proximal tip of the fiber changes the working distance, defined as the focusing distance away from the fiber tip, but not the distance between adjacent focused spots.

The sample in this experiment consists of two nylon threads (20-30 μm nominal diameter, NYL02DS, Vetsuture, France) tied into a knot and placed at the working distance away from the fiber, as show in the inset of figure 2.7. For each position of the focused optical spot, acoustic waves are detected by the transducer, and the resulting electric signal is amplified by a low noise amplifier (DPR500, remote pulser RP-L2, JSR Ultrasonics, USA), displayed on a oscilloscope, transferred and stored in the computer for the image acqui-

sition. The same computer is used to synchronize all the required actions by sequentially projecting the phase on the SLM for the generation of the focus, then acquiring the data from the transducer through the oscilloscope and repeating these steps for the scanning and acquisition of the image.

2.2.2 Procedure

A rigorous procedure has to be followed for the experimental setup just described to be correctly implemented.

The calibration phase is achieved with no water in the water tank. The water tank is then partially filled with water, the objective used to produced the calibration phase focused spot, is replaced by a long focal, low numerical aperture objective (20x, 0.35 NA), to image the focusing plane at the proximal tip of the fiber. White light is used to illuminate the sample, and while a focused spot is projected at the center of the 201 by 201 μm field of view, the sample is adjusted at the correct distance from the fiber and at the correct position in the field of view, using the imaging system composed of the long focal objective and the lens L5 (20 cm focal length) and CCD sensor (TXF-14, CCD camera, Baumer, Switzerland) of figure 2.5 (not show on figure 2.7). A conventional optical image is acquired on the camera for later comparison with the OR-PAM image. Once this is done, the objective is replaced by the ultrasound transducer, and more water is carefully added in the water tank to prevent any motion of the sample. Once this is done the transducer position is adjusted so that the sample is in its focal region. This is done by adjusting the transducer vertical position and by acquiring a pulse echo image of the sample by raster scanning of the transducer. Once everything is aligned, the OR-PAM imaging part of the experiment can start.

The calibration phase where all the required holograms are acquired and treated takes about 45 minutes. The imaging part of the experiment is quite long, more than an hour, but is due to the slow data transfer rate between the oscilloscope and the computer, and could ultimately be limited by the refreshing rate of the SLM, 20 Hz, and the combination of the photoacoustic signal averaging, 16, and the laser repetition rate, 1 kHz. Taking the SLM refreshing rate as the limiting imaging speed parameter yields an approximate imaging time of 15 minutes.

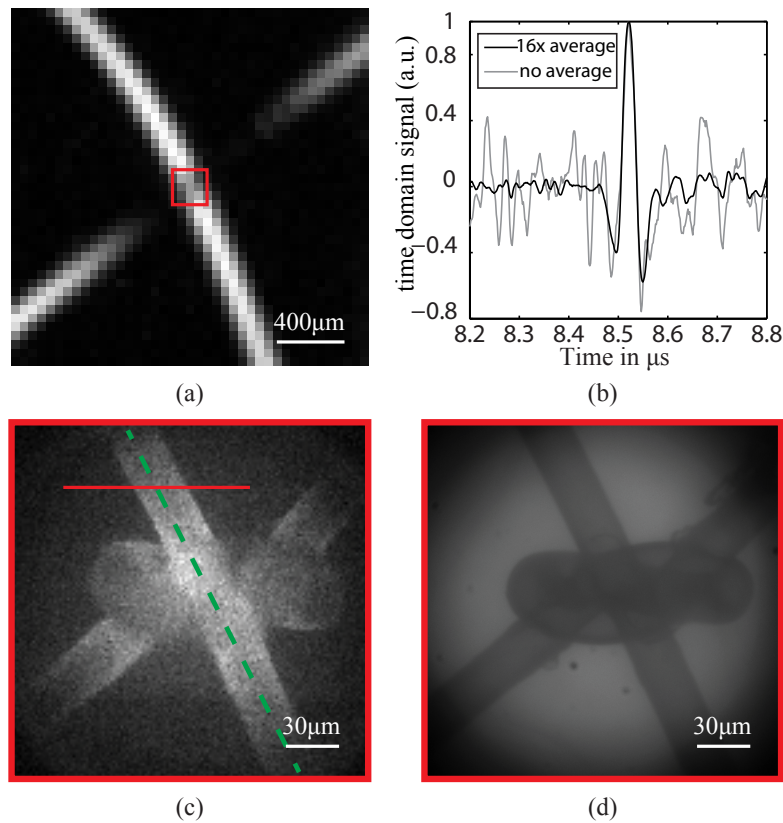


Figure 2.8 – Images and signals obtained with the setup presented in section 2.2. (a) Pulse-echo image, (b) OR-PAM signals, (c) OR-PAM image, (d) white light optical image. The fields of view of images (c) and (d) are the same, and correspond to the red square in image (a).

2.3 Results

2.3.1 Photoacoustic images

The images and signals obtained using the setup described previously are shown in figure 2.8. The pulse-echo image, captured by sequential raster scanning of the transducer, is presented in figure 2.8(a). As introduced earlier in chapter 1, the resolution in this now acoustic-resolution photoacoustic microscopy approach is defined by the central frequency and the aperture of the transducer. This yields a $2\omega_0$ parameter for the transducer Gaussian-like focal region transverse profile of approximately $200\ \mu\text{m}$. This can clearly be seen as the $30\ \mu\text{m}$ diameter threads appear as thick structures and no details of the knot can be resolved. The pixel size of the image is $50\ \mu\text{m}$. The time-domain acoustic signal

captured by the transducer when the light emerging from the multimode fiber is focused on the wires is presented in figure 2.8(b). The grey line corresponds to the raw electric signal from the transducer, while the black line is the result of 16 times averaging. The non-averaged signal has a SNR of 6, which rises to 25 when 16 times averaging is performed. The SNR level of the non-averaged signal is sufficient to allow the acquisition of images with just a single pulse. The OR-PAM image obtained by DPC scanning of the focused spot and energy measuring of the 16 times averaged acoustic signals is shown in figure 2.8(c). The image is acquired 250 μm away from the fiber tip, the pixel size is 1.5 μm , the field of view is 201 by 201 μm , and reveals the details of the knots thanks to a level of details much higher than in figure (a). A white light optical image acquired with a 20x, 0.35 NA microscope objective is shown in figure 2.8(d). We can see that the OR-PAM image gives a high quality image closely resembling the white light optical image. The imaging plane is set exactly at the plane of the wires and the rendered 2-d image illustrates the 3-d structure of the knot.

2.3.2 Estimation of the resolution

Some interesting information on the system resolution, collection and phase conjugation efficiencies can be extracted from the OR-PAM image of figure 2.8.

Drawing a cross-sectional plot along the threads, the resolution of the system can be estimated. To avoid the need to interpolate the acquired data, which would cause the generation of artifacts, a cross-sectional plot is drawn horizontally across the raster scanning, not exactly perpendicular to the wires therefore resulting in an underestimation of the achieved resolution. The cross-sectional plot along the solid red line in figure 2.8(c) is shown on figure 2.9(a). As can be seen in figure 2.9(a) the transition between the background signal to the signal from the wire, occurs within 1 pixel of the image (1.5 μm), therefore defining the upper limit of the resolution to 1.5 μm .

A cross-sectional plot can also be used to characterize the collection efficiency of the system. To do so the cross-sectional plot along the dashed green line in figure 2.8(c) is drawn in figure 2.9(b). As can be seen in figure 2.9(b) the collected signal is weaker towards the edges of the image. Performing a curve fitting with a Gaussian profile shows that the fitted curve has a $2\omega_0$ parameter equal to 200 μm , which corresponds well to the calculated $2\omega_0$ parameter of the focused transducer. Therefore, the different levels of the collected signal

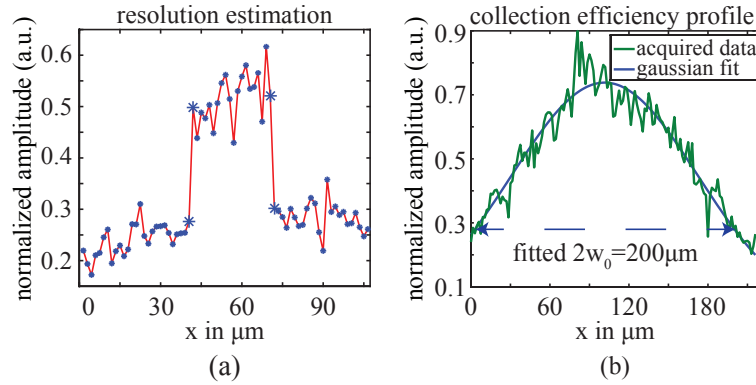


Figure 2.9 – Resolution and collection efficiency estimation of the system.

between the center and the edges of the image are attributed to the Gaussian-like collection efficiency of the focused ultrasound transducer.

Using the plot in figure 2.9(a), we can see that the contrast of the OR-PAM image, i.e. the ratio between the energy of the photoacoustic signal from the thread and that from the background photoacoustic signal is approximately 2. Although the OR-PAM image is of very high quality, its contrast is lower than the contrast of the OR-PAM images shown in the next chapter. This can be attributed to the optical energy that is still present outside of the optical focus region, due to the imperfectness in the phase conjugation process (see section 2.1.4).

2.4 Conclusion

It was shown that digital phase conjugation could be used to generate optical-resolution images at the distal tip of a multimode fiber. Images of a knot made by two absorptive threads immersed in a water tank were obtained with a resolution better than $1.5 \mu\text{m}$ across a $201 \times 201 \mu\text{m}$ field of view.

This work presents several limitations. First, the phase look-up table calculated for the focusing and the scanning of the light field after the multimode fiber are only valid for a given conformation of the fiber. In case the fiber changes conformation (bending), the phase look-up table has to be recalculated. Second, in the presented setup the samples were imaged in a water tank. In the context of tissue imaging, the generated photoacoustic waves would undergo a significant attenuation as they propagate through tissue because of the

strong acoustic attenuation coefficient of biological tissues at the high frequencies generated in OR-PAM. A third limitation that could deteriorate the imaging performance in the context of tissue imaging is the fact that once inserted in the tissue the medium between the imaging plane and the fiber facet is not the same anymore as during the calibration phase. Although this is true, the situation is similar to what happens when doing OR-PAM with a microscope objective and therefore the quality of the optical focusing should not be degraded significantly.

Although interesting work is being done to achieve fiber bending compensation [[Farahi et al., 2013](#); [Caravaca-Aguirre et al., 2013](#)], the performance required for the development of a flexible endoscope still remains out of reach for the moment. A rigid configuration can be considered based on the insertion of the fiber in a rigid jacket, to create ultra-thin needle-type endoscopes. Fortunately it was shown that in this type of setup the fiber sensitivity to movements is not too critical and thus the rigid endoscopic approach can be effective in practical conditions (see [[Papadopoulos et al., 2013b](#)]).

Overcoming the penetration depth limitation due to the strong acoustic attenuation in biological tissues is a remaining challenge. One of the possible solutions could be to do a piezoelectric or optical detection of the acoustic waves at the distal tip of the capillary. In the following chapter, a novel approach is proposed to overcome the penetration depth limitation due to the strong acoustic attenuation in biological tissues at the high acoustic frequencies generated in OR-PAM.

Chapter 3

Photoacoustic sensing through a water-filled capillary

Contents

3.1	Background and principles	53
3.1.1	Acoustic attenuation	53
3.1.2	A silica capillary as an acoustic guide	57
3.2	Proof of principle	61
3.2.1	Materials and methods	61
3.2.2	Results	64
3.2.3	Conclusion	66
3.3	Some properties of the capillary as an acoustic waveguide . .	66
3.3.1	Materials and methods	67
3.3.2	Results	69
3.3.3	Discussion	73
3.4	Current work and perspectives	81
3.4.1	A silica capillary as an optical waveguide	81
3.4.2	Experimental Setup	84
3.4.3	Results	85
3.5	Conclusion	86

In the previous chapter, it was demonstrated that digital phase conjugation could be used to generate OR-PAM images at the distal tip of a multimode fiber. It was however then underlined that provided that a focus spot could be scanned at depth in tissue by minimally invasively inserting the multimode fiber inside the tissue, the high frequency photoacoustic waves generated would undergo significant acoustic attenuation during their propagation towards the tissue surface. One solution to overcome this issue is to detect the generated photoacoustic waves at the distal tip of the fiber. This solution would require the miniaturization of the acoustic detectors, thus reducing their sensitivities, especially for piezoelectric transducers, and demanding dedicated technological developments. Here we propose a novel approach that consists in guiding the high frequency photoacoustic waves outside the tissues for remote ultrasound detection.

The main objective of this chapter is to demonstrate that a water-filled silica capillary could be used, coupled with the digital phase conjugation setup described in the previous chapter, to acquire OR-PAM images at several centimeters depths in biological tissues. This could be a significant progress towards the development of minimally invasive optical-resolution photoacoustic endoscopes. We first explain the principles underlying the use of a water-filled silica capillary as a high frequency acoustic waveguide. The ability of such a capillary to transmit an optical-resolution photoacoustic image through several centimeters of a strong acoustic attenuation tissue is then demonstrated. Next, various properties regarding acoustic waves transmission and collection of the capillary are investigated. Finally, the ability of the capillary to guide both light and ultrasound for photoacoustic excitation and sensing is demonstrated.

3.1 Background and principles

3.1.1 Acoustic attenuation

Attenuation coefficient

Analog to the case of optical attenuation, the attenuation of acoustic waves within a macroscopically homogeneous medium is usually reflected by an attenuation coefficient in the following law for plane wave propagation:

$$P(x) = P(0) \cdot e^{-\alpha x} \quad (3.1)$$

where $P(x)$ is the pressure amplitude of the acoustic wave at position x and α is the acoustic attenuation coefficient expressed in Np per unit length. This attenuation can also be expressed with a similar equation:

$$P(x) = P(0) \cdot 10^{\frac{\alpha_{dB}}{20} x} \quad (3.2)$$

where α_{dB} is the acoustic attenuation coefficient expressed in dB per unit length. α and α_{dB} are related to one another by the following relations:

$$\begin{aligned} \alpha &= \frac{\ln(10)}{20} \cdot \alpha_{dB} \approx 0.12 \alpha_{dB} \\ \alpha_{dB} &= \frac{20}{\ln(10)} \cdot \alpha \approx 8.7 \alpha \end{aligned} \quad (3.3)$$

For any type of medium, α is a function of frequency, which depends on the type of attenuation involved. As for optics, attenuation may result from absorption and/or scattering phenomena. In the following paragraphs, we provide and discuss orders of magnitude for the acoustic attenuation of pressure waves in tissue and water, as a justification for the use of the capillary acoustic waveguide introduced in this chapter.

Acoustics attenuation in tissue

In tissue, the acoustic attenuation of pressure waves originates from both absorption and scattering phenomena, and remains difficult to predict theoretically. However experimental data are available and show that the acoustic attenuation is very dependent on the tissue type and state. As a first approximation, for a living tissue it has been observed that the acoustic attenuation at body temperature is close to being proportional to the acoustic frequency and on the order of 0.5 to 2 dB cm⁻¹ MHz⁻¹ [Grigoriev and Meilikhov, 1997; Szabo, 2004].

Acoustics attenuation in water

In water, the acoustic attenuation is due to viscosity and thermal conduction, and can be predicted theoretically: an acoustic wave is associated with the propagation in the fluid of a temperature and velocity disturbance. The temperature disturbance creates heat flows between fluid particles, while the velocity disturbance creates frictions between fluid particles. Because of those two irreversible processes the entropy of the fluid increase, and thus the mechanical energy associated with the acoustic wave decreases.

It can be shown that the acoustic attenuation of pressure (compressional) waves in a viscous and thermally conductive fluid is given by the following equation [Landau and Lifshitz, 1959; Pierce, 1989]:

$$\alpha = \frac{\omega^2}{2\rho c^3} \left[\left(\frac{4}{3}\mu + \mu_b \right) + \frac{\kappa}{c_p}(\gamma - 1) \right] \quad (3.4)$$

where $\omega = 2\pi f$ is the angular frequency of the acoustic wave, ρ is the volumetric mass density of the fluid, c is the speed of sound in the fluid, μ is the dynamic viscosity of the fluid, μ_b is the volumic viscosity of the fluid, κ is the thermal conductivity of the fluid, c_p (resp. c_v) is the heat capacity at constant pressure (resp. volume), and $\gamma = \frac{c_p}{c_v}$. This equation holds provided that the angular frequency is low enough so that the attenuation over an acoustic wavelength is small. This criteria is always met in practice in conventional photoacoustic imaging. For water, the various parameters involved in equation 3.4 have the following values at 20 °C [Xu et al., 2003; Holmes et al., 2011; NIST]:

- $\rho = 998.21 \text{ kg m}^{-3}$

- $\mu = 1.0016 \times 10^{-3} \text{ kg m}^{-1} \text{ s}^{-1}$
- $\mu_b \approx 3\mu$
- $\kappa = 0.59846 \text{ W m}^{-1} \text{ K}^{-1}$
- $c_p = 4184.1 \text{ J kg}^{-1} \text{ K}^{-1}$
- $\gamma = 1.0066$

μ_b is the bulk viscosity, also called the second viscosity. Its numerical value is not easy to determine, and thus the value given is only approximate. One of the way to measure this coefficient is in fact to deduce its value from equation 3.4 and a measure of sound attenuation at given frequencies. Other measuring techniques provide very similar numerical values. To evaluate the acoustic attenuation of water one can apply equation 3.4 with the tabulated values for its parameters, or directly use the tabulated values of acoustic attenuation in water. At 20 °C, acoustic attenuation in water is about $2.17 \times 10^{-3} \text{ dB cm}^{-1} \text{ MHz}^{-2}$ [Grigoriev and Meilikhov, 1997; Szabo, 2004].

The use of equation 3.4 enables one to compare the relative contribution of both the thermal conductivity and the viscosity to the acoustic attenuation in water. The ratio of the contribution from thermal conductivity to that of viscosity can be expressed as:

$$r = \frac{\alpha_{thermal}}{\alpha_{viscosity}} = (\gamma - 1) \frac{\kappa}{c_p} \cdot \left(\frac{4}{3}\mu + \mu_b \right)^{-1} \quad (3.5)$$

The numerical evaluation of r for water at 20 °C shows that at this typical temperature the contribution of the thermal conduction is negligible and that the acoustic attenuation is almost entirely due to viscosity: $r \approx 10^{-4} \ll 1$. The reason for such a low value of r is the fact that γ is very close to 1 in liquid water, thus $\gamma - 1 \approx 10^{-2} \ll 1$.

Equation 3.4 shows that the acoustic attenuation in water varies as the square of the acoustic wave frequency. Although it was out of our scope here to demonstrate this equation, it is interesting to understand where this frequency dependence comes from. The acoustic energy dissipated per volume and time unit is dictated by the square of both the temperature and velocity gradients [Landau and Lifshitz, 1959; Pierce, 1989]. Those gradients in turn, because induced by the acoustic perturbation, are inversely proportional to the acoustic wavelength, so proportional to the acoustic frequency. This explains why the acoustic attenuation is thus dictated by the square of the acoustic frequency.

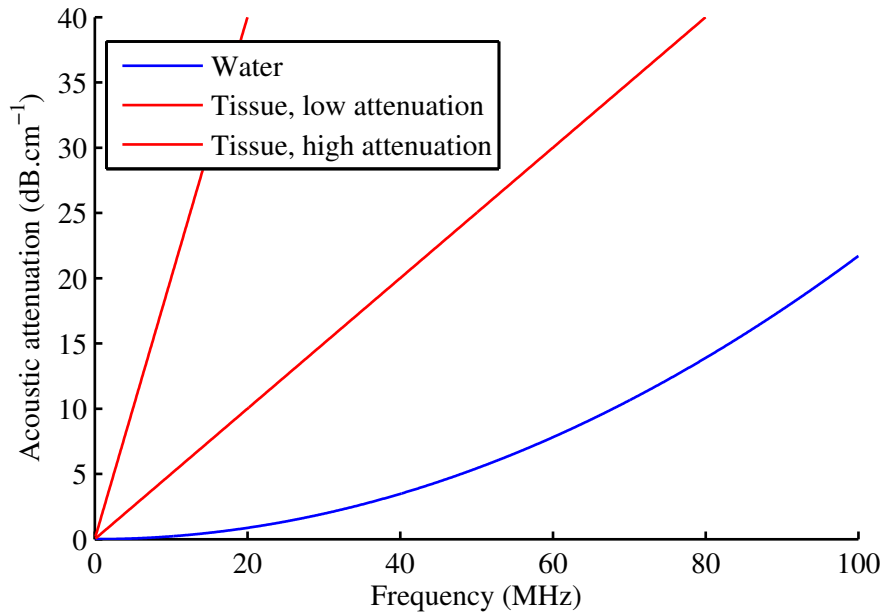


Figure 3.1 – Acoustic attenuation of water and tissues as a function of the acoustic waves frequencies. Low and high attenuation tissues respectively refer to tissues with acoustic attenuations of $0.5 \text{ dB cm}^{-1} \text{ MHz}^{-1}$ and $2 \text{ dB cm}^{-1} \text{ MHz}^{-1}$.

Comparison between water and biological tissue

To summarize the previous discussions on acoustic attenuation in water and tissue, we can write the following attenuation coefficients for tissue and water:

$$\begin{aligned} \alpha_{tissue} &\sim 0.5 - 2 \text{ dB cm}^{-1} \text{ MHz}^{-1}, \text{ at } 37^\circ\text{C} \\ \alpha_{water} &\sim 2 \times 10^{-3} \text{ dB cm}^{-1} \text{ MHz}^{-2}, \text{ at } 20^\circ\text{C} \end{aligned} \quad (3.6)$$

The dependencies above are illustrated on figure 3.1. The two important points to note from this figure are that, at 1 MHz, α_{water} is about 10^3 times lower than α_{tissue} , and that while α_{tissue} increases with f , α_{water} increases with f^2 . The acoustic attenuation in water is therefore much lower than in tissue for several tens of MHz frequencies. For acoustics frequencies of several hundreds of MHz, because of the square dependency, the acoustic attenuation in water is eventually higher than that in tissue. Based on the comparison above, the main idea of the work described in this chapter is to introduce the use of a water-filled acoustic waveguide to propagate high-frequency photoacoustic waves generated in optical-resolution photoacoustic micro-endoscopy in order to avoid acoustic attenuation

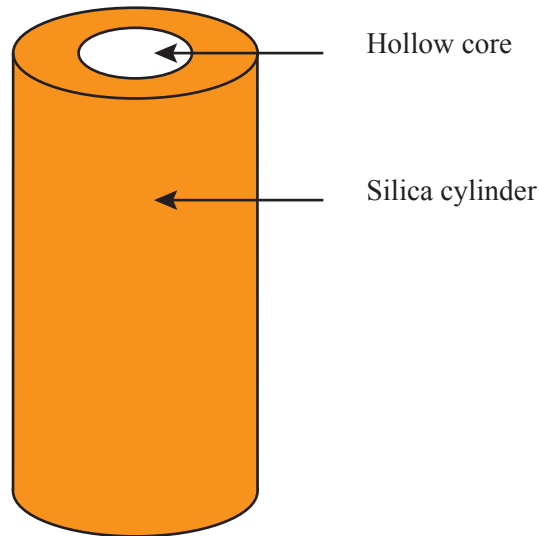


Figure 3.2 – General shape of a silica capillary.

in tissue.

3.1.2 A silica capillary as an acoustic guide

In this chapter silica capillaries are used. They are very thin hollow silica cylinders as illustrated on figure 3.2 which represents their general shape.

Why a silica capillary?

In the previous chapter, a step-index silica multimode fiber was used to focus and deliver at depth in tissue for photoacoustic endoscopy. Such a step-index fiber acts as a waveguide for light based on total internal reflection. While it was presented in more details in the previous chapter, let us remind its basic principle. A cylindrical core is surrounded by a lower refractive index cladding, so that provided that the optical field at the fiber input facet has an incidence angle θ_i smaller than $\theta_c = \sqrt{n_1^2 - n_2^2}$, the optical field propagates in the fiber core where it is trapped thanks to total internal reflection at the core/cladding boundary. The idea in this chapter is to use an optical waveguide to illuminate the fiber that would also act as acoustic waveguide to detect photoacoustic waves from outside the sample. In a fluid-filled silica capillary such as that illustrated on Fig 3.3, acoustic waves are expected to be guided, as the acoustic velocities in the silica "cladding" are higher than

that of in the inner water core (see following section for a detailed justification) [[Morse and Ingard, 1968](#)] (chapter 9, "Sound waves in ducts and rooms").

It follows from our previous discussion on acoustic attenuation, that the attenuation in such a water-filled acoustic waveguide is expected to be lower than the attenuation through tissue for the same propagation length. Moreover, water impedance is close to that of tissue so the coupling of the generated acoustic waves into the fiber core should not be affected by an impedance mismatch between the acoustic guide core and the imaged tissue. Finally, as will be justified in the discussion further, the silica capillary introduced above acts as a multimode optical waveguide in a way very similar to the conventional silica fiber used in the previous chapter.

Guiding of acoustic waves through a silica capillary

We discuss here in further details why a silica capillary can act as a waveguide for pressure wave in the water-filled core. Because the core/cladding boundary is a liquid/solid type boundary, with the liquid being water, and the solid being silica, the wave reflection and refraction at the boundary is not as simple as it would be in a fluid/fluid type boundary. Only longitudinal acoustic waves can propagate in a fluid, while both transverse and longitudinal waves can propagate in a solid. The speed values in glass depends strongly on the glass type, and thus will be given here for fused quartz which acoustic properties are very similar to the acoustic properties of the fused silica cladding medium used. The speed values for water and fused quartz/fused silica at 20 °C are [[Szabo, 2004](#); [NIST](#)]

- $c_{water} = 1482 \text{ m s}^{-1}$
- $c_{silicaL} \approx 5935 \text{ m s}^{-1}$
- $c_{silicaT} \approx 3740 \text{ m s}^{-1}$

An other important acoustic property of a medium is its acoustic impedance defined as the product of its volumetric mass density and the speed of sound in the medium. In silica the acoustic impedance can be described relative to both the speed of the longitudinal and transverse acoustic waves. The values in water and fused quartz/fused silica are given below at 20 °C [[NIST](#); [Momentum](#)]:

- $\rho_{water} \approx 998 \text{ kg m}^{-3}$,

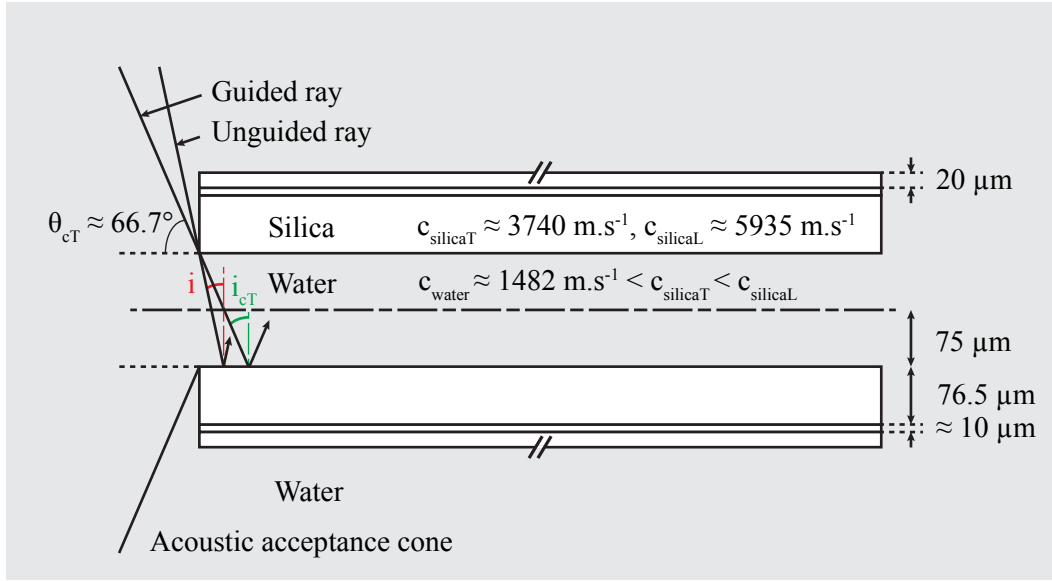


Figure 3.3 – Capillary seen from an acoustic waveguide point of view. c_{water} , $c_{silicaL}$ and $c_{silicaT}$ are respectively the speed of the longitudinal acoustic waves in water and the speed of the longitudinal and transverse acoustic waves in silica.

- $\rho_{silica} \approx 2200 \text{ kg m}^{-3}$
- $Z_{water} = \rho_{water}c_{water} \approx 1.480 \times 10^6 \text{ kg s}^{-1} \text{ m}^{-2}$
- $Z_{silicaL} = \rho_{silica}c_{silicaL} \approx 13.06 \times 10^6 \text{ kg s}^{-1} \text{ m}^{-2}$
- $Z_{silicaT} = \rho_{silica}c_{silicaT} \approx 8.228 \times 10^6 \text{ kg s}^{-1} \text{ m}^{-2}$

Reflection/refraction of a pressure wave at a fluid/solid interface. Let us describe what would happen to a incident plane monochromatic acoustic wave on a water/silica boundary for increasing incidence angle (represented in red on figure 3.3) from $i = 0^\circ$ to $i = 90^\circ$ [Royer and Dieulesaint, 2000]. The incident wave is propagating in water and therefore is always longitudinal and so is the reflected wave if there is any. At $i = 0^\circ$, part of the incident wave is reflected as a longitudinal wave in water and part of it is transmitted in the silica as a longitudinal wave as well. The amplitude of the reflected acoustic wave is dictated by the water acoustic impedance and the silica longitudinal acoustic impedance. The higher the contrast between these impedance the higher the amplitude reflection coefficient. At normal incidence the pressure amplitude reflection coefficient for a water/silica boundary is given by $r_p = \frac{Z_{silicaL} - Z_{water}}{Z_{silicaL} + Z_{water}} \approx 0.80$. As the incidence angle

increases i , the refracted acoustic waves in the solid are not longitudinal only anymore but also transverse. When the incidence angle i is greater than the first critical incidence angle value $i_{cL} = \arcsin(\frac{c_{water}}{c_{silicaL}}) \approx 14.5^\circ$, the longitudinal refracted waves in the silica becomes evanescent. The same phenomena appear at even higher incidence angles for which the transverse refracted waves also become evanescent if the incident angle is higher than the second critical angle (represented in green on figure 3.3 $i_{cT} = \arcsin(\frac{c_{water}}{c_{silicaT}}) \approx 23.3^\circ$). For incidence angle higher than i_{cT} the incident longitudinal waves in water are totally reflected.

Propagation of a pressure wave in a liquid-filled solid cylindrical tube. Let us consider a water-core, silica-cladding acoustic waveguide immersed in water and used to guide the acoustic waves generated by an acoustic source also immersed in water as well. Of course in a photoacoustic experiment context the acoustic source will be a photoacoustic source and it will be placed, as the acoustic guide, in either water or tissue. The generated acoustic waves will be coupled inside the acoustic guide and propagated through it until it opposite end where it will be detected by an acoustic sensor.

Just as in the case of optical fibers, the rigorous description of the wave propagation inside the water-core surrounded by the silica-cladding would require to solve the acoustic wave equations in each of these medium along with the appropriate boundary conditions. This is however difficult to do in practice because of the different waves that might propagate in both the water and the silica, as well as the quite small thickness of the silica cladding used compared to the wavelength of the acoustic waves transmitted. The coupling of the acoustic wave inside the guide depends on the acoustic modes of the guide and on the acoustic source emission and position. The propagation of the acoustic waves at the guide output until their detection by an acoustic sensor is dictated by the propagation of the excited acoustic mode inside the guide. In this chapter the chosen acoustic waveguides have inner diameters that are about twice the size of the detected acoustic waves wavelength in water, so that it may reasonably be considered that only low orders modes can be guided.

Although the geometrical ray acoustic approach is incomplete and only valid for acoustic waveguides that would support a great number of modes, it can provide some useful results. It follows from the previous discussion about a water/silica boundary, based on a similar explanation as the one done in the previous chapter for optical rays and optical fibers, that an acoustic wave propagating in water and incident on the acoustic waveguide will

be guided and trapped inside the water core of the acoustic waveguide only if its incident angle on the guide input facet is smaller than $\theta_c = \arcsin(\sqrt{1 - (\frac{c_{water}}{c_{silicaT}})^2}) \approx 66.7^\circ$. This critical angle can be used to fix an upper limit of the acoustic waveguide acceptance cone half angle.

The capillary tube that we used as an acoustic waveguide is depicted on figure 3.3. It is composed of a 150 μm inner diameter hollow core that is filled with water, surrounded by a 76.5 μm thick silica and doped silica cladding, and a 20 μm thick protective polyimide layer. The overall outer diameter of the acoustic guide is about 363 μm .

The color code that has been applied on figure 3.3 follow the color code that had been used in the previous chapter and that will be used in all this chapter for acoustic as well as optical waves guidance, so that regions of the waveguide in which the wave propagating speeds are lower are represented with darker colors. According to that color code, waves traveling from a dark to a bright region can undergo total internal reflection while waves traveling from a bright to a dark region will always be only partially reflected. Regions of the waveguide considered perfectly absorbing are represented in dark (see figure 3.15).

3.2 Proof of principle

The objective of this section is to demonstrate the ability of a water-filled capillary to transmit an OR-PAM image through several centimeters of a strong acoustic attenuation tissue. Here we are only interested by the acoustic guiding part of the OR-PAM imaging process, thus we allowed ourselves to directly scanned a focused spot on the sample placed at the opposite side of the tissue by use of a microscope objective. This is in fact the complementary experiment of what was performed in the previous chapter, where ultrasound was detected at the tip facing the sample, and light was focused from the other tip.

3.2.1 Materials and methods

Experimental setup

Figure 3.4 presents a schematic of the experimental setup for OR-PAM imaging through a capillary. The output of a Q-switched pulsed laser (wavelength 532 nm, pulse duration

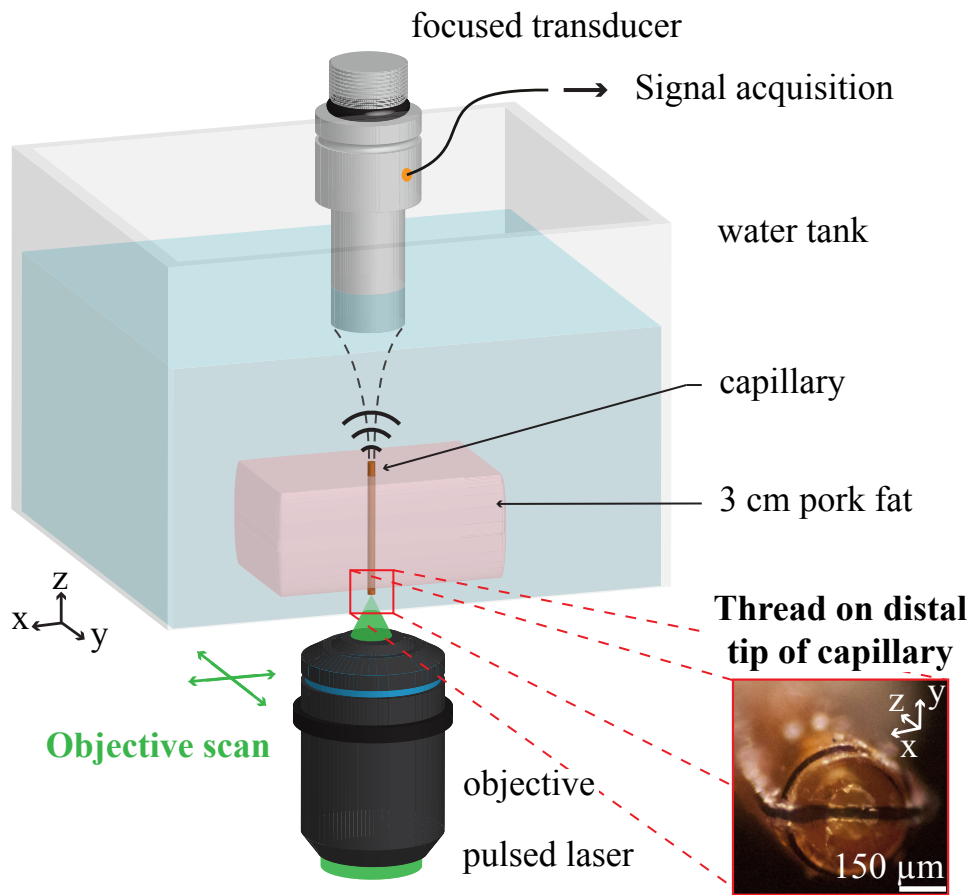


Figure 3.4 – Experimental setup for OR-PAM imaging through a capillary. An absorbing sample, 30 μm diameter black nylon thread, is shown in the inset.

4 ns, repetition rate 10 Hz, Brilliant, Quantel, France) was focused by a 40x, 0.6 NA microscope objective (LUCPLFLN, Olympus, Japan). The laser output energy was estimated at around 1 $\mu\text{J}/\text{pulse}$. The objective was mounted on a 3-axis motorized translation stage installed below the water tank to mechanically raster scan the optical focus on the absorbing sample.

A 30 mm long capillary (150 μm inner diameter, 86.5 μm silica thickness, Polymicro Technologies, USA) was filled with water to be used as an acoustic waveguide. The distal tip, which would be inside the sample in a tissue experiment and therefore corresponds to the acoustic waves entrance tip, was located at the bottom of the water tank where the optical spot was raster scanned around the absorbing sample.

The photoacoustic waves guided through the capillary water core (see figure 3.3) were detected with a high frequency spherically focused transducer (20 MHz, 12.7 mm focal distance, 6.3 mm diameter, PI20-2-R0.50, Olympus, Japan), with its focal spot located at the proximal tip (the tip that would be outside the sample in a tissue experiment). For each position of the focused optical spot, the photoacoustic signal was acquired by the transducer, amplified by a low noise amplifier (DPR500, remote pulser RP-L2, JSR Ultrasonics, USA) and digitized on an oscilloscope (DLM 2024, Yokogawa, Japan). The data were transferred to the computer used to control and synchronize the whole acquisition process. OR-PAM images were obtained by raster scanning of the optical focus spot and measuring the peak amplitude of the envelope of the acoustic signal detected at each scanning position. Pixel sizes are 5 μm and fields of view are 401 μm by 401 μm .

Two types of absorbing samples were used, depending on the objective of each series of experiment.

- The first type of absorbing sample consisted of a homogeneously absorbing 23 μm -thick polyester red layer (color film 60193, Réfectiv, France), fixed at the bottom of the water tank. This sample was used to compare photoacoustic *signals* with and without the capillary used as an acoustic waveguide. The optical spot was focused directly on the absorbing layer.
- The second type of absorbing sample was a 30 μm diameter black nylon thread (NYL02DS, Vetsuture, France), either held onto the bottom of the tank when no capillary was used (for the reference image, see below) or held directly on the distal tip of the capillary (see inset in figure 3.4) to prevent any motions during the imaging process. This sample was used to obtain photoacoustic *images*.

Series of experiments

Several series of photoacoustic experiments were carried out:

1. In a first series of experiments, photoacoustic signals generated by the homogeneous absorbing layer were used to compare the amplitude of photoacoustic waves through either water or a 10-mm thick layer of fat pork. The acoustic transducer was focused and aligned onto the absorbing layer at the location of the optical spot. In this configuration, the pork layer was easily inserted between the transducer and the

homogeneous absorbing layer without perturbation of the photoacoustic signal. The thickness of the pork layer was limited to 1 cm by the 12.7 mm focal length of the transducer. With this series of experiment, no capillary was used.

2. To obtain a reference photoacoustic image of the absorbing thread through water, a simple imaging experiment was carried out with the thread fixed at the bottom of the water tank, with the ultrasound transducer focused at the sample location (12 mm away from the bottom of the tank). Here again, no capillary was used.
3. To obtain an image of the absorbing thread through a 30-mm thick layer of pork fat (obtained from a butcher store), the thread was directly held by the distal tip of the 30-mm long capillary. The capillary was embedded into the pork layer before imaging. The high acoustic attenuation of pork fat, and the significant thickness of the layer, were used to illustrate a situation in which the detection of high frequency photoacoustic signals at depth in tissue is very difficult if not impossible. For imaging with photoacoustic wave guided through the capillary, the acoustic transducer was focused onto the proximal tip of the capillary, as represented on Fig. 3.4.

3.2.2 Results

Acoustic attenuation through the layer of fat

Based on the measurement from the first series of experiments, figure 3.5 shows that OR-PAM signals transmitted through through a 1 cm pork fat layer are about 100 times lower (-40 dB) than that measured through water. As a consequence, it is in practice impossible to detect OR-PAM signals directly through a 3 cm pork fat layer, for which a total attenuation of typically about 120 dB may be expected. Figure 3.5 also illustrates the low-pass filtering of high frequency photoacoustic waves through biological tissue: the central frequency of the signal is reduced from 17 MHz, close to the 20 MHz central frequency of the transducer, to only 5.5 MHz, well below its 14 MHz -6 dB cut-off frequency.

Photoacoustic images of the absorbing thread

Figure 3.6 summarizes the results from the two other series of experiments. Figure 3.6(a) shows the optical-resolution photoacoustic reference image of the absorbing thread ob-

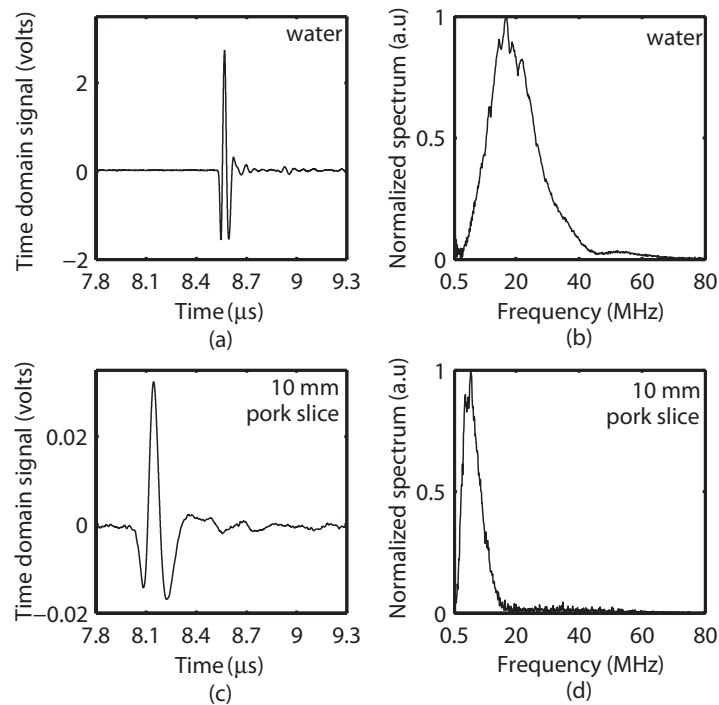


Figure 3.5 – Pork fat acoustic attenuation. (a) Time-domain acoustic signal captured in water, (b) normalized spectrum of the time-domain signals in (a), (c) time-domain acoustic signal acquired through a 1 cm thick pork fat layer, and (d) normalized spectrum of the time-domain signals in (c).

tained through water. Figure 3.6(b) shows the image of the same sample obtained after the photoacoustic waves have been guided inside the capillary through the 30-mm thick pork layer. For both images, signals were coherently averaged 16 times. As expected the resolution is the same on both images, and the field of view is reduced to a 150 μm diameter disc, corresponding to the diameter of the acoustic waveguide: looking at the OR-PAM image and the white light optical image in figure 3.6(c) we can see the photoacoustic wave's guidance by the water-filled core of the capillary as the effective field of view is limited to the solid circle corresponding to the capillary core. Probably because of the residual distance between the nylon thread and the entrance of the capillary core, low amplitude photoacoustic signals were also detected outside the field of view of the capillary core. The OR-PAM image closely resembles the white light optical image.

The upper signal shown on 3.6(d) corresponds to that measured when the optical spot is focused at the center of the thread on Fig.3.6(a). The lower signal corresponds to that measured when the optical spot is focused at the center of the thread on Fig.3.6(b). The

signals shown were coherently averaged 128 times in water and 1024 times through the capillary. The amplitude of the acoustic signals through the capillary is about 20 dB lower than through water, and the signals are detected about 19 μs later through the capillary than through water as the distance between the thread and the transducer is 30 mm greater. As illustrated by Fig. 3.6(e) plotting the frequency spectra of the temporal signals of figure 3.6(d), the acoustic coupling in and out of the capillary and acoustic propagation through the capillary act as a low-pass filter.

3.2.3 Conclusion

We have obtained an optical-resolution photoacoustic image after the photoacoustic waves have been guided in a capillary through 30 mm of fatty tissue. While these results are promising, several questions arose from this proof-of-principle experiment: in particular, a 20 dB loss was observed when the capillary was used, as compared to the free-space propagation in water. This loss can be caused either by insertion loss, or by propagation losses during the propagation through the fiber. The main objective of the following section is to further characterize the transmission efficiency of the capillary and to understand the origin of the losses.

3.3 Some properties of the capillary as an acoustic waveguide

The aim of this section is to characterize the transmission efficiency of the water-filled capillary as a function of the capillary length and the position of the photoacoustic source relative to the capillary input facet. One of our particular objective is to understand the origin of the transmission loss through the capillary.

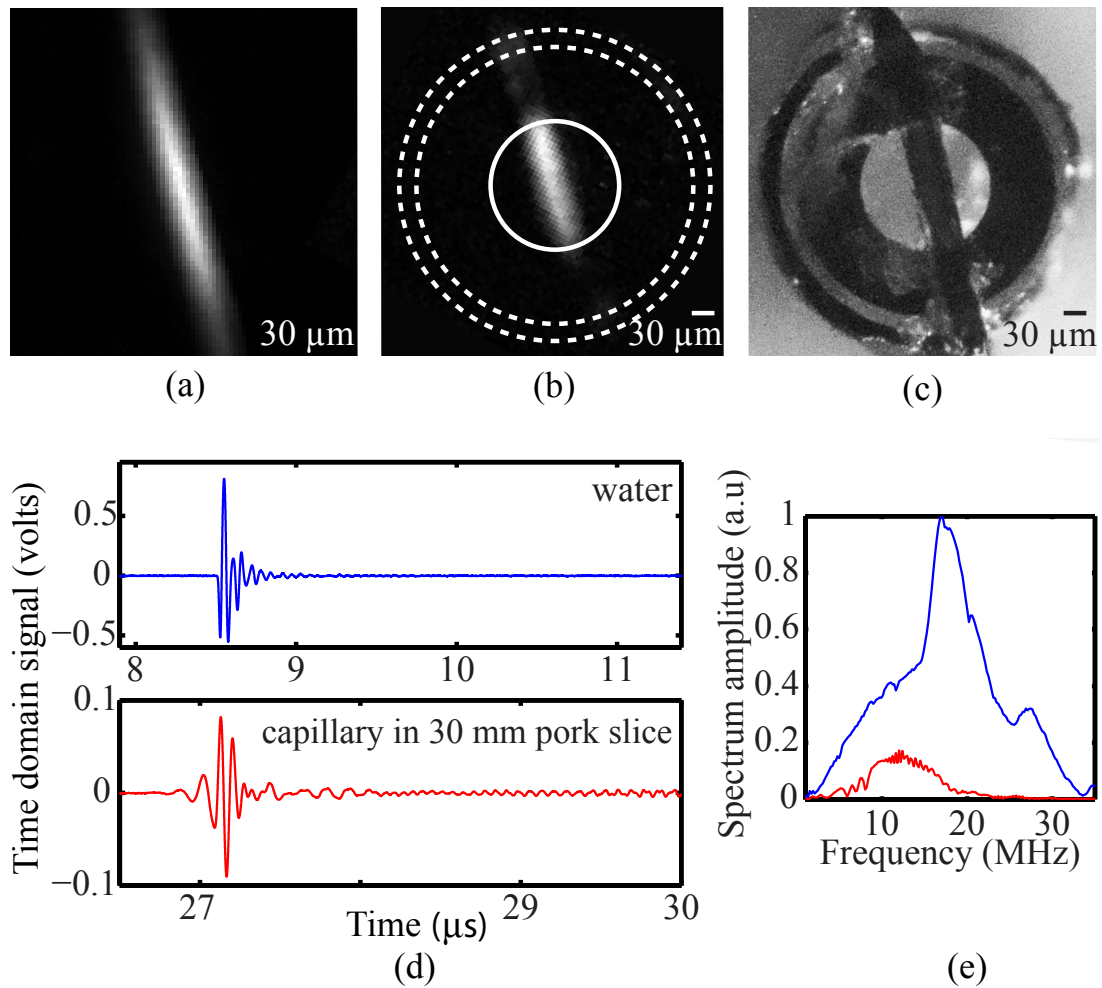


Figure 3.6 – Images and signals obtained with the setup presented in section 3.2.1. (a) OR-PAM image, (b) OR-PAM image through a capillary (the solid circle corresponds to the boundaries of the water-filled core, and the small and big dashed circles to the silica cladding, and the polyimide protective coating external boundaries, respectively), (c) white light optical image of the thread fixed at the distal tip of the capillary, (d) OR-PAM signals in the upper part, and OR-PAM signals through a capillary, in the lower part, and (e) frequency analysis of the signals shown in (d). The fields of view of images (a), (b) and (c) are the same.

3.3.1 Materials and methods

Experimental setup

To characterize the transmission through capillaries of various lengths, the setup used in the previous section was modified. As the propagation through the capillary is independent

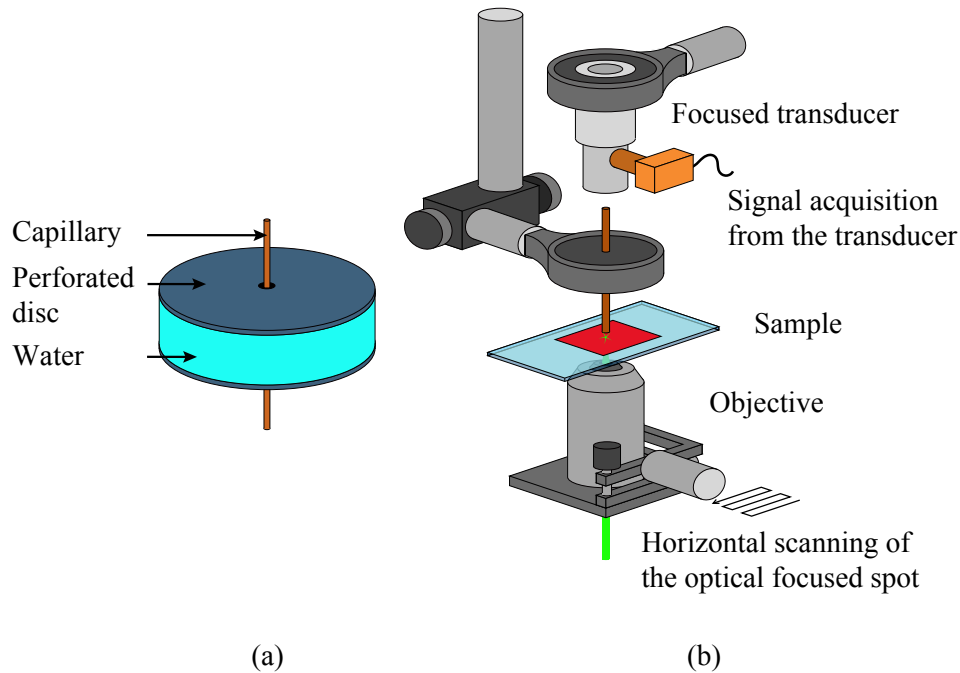


Figure 3.7 – Experimental setup for capillary acoustic guidance characterization. (a) Capillary holder, (b) PA signals detection through capillary.

of the surrounding medium, all experiments were carried out in water rather than through tissue for sake of ease. To accurately control the position of the capillary relative to the sample and the transducer, a capillary holder was used and mounted on a 3-axis manual translation stage. The transducer and the microscope objective were respectively mounted on a single vertical axis manual translation stage and a 3-axis motorized translation stage. The different mechanical components were assembled so that any of the three elements, capillary, transducer, microscope objective, could be moved relative to the other in all directions. The absorbing sample used in this section was the same homogeneously absorbing layer as the one used for the acoustic attenuation estimation of the pork fat layer in the previous section. For instruments availability reasons, we used a different transducer (35 MHz, 12.7 mm focal distance, 6.3 mm diameter, PI50-2-R0.50, Olympus, Japan), low-noise amplifier (5900PR, Olympus, Japan), and laser (wavelength 532 nm, pulse duration 0.6 ns, repetition rate 3 kHz, HLX-G-F001-110, Horus Laser, France) than in the previous section. The capillary holder and the setup used in this section are respectively depicted on figure 3.7(a) and 3.7(b).

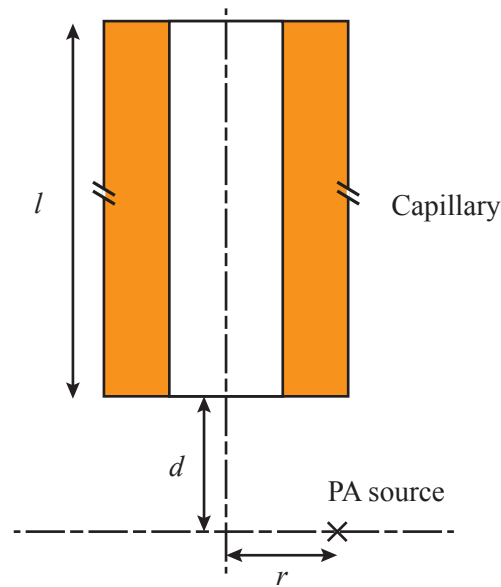


Figure 3.8 – Parameters of the experimental setup as a function of which the amplitude of the transmitted photoacoustic signal was studied, length l of the capillary and position (d, r) of the photoacoustic source relative to the capillary input facet.

Measurements

The amplitude of the detected photoacoustic signal was studied as a function of the length l of the capillary, the distance d along the capillary axis between the photoacoustic source and the capillary input facet, and the distance r of the photoacoustic source to the capillary axis. These parameters are represented on figure 3.8. During all the characterization measurements, the homogeneously absorbing sample was kept fixed at the bottom of the water tank (not represented in figure 3.7(b)). The fact that the sample was homogeneously absorbing had been verified in previous experiments and helped a lot for the characterization experiments presented here, especially for the study of the dependence with the radial distance r .

3.3.2 Results

In all the following results, the photoacoustic signal amplitude is taken as the peak amplitude of the signal envelope.

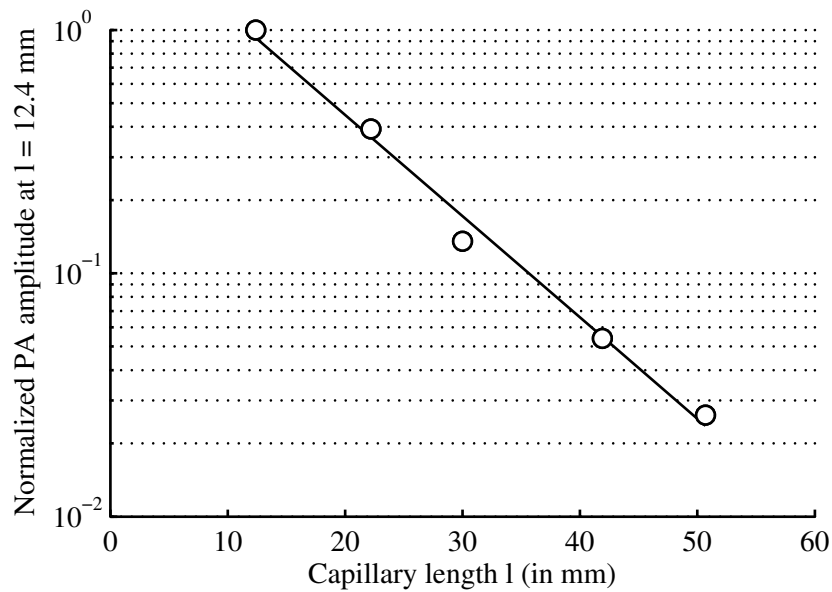


Figure 3.9 – Amplitude of the detected photoacoustic signals at the output of a capillary as a function of the capillary length.

Transmission as a function of capillary length

Figure 3.9 represents the amplitude of the transmitted photoacoustic signals as a function of the capillary length. The amplitude is plotted on a semi logarithmic scale for capillary lengths of about 10, 20, 30, 40 and 50 mm. The detected amplitude is found to drop exponentially with the capillary length: the fitting of the data by an exponential function, represented by a solid line in figure 3.9 indicates that the detected photoacoustic amplitude decays approximately with the capillary length according to the following equation:

$$\text{Amplitude}(l) = \text{Amplitude}(l_0) \cdot e^{-\alpha(l-l_0)} \quad (3.7)$$

where $l_0 = 12.4$ mm and $\alpha = 0.096$ mm⁻¹. The 95 % confidence bounds of the α value given by the data fitting are 0.080 and 0.110 mm⁻¹. This value corresponds to an attenuation of about 8.3 dB cm⁻¹. This is much higher than the expected attenuation for an acoustic waves propagating in water for frequencies such as those measured on the spectrum of the photoacoustic signal at the output of the $l = 12.4$ mm capillary. The average frequency on the spectrum was indeed measured to be about 25 MHz, and the acoustic attenuation in water at this frequency is about 1.4 dB cm⁻¹. Therefore, the observed attenuation does not seem to be dictated by the acoustic attenuation of plane pressure waves as initially

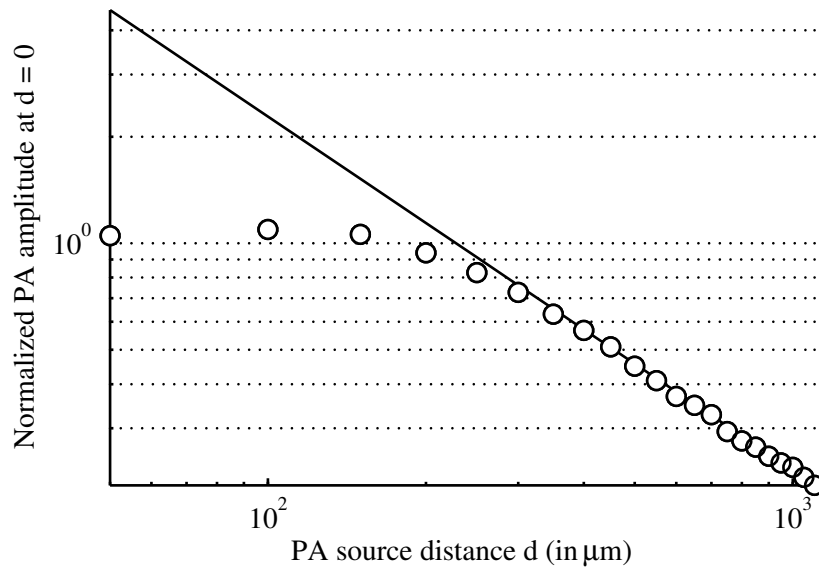


Figure 3.10 – Amplitude of the detected photoacoustic signals at the output of a 30 mm capillary as a function of the photoacoustic source distance on the capillary axis.

expected. This result will be discussed further below in the discussion.

Transmission as a function of source-to-capillary distance

Figure 3.10 plots the amplitude of the photoacoustic signals as a function of the on-axis distance from the photoacoustic source d to the capillary input facet. The curve is represented in a logarithmic scale, for distance d ranging from 0 to 1000 μm . On the figure the function $\text{Amplitude}(d) = \text{Amplitude}(d_0) \cdot \frac{d_0}{d}$ is also represented, where $d_0 = 1000 \mu\text{m}$. As can be seen on figure 3.10, this law fits well the experimental data for photoacoustic source distances greater than about 300 μm .

For distances ranging from 0 to 200 μm the amplitude of the envelope detected photoacoustic signal seems to increase slightly before decreasing for distances d greater than 100 μm . Although this could be explained by an not yet understood coupling phenomenon of the photoacoustic wave inside the capillary, it is likely that the capillary slightly moved up and back down in the capillary holder and thus in the transducer focal region when brought too close and then away from the absorber. If this explanation is correct, distance $d = 0 \mu\text{m}$ should be taken at the distance $d = 100 \mu\text{m}$ on figure 3.10. When brought in contact to the absorber the relative position of the capillary output facet relative to the transducer is

controlled in pulse/echo mode to normally avoid such inaccuracies.

Aperture of the capillary

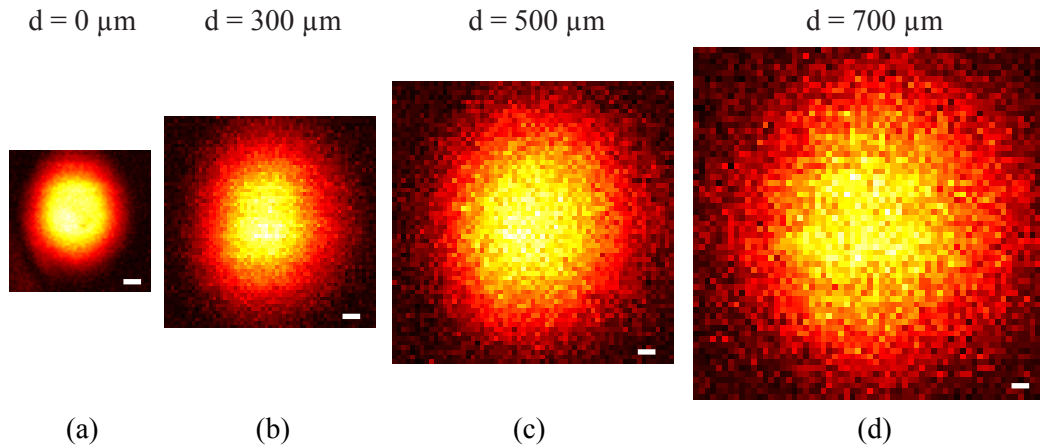


Figure 3.11 – Sensibility map of a 30 mm capillary in imaging planes orthogonal to its axis at distance (a) $d = 0 \mu\text{m}$, (b) $d = 50 \mu\text{m}$, (c) $d = 75 \mu\text{m}$, and (d) $d = 150 \mu\text{m}$. Scale bars represent $30 \mu\text{m}$.

Figure 3.11 shows maps of the photoacoustic signal amplitude in planes orthogonal to the capillary axis at distances $d = 0, 300, 500$ and $700 \mu\text{m}$ from the capillary input facet. It can be seen on this figure that as the imaging planes distance from the capillary input facet increases, the field of view increases. In fact, in good agreement with figure 3.10 it can also be seen that the amplitude of the detected photoacoustic signals decreases when the imaging plane distance d increases. The background color in these images all corresponds to the same noise level of the characterization setup.

The shape of the represented fields of view are almost circular and thus one can study the size of the field of view by measuring a radius. The radius of the field of view is defined here as half the full width at half maximum and could be measured at all plane distances without interference from the background noise level. The radius of field of view is represented as a function of the imaging plane distance d on figure 3.12. For a distance $d = 0 \mu\text{m}$ the field of view radius corresponds to the $75 \mu\text{m}$ radius of the water filled core of the capillary. For distances of $d = 300 \mu\text{m}$ and above the field of view radius is well fitted by a linear function with a slope of 0.36, when the field of view radius and the distance d are both expressed in the same length units (μm in figure 3.12). The 95% confidences

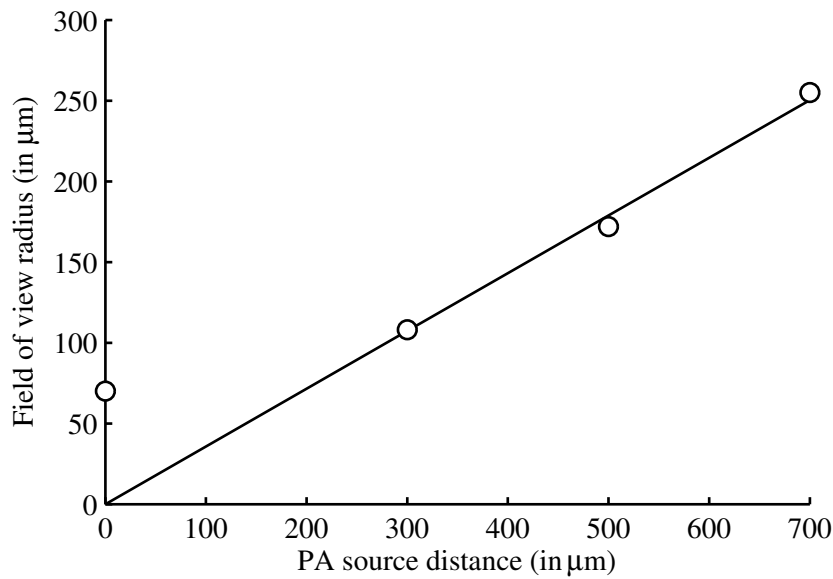


Figure 3.12 – -6 dB field of view radius as a function of the imaging plane distance for a 30 mm capillary.

bounds of the slope value given by the data fitting are 0.33 and 0.39. The 0.36 slope value corresponds to a half-angle angular field of view of $\theta = 19.7^\circ$. This angle value is however smaller than that of the acceptance cone half-angle predicted in section 3.1.2, $\theta_c \approx 66.7^\circ$. This will be further discussed later below.

3.3.3 Discussion

Propagation losses in the capillary

There are two main possible reasons to explain the high acoustic attenuation length measured in the capillary. First, some acoustic energy might not be properly confined in the capillary core, for instance if it leaks into the medium surrounding the capillary. Second, acoustic energy might be dissipated during its propagation in the capillary due to absorption phenomena beyond that of acoustic attenuation of plane pressure waves in water. In this discussion, we show that viscous losses from shear induced at the silica/water boundary, that were not considered so far, are significant and explain reasonably well the propagation losses in the capillary.

A simple model for viscous losses in a rigid tube. To do so, we consider a very simple model for the propagation of the photoacoustic waves inside the capillary. First, we will consider the silica cladding as being perfectly rigid so that the capillary is modeled as a perfectly rigid tube filled with water (no motion of the silica interface). The inner diameter of the tube is that of the capillary water-filled core, that is 150 μm . In such a tube, several acoustic modes may propagate. Here we will consider that only the first order mode, similar to a piston mode, will propagate. Under such condition, if water was considered as a lossless fluid, the acoustic waves would propagate inside the capillary without any attenuation as a plane wave. However, if viscosity and thermal conductivity of water are taken into account, the energy of the guided waves will be dissipated as they propagates inside the simplified capillary [Landau and Lifshitz, 1959; Pierce, 1989]. The acoustic attenuation coefficient is given by:

$$\alpha = \alpha_{fluid} + \alpha_{capillary} \quad (3.8)$$

where α_{fluid} is the acoustic attenuation coefficient of a plane wave propagating in the fluid and is given by equation 3.4:

$$\alpha_{fluid} = \frac{\omega^2}{2\rho c^3} \left[\left(\frac{4}{3}\mu + \mu_b \right) + \frac{\kappa}{c_p}(\gamma - 1) \right] \quad (3.9)$$

and $\alpha_{capillary}$ is an additional attenuation coefficient due to the capillary boundaries [Landau and Lifshitz, 1959; Pierce, 1989] (respectively chapter 77, "Absorption of sound", and chapter 10.5, "Attenuation and dispersion in ducts and thin tubes"):

$$\alpha_{capillary} = \frac{\sqrt{\omega}}{\sqrt{2}\rho c a} \left[\sqrt{\mu} + \sqrt{\frac{\kappa}{c_p}}(\gamma - 1) \right] \quad (3.10)$$

It is out of our scope to demonstrate those formulas however we will discuss the conditions under which they are valid as well as they physical origin.

As discussed in section 3.1.2, to find the guided modes inside a perfectly rigid acoustic guide, one has to solve the wave equation inside the fluid with the appropriate boundary conditions. If the fluid is considered ideal, the appropriate boundary conditions are that the tangential component of the velocity is equal to zero at the boundary. If however the fluid is considered viscous and conductive then the appropriate boundary conditions are that both

the tangential and normal component of the velocity are equal to zero at the boundary and that the temperature is equal to zero at the boundary. Here the term velocity and temperature refer to the fluid velocity and temperature associated with the propagation of the acoustic waves, in a homogeneous and quiescent fluid. The temperature boundary condition given here is in fact only an approximation but this will be of little importance as will be seen later.

Because of those two conditions, in a viscous and conductive fluid, the uniform piston-like acoustic mode that usually propagates in an ideal fluid is modified. It stays uniform over the majority of the tube section except close to the boundary where the velocity and the temperature have to drop to zero: the velocity and temperature exponential decays take place over layers close to the boundaries which thicknesses are given by:

$$\begin{aligned}\delta_v &= \sqrt{\frac{2\mu}{\omega\rho}} \\ \delta_T &= \sqrt{\frac{2\kappa}{\omega\rho c_p}}\end{aligned}\tag{3.11}$$

where δ_v and δ_T are the thicknesses of the viscous and thermal boundary layers.

Even if these thicknesses are small compared to the tube radius, they nevertheless turn out to induce a significant strong acoustic attenuation (as opposed to what we initially intuited when the capillary was introduced to guide acoustic waves). The reason is that as the boundary layers get smaller the velocity and temperature gradients get stronger, and thus the acoustic energy dissipation per unit volume get stronger. The total volume over which these gradients are strong due to the presence of the capillary varies as the boundary layer thicknesses, thus as $\sqrt{\omega}^{-1}$, but the gradients varies as the inverse of these thicknesses, thus as $\sqrt{\omega}$. Because the acoustic energy dissipated per unit time per unit volume is proportional to the square of the gradients, the total dissipated power integrated over the boundary layers volume, varies in the end as $\sqrt{\omega}$. The origin of the acoustic energy dissipation close to the boundaries is the same as in free space, the viscosity and thermal gradients, but the above discussion explains why the acoustic attenuation due to the capillary boundaries scales as $\sqrt{\omega}$ and not as ω^2 as in free space.

The expression given in equations 3.8, 3.9, and 3.10 for the acoustic attenuation is only valid for the first order mode propagating in a perfectly rigid guide under some specific conditions. These conditions are:

- $\delta_v \ll a$
- $\delta_t \ll a$
- $\delta_v \ll \lambda$
- $\delta_t \ll \lambda$
- $\alpha_{fluid} \ll \frac{\omega}{c}$
- $\alpha_{capillary} \ll \frac{\omega}{c}$

In our case, considering a capillary with an inner radius $a = 75 \mu\text{m}$, these conditions are very easily satisfied for any acoustic frequencies in the MHz to several tens of MHz range.

As mentioned earlier, for the simple temperature nullity boundary condition to be valid, there is another condition that has to be satisfied. This condition is roughly that the capillary material heat conductivity is much bigger than that of water. In our case this condition does not accurately hold as the heat conductivity of fused silica is only about twice that of water: $\kappa_{silica} \approx 1.4 \text{ W m}^{-1} \text{ K}^{-1}$, $\kappa_{water} \approx 0.6 \text{ W m}^{-1} \text{ K}^{-1}$ [NIST; Mometric]. However, in the case of a water-filled tube, the acoustic attenuation due to the capillary boundaries is mainly due to the viscosity of water and not to its thermal conductivity, so this is of very little importance.

Predictions from the simple model above. Let us work out some numerical computations to see whether the theory introduced above can explain the high acoustic attenuation measured in figure 3.9, with an attenuation coefficient of about 0.096 mm^{-1} .

To apply equation 3.8 to this experiment we can determine some center frequency for the measured photoacoustic signals. The spectrum of a signal at the output of the 10 mm capillary was analyzed and the average frequency was determined to be about 25 MHz. For such a frequency the attenuation predicted by our model is about 0.095 mm^{-1} which is very close to what was measured experimentally.

However, because the acoustic wave propagation in the capillary is dispersive, it is necessary to measure the acoustic attenuation coefficient at given frequencies. This is done in figure 3.13 where the acoustic attenuation coefficient is represented as a function of the acoustic waves frequencies, for frequencies ranging from 10 to 25 MHz. These values were obtained by fitting at each frequency the amplitudes of the spectra of the five signals used to plot

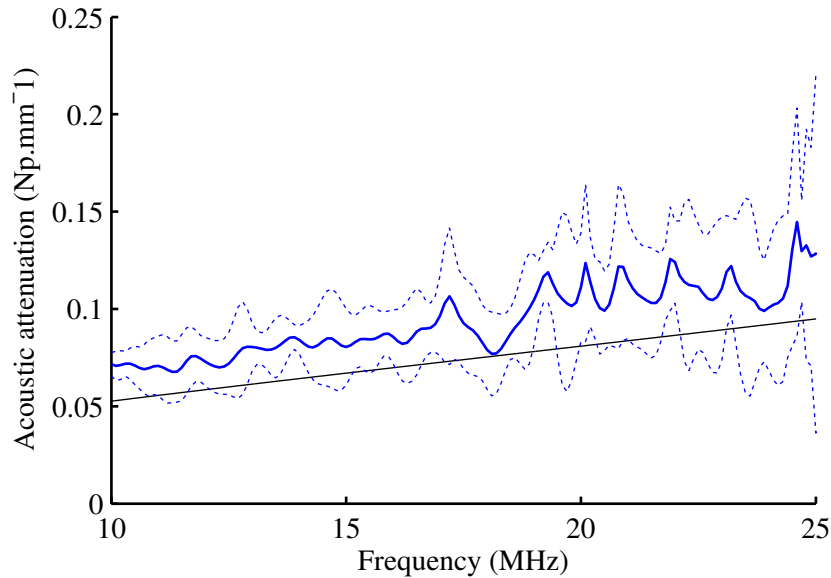


Figure 3.13 – Measured (solid blue curve), and predicted by equation 3.8 (solid black curve), acoustic attenuation coefficients as a function of the acoustic waves frequencies. The 95 % confidence intervals of the measured values are also represented (dashed blue curve).

figure 3.9. The 95 % confidence bounds values given by the fit are also represented along with the acoustic attenuation coefficient predicted by equation 3.8. It can be seen that there is a good agreement between the measured and the predicted values both in terms of orders of magnitude and of frequency dependence, although the measured values are slightly higher than the predicted ones. It should be mentioned here that the reason for the 95 % confidence intervals to be larger at higher frequencies in figure 3.13 is that the signal-to-noise ratios at the output of the longest capillaries were too low at frequencies below 10 MHz and at high frequencies, thus reducing the quality of the fit and probably slightly underestimating the acoustic attenuation coefficient at the figure highest frequencies. The signal-to-noise ratios are also what limited our frequency range of study to no more than 10 to 25 MHz.

Let us consider the experiment done with the 30 mm capillary embedded in a pork fat layer and a 20 MHz transducer. The average frequency of the photoacoustic signals detected directly in water was about 20 MHz. At such frequency the model predicts that the amplitude of a photoacoustic signal guided through a 30 mm capillary will be attenuated by 21 dB which is very close to the 20 dB value measured experimentally. However, in this case the attenuation is measured relative to a photoacoustic signal detected without the

capillary: the good match between the simple piston-like model and the measured value suggests that insertion losses into the capillary may be considered negligible.

The simple model used is based on the approximation that the capillary silica layer is perfectly rigid and that only the first order mode is propagating. The first approximation is justified by the fact that the characteristic impedance of silica is about 10 times greater than that of water. The second approximation is justified by the fact that only a small number of modes are susceptible to propagate in the tube. The cut-off frequency of such a rigid tube is given by $f_c = 0.29 \frac{c}{a}$ which is close to 5.8 MHz in our case. Although this is lower than the frequency guided in the capillary, it is not that small compared to what would happen in a multimode fiber as studied in the previous chapter, so that only a few modes can propagate in the capillary.

The excellent match observed when the model was applied in a very approximate way on the time domain signals amplitudes does not reflect the fact that the model is perfectly appropriate, but rather that its predictions are compatible with the measurement, with possible compensations of effects that were not taken into account. A phenomenon that was not taken into account for instance is temporal dispersion in the case of multimode propagation. Dispersion due to different acoustic modes propagating in the capillary would imply different arrival times for different frequency components. It can be observed accordingly on figure 3.6(d) that the high frequency components arrive later than the low frequency components.

When the model was correctly applied on each frequency, the fact that it predicts acoustic attenuation coefficients slightly lower than the measured ones probably indicates that although acoustic attenuation seems to be predominantly due to shear viscous losses, there are also possible leaking of the guided wave through the silica walls.

A phenomenon that can be seen in figures 3.6(d) and (e) is that the average frequency of the photoacoustic signals detected at the output of the capillary is lower than that of the photoacoustic signals detected in water: about 14 MHz, against about 20 MHz. This can quite easily be explained by the fact the acoustic attenuation in the capillary increases significantly with the acoustic frequency as can be seen in equations 3.8, 3.9, and 3.10.

Some conclusion regarding the use of a capillary to guide high-frequency photoacoustic waves. Boundary viscous losses were initially not taken into account to draw

3.1 and compare the attenuation in water and tissue. As is now clear from the analysis above, viscous losses in boundary layers are crucial in estimating the acoustic propagation losses in the capillary. Figure 3.14 is a modified version of figure 3.1 that now includes the contribution of all viscous losses (under the assumption of single mode propagation though). Represented are the acoustic attenuations of water, tissues and capillaries of different radii as a function of the acoustic waves frequencies. The contributions of the acoustic attenuations due to the water/silica boundaries to the capillary overall acoustic attenuations are also represented. It can be seen that the acoustic attenuations in the capillaries are lower than in tissues only at sufficiently high frequencies, when the black curves are lower than the red curves. To estimate these frequencies the contributions of the acoustic attenuations due to the friction effects at the boundaries have therefore to be taken into account. At a given frequency, the thinner the capillary, the more significant the boundary effects. A wide capillary should be chosen to limit the acoustic attenuation, however at the expense of the acoustic waveguide bulk. A 100 μm to 150 μm radius capillary could be an interesting compromise. However, it is important to remember that as the capillary radius increase, the number of supported modes increases, making our model less accurate.

On the collection aperture

Before moving on to the next section that will detail our current works and perspectives, let us take a last look at the data presented in figures 3.11 and 3.12. Although it had been predicted in section 3.1.2 that the half-angle of the acceptance cone is about 66.7° the half-angle of the -6 dB field of view measured with a 30 mm long capillary and a 20 MHz transducer is about 19.7° as shown in figure 3.12. A simple explanation is that in that case the average frequency of the photoacoustic signals detected at the capillary output is about 16 MHz, which correspond to a wavelength in water of about 90 μm . Because this wavelength order of magnitude is the same as that of the water filled core the geometrical description given in section 3.1.2 is of course incorrect and only gives an upper limit to the field of view half-angle. If we apply the approximation that the capillary collection efficiency is the same as would be the emission efficiency of a baffled 75 μm radius piston for a 90 μm wavelength we find that the half-angle of the -6 dB field of view is about 23° which is quite close to the measured 19.7° . The above approximation is based on the assumption that the photoacoustic wave emitted in water is spherical which is justified by the small dimension of the photoacoustic source because of the tight light focusing. The

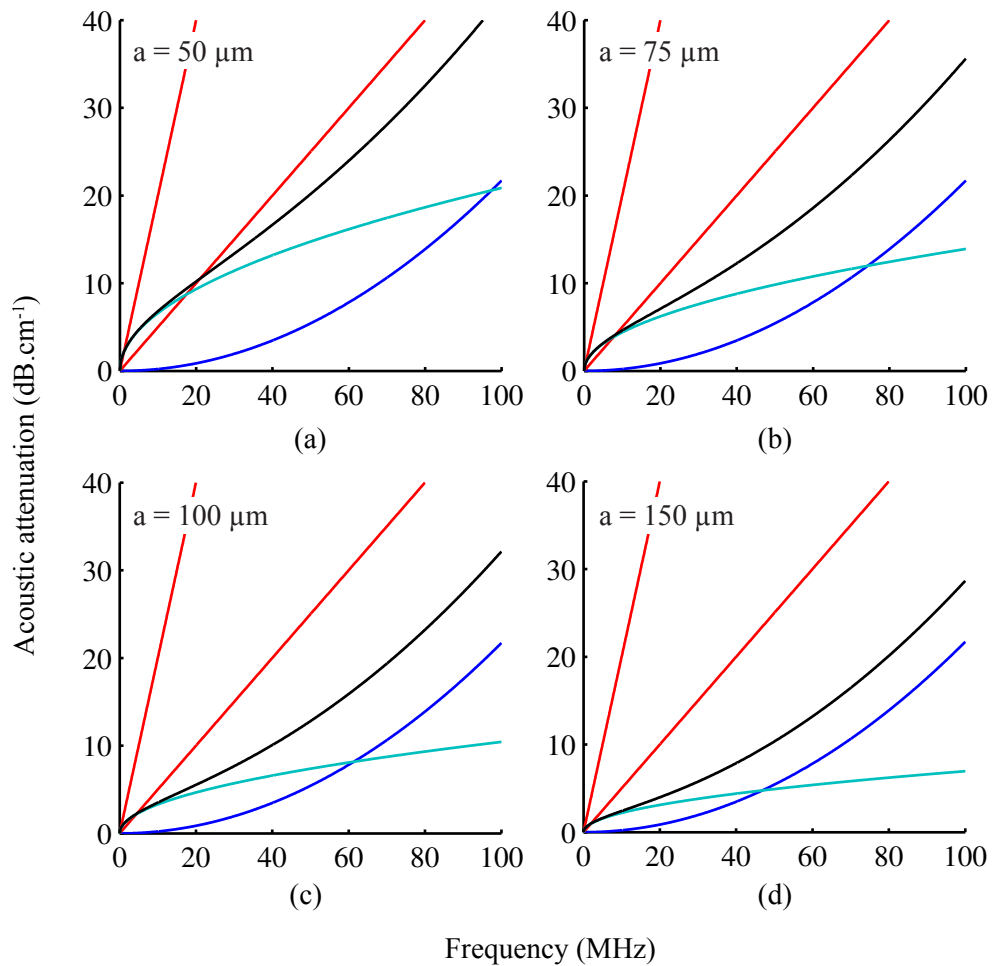


Figure 3.14 – Acoustic attenuations of water (dark blue curves) and low and high acoustic attenuation tissues ($0.5 \text{ dB cm}^{-1} \text{ MHz}^{-1}$ and $2 \text{ dB cm}^{-1} \text{ MHz}^{-1}$, red curves) as a function of the acoustic waves frequencies. The acoustic attenuations given by equations 3.10 (light blue curve) and 3.8 (black curves) are also represented for different values of the capillary inner radius a : (a) $50 \mu\text{m}$, (b) $75 \mu\text{m}$, (c) $100 \mu\text{m}$, and (d) $150 \mu\text{m}$.

computation of the field of view is only valid in the far field region from the capillary input facet/emitting baffled piston. This is the case for distances d of 300 μm and above as in such cases d is much greater than both $\frac{a^2}{\lambda} \approx 62 \mu\text{m}$ and $a = 75 \mu\text{m}$. This simple model is also able to predict the d^{-1} behavior of the amplitude of the enveloped detected photoacoustic signals at the capillary output that can be seen on figure 3.10 for distances d greater than about 150 to 250 μm depending on the d value chosen at the axis origin.

3.4 Current work and perspectives

The objective of this section is to demonstrate that the capillary can be used in *both* directions, i.e. as an optical waveguide into the tissue and as an acoustic waveguide in the opposite direction. We first explain why the capillary is in fact a multimode waveguide for optical fields, and then illustrate this dual guiding ability.

3.4.1 A silica capillary as an optical waveguide

The capillary that was described in the previous section and in figure 3.3 can be used as an acoustic guide but as an optical guide as well. As described previously it is composed of a water-filled hollow core surrounded by a silica layer, a doped silica layer, and a polyimide layer. From an acoustic point of view, the water-filled hollow core act as the core of the acoustic waveguide, and the two silica layers act as the cladding of the acoustic waveguide, with no difference being made between the two silica layers. The polyimide layer that is quite thin probably does not have any significant impact on the acoustic guiding abilities of the capillary. From an optical point of view things are a bit different. The refractive index of the silica layer is higher than that of water and than that of the doped silica layer, so that an optical wave can be confined within the silica layer based on total internal reflection. The numerical aperture specified by the capillary manufacturer is 0.22. The ability of the capillary to guide both the optical and the acoustic waves could be very useful. Indeed, provided the thin capillary is minimally invasively inserted inside a tissue, it could be used as an optical waveguide in one direction to illuminate the tissue at depth, and as an acoustic waveguide in the other direction for remote detection of the generated photoacoustic waves at the tissue surface, thus avoiding the strong acoustic attenuation in tissue at the OR-PAM acoustic frequencies. Because the silica layer thickness is very big compared to the

wavelength of the optical waves usually used in photoacoustic, the capillary will act as a multimode optical waveguide. Light distribution at its output will depend on the light injection, and the illuminated medium optical properties. If the illuminated medium is homogeneous thus not scattering, light delivery at the capillary optical output will only be possible within a cone whose top half-angle is dictated by the capillary numerical aperture and the medium refractive index. In water that angle value would be: $\theta_c = \arcsin(\frac{NA}{n_{water}}) \approx 9.5^\circ$. Because the capillary acts as a multimode waveguide, the digital phase conjugation method that was demonstrated in the previous chapter could be used to focus and scan light through the optically and acoustically guiding capillary for deep OR-PAM imaging in tissues.

The capillary used is very similar to a multimode step index optical fiber, however because it has a water-filled hollow core at its center, the propagation of optical waves in it is modified. A few questions that arise are: what portion of the input light is guided inside the silica layer, and can light be guided in the water-filled core as well? The answer to the first question is the same than would be for a conventional step-index optical fiber: only the light that is incident on the capillary input facet with an incidence angle lower than $\theta_c = \arcsin(\frac{NA}{n})$ can be guided in the silica layer, where NA is the capillary numerical aperture, and n the refractive index of the incident medium at the capillary input facet. The light rays that are incident on the capillary input facet with an angle larger than θ_c are partially reflected and partially transmitted at each silica/doped silica and silica/water interface thus not confined in the silica layer. The portion of the light that is transmitted either propagates in the doped silica cladding and is absorbed at the doped silica/polyimide boundary or propagates in the water and is absorbed later for reasons that will be explained just below, so that the light that is incident on the capillary input facet with an angle greater than θ_c rapidly vanishes. The answer to the second question is that no light can be guided inside the water filled core because any light that propagates inside would be partially transmitted at the water/silica boundary and then again at the doped silica/polyimide boundary where the transmitted light will be absorbed. The reason for this behavior is that not only are the refractive indexes of water and doped silica lower than that of silica, but the refractive index of water is lower than that of the doped silica. Provided that the capillary hollow core was filled in with a liquid that has a higher refraction index than either silica or doped silica, the capillary would act as a liquid-core fiber, but that is not the case here. There are two important remarks that we can make here from what has been said.

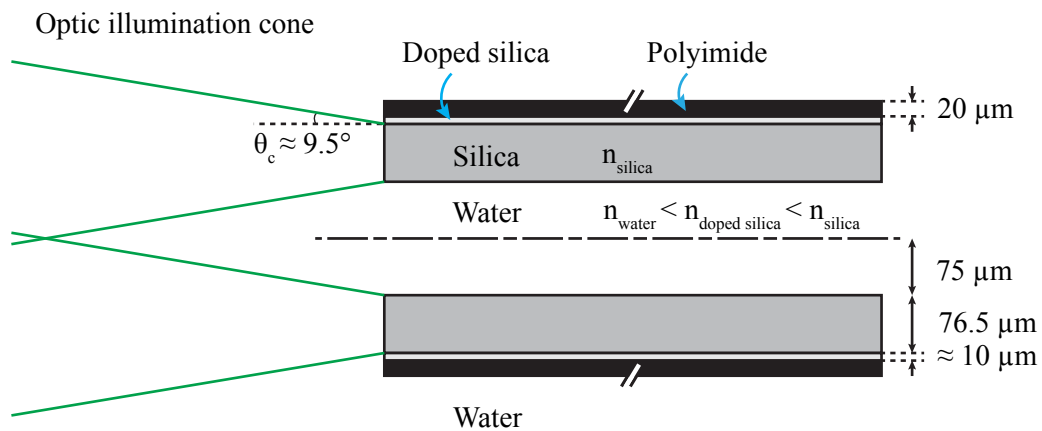


Figure 3.15 – Capillary seen from an optical waveguide point of view.

First, the polyimide protective layer plays an important role as far as light propagation is concerned. This is also true in the case of a conventional optical fiber where this protective layer, called the coating, not only protects the core and cladding of the fiber from physical damage but is also chosen so to be optically absorbing and to have a higher refractive index than the cladding to prevent light from being guided in the cladding. Second, the way the light will be coupled inside the capillary will be important as the light that will be sent on the silica layer with a too big incidence angle or on the water-filled core will be lost, meaning not guided and transmitted to the capillary output facet. With what has been said, one could wonder what is the advantage of using a capillary composed of a succession of silica, doped silica, and polyimide layers. The answer is the same as for an optical fiber. A simple silica capillary could be used to guide light, but using a cladded capillary enables to precisely control the numerical aperture of the capillary, and to make propagation inside the capillary insensitive to the outer medium in which it is inserted.

The capillary used is represented from an optical point of view in figure 3.15. Just as for figure 3.3, the scale was respected as it is quite important to get a realistic feeling of the elements size of the capillary, although it is not always immediate because of the small sizes involved.

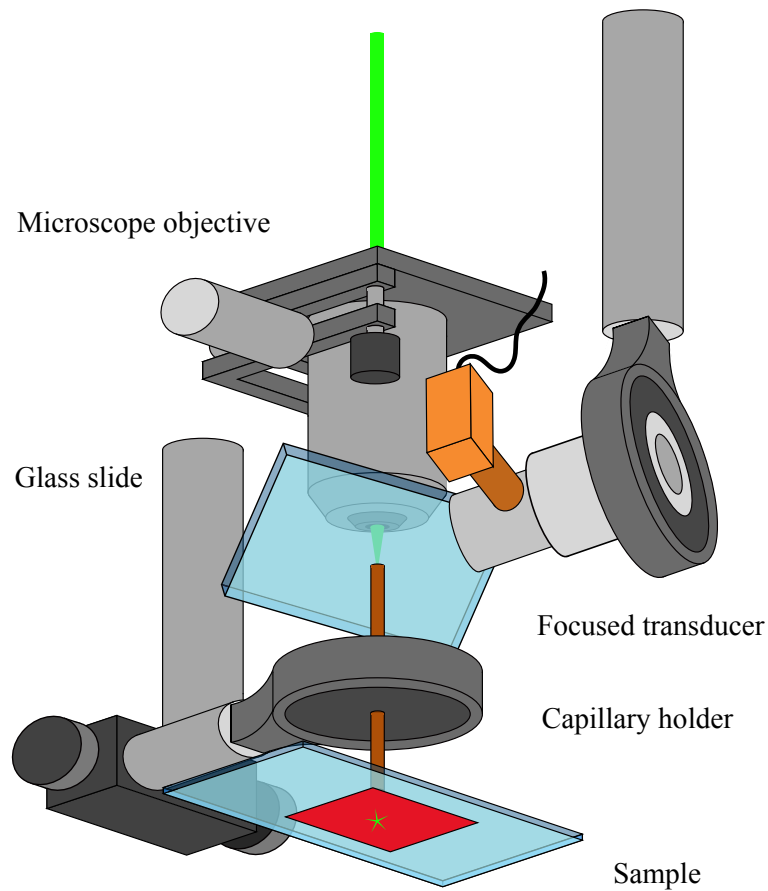


Figure 3.16 – Experimental setup for optical and acoustic guidance by a unique capillary.

3.4.2 Experimental Setup

In this section a setup was built, based on the setup presented in the previous section and in figure 3.7, to demonstrate the ability of a unique capillary to be used both for the photoacoustic excitation and detection. The setup used is very similar to that of figure 3.7 and is depicted on figure 3.16. The objective and the transducer were placed on the same side of the capillary and a 100 μm thick glass slide was used to deviate the photoacoustic waves emitted at the output of the capillary towards the transducer which was placed out of the capillary axis. The angle between the glass slide and the capillary axis was about 45°. In these preliminary experiments an $f' = 10$ cm converging lens was used instead of a microscope objective. Acoustic waves deviation by a 1 mm thick glass slide was also tested but no significant differences were observed compared to the 100 μm thick glass slide. The

100 μm thick glass slide was thus chosen as its footprint is smaller. No significant amplitude losses were measured on the photoacoustic detected signals due to the deviation by the glass slide. This was measured by using, or not using, the glass slide in pulse/echo mode on the capillary output facet and in photoacoustic mode by use of light delivery by an objective below the water tank as in the setup of figure 3.7.

3.4.3 Results

Two samples were imaged. To do so the sample holder was fixed to a one-axis translation stage orthogonal to the capillary, so that the absorber could be scanned in one direction withing the imaging plane of the capillary. In the setup configuration used in this section the imaging resolution is defined by both the illumination and the acoustic field of view in the capillary imaging plane and thus is about a few hundred μm .

Figures 3.17(a) and 3.17(b) presents profile of a 0.7 mm large non absorbing band created withing a large uniform absorber (color film 60193, Réfectiv, France) and of a 30 μm diameter black nylon thread (NYL02DS, Vetsuture, France). The distance between the capillary input facet and the sample holder are about 100 μm and 150 μm , and the scanning steps 50 μm and 10 μm , for figures 3.17(a) and 3.17(b) respectively.

We can see on figure 3.17(a) that the width of the non absorbing band is indeed about 0.7 mm and that the size of the collection area in the imaging plane, given by the size of the two edges slope is about 300 μm .

In figure 3.17(b) the 30 μm thread is too thin to be resolved however it is interesting to note that the size of the collection area in the imaging plane is also about 300 μm as in figure 3.17(a) and that the amplitude profile presents two maxima. The existence of these maxima confirms what had been said in section 3.4.1 that is that the optical waves are guided inside the silica layer. The fact that one maximum is higher than the other is likely due to the fact that more light was injected at one side of the capillary than at the other.

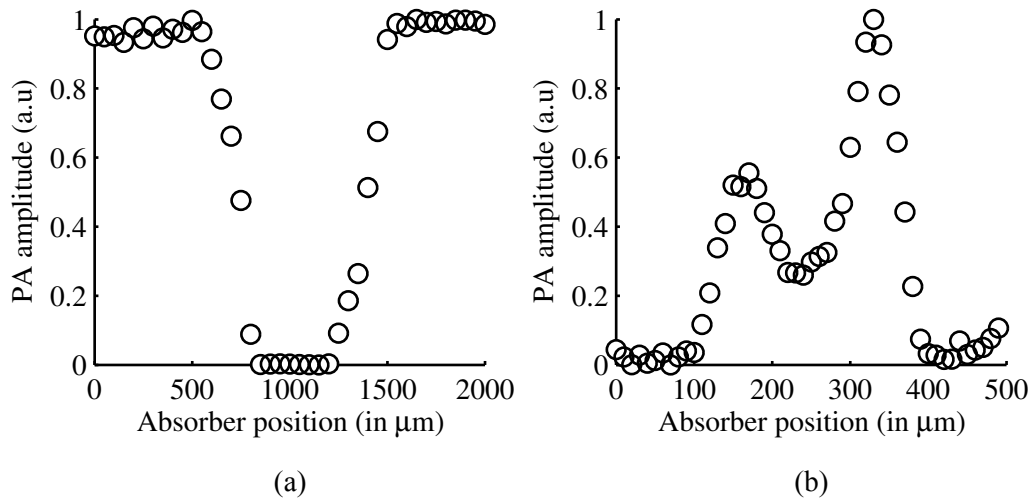


Figure 3.17 – Photoacoustic amplitude profile of (a) an about 0.7 mm non absorbing band in an homogeneously absorbing sample, and (b) a 30 μm diameter nylon thread using the setup depicted in section 3.4.2 with a 20 mm capillary.

3.5 Conclusion

In this chapter it was experimentally shown that water-filled silica capillaries could be used to transmit OR-PAM images through several centimeters of highly acoustically attenuating tissues. Images of a 30 μm nylon thread were acquired across a 3 cm thick pork fat layer. The photoacoustic waves detected at the output of the capillaries however suffered from an about 20 dB unexpected attenuation, significantly higher than the about 2 dB expected attenuation for a 3 cm plane wave propagation at the about 20 MHz acoustic frequencies detected. Further experiments were thus done to further characterize the acoustic guiding abilities of the capillaries. The amplitude of the transmitted photoacoustic waves were studied as a function of the capillaries lengths and the photoacoustic source position relative to the capillaries input faces. It was measured that the amplitude of the transmitted photoacoustic waves indeed decreased exponentially with the capillary length. For photoacoustic sources distances to the capillaries input faces greater than several hundred micrometers, the amplitude of the transmitted photoacoustic signals decayed inversely with the photoacoustic source distance to the capillaries input faces, for an acoustic source on the capillary axis. Under the same far field conditions, the -6 dB field of view of the capillaries increased proportionally with the imaging planes distances to their input faces.

A simple model was proposed for the propagation of the photoacoustic waves inside the capillaries, based on the assumptions that the capillaries walls were perfectly rigid and that most of the acoustic energy was guided in the first order acoustic mode. Taking into account the water viscosity, the model predicted attenuations that were in good agreement with the measured data, indicating that these previously unexpected acoustic attenuations are likely predominantly due to friction losses at the water/silica boundaries of the capillaries. This model also provided predictions concerning the fields of view that were in good agreements with the values measured experimentally. Moreover, it is compatible with the inversely proportional decay of the amplitude of the transmitted photoacoustic waves with the photoacoustic source distance to the capillaries input faces, for a photoacoustic source on the capillary axis. Interestingly, it also predicts that attenuation coefficient through the capillary tube should vary as the inverse of the capillaries radii and the square root of the fluid viscosity. Finally, it was shown at the end of this chapter that a unique capillary could be used both for photoacoustic excitation and detection.

There are several limitations to this work. First, although OR-PAM images could be transmitted through several centimeters of strongly acoustically absorbing tissue, the transmitted photoacoustic waves suffered from a quite strong acoustic attenuation. This could strongly limit the capillaries lengths that can be used and thus the imaging depths. Second, although the proposed model gave correct behaviors and orders of magnitudes for the measured data, it remains a very simple model that do not take into account a number of effects that might have a significant importance such as the acoustic wave coupling at the capillaries input, the higher orders acoustic modes of the capillaries, and the propagation towards the transducer at the capillaries outputs. Third, the ability of the capillaries to be used at the same time both photoacoustic excitation and detection was demonstrated without any wavefront shaping of the laser beam and thus could not provide OR-PAM images.

It seems that the acoustic attenuation due to the friction losses at the water/silica capillaries boundaries might be difficult to overcome. However, if our simple model is correct, they should significantly decrease as the capillaries inner radii are increased. Slightly wider capillaries could therefore be used to reduce the acoustic attenuation of the guided waves. It also seems that using warmer water, for example at 37 °C in *in vivo* experiments, would significantly reduce the acoustic attenuation of the capillaries through the water viscosity that strongly decreases as the temperature increases. The simple model could be refined

by taking into account some of the above mentioned neglected effects. Further experiments could also be done to gather more information concerning the capillaries guiding abilities and to test the models. For example, larger inner radius capillaries, larger numerical aperture transducers, and higher water temperatures could be used to further investigate the phenomenon at stake in the experiments presented in this chapter. Finally, and more importantly, building on the work that was presented in the previous chapter, the setup developed to demonstrate the ability of the capillaries to be used both for the photoacoustic excitation and detection should be coupled to a digital phase conjugation setup to demonstrate OR-PAM imaging ability through the capillaries in reflection mode. The shaping part of the experiment is being done by Nicolino Stasio at École Polytechnique Fédérale de Lausanne, and the complete experiment is in progress as an on-going collaboration with Nicolino Stasio.

Part II

Acoustic-resolution photoacoustic sensing

Chapter 4

Experimental setups for acoustic-resolution photoacoustic imaging

Contents

4.1	Raster-scanned focused transducer	91
4.1.1	Imaging system	91
4.1.2	Phantom images	93
4.2	Linear array probe and commercial ultrasound scanner . . .	94
4.2.1	Imaging system	94
4.2.2	In vivo imaging of mice tumors after injection of gold nanoparticles	96
4.3	Conclusion	100

In this chapter, some acoustic-resolution photoacoustic imaging setups are presented. These setups were initially developed for small animal imaging before the work done in the thesis took a different orientation as will be seen in the next chapter. The main objectives of this chapter is to present the setups that were developed and some of the results results that they allow to obtain, and to present in more details the setup that will be used in the following chapter (but only briefly described there). We first present an acoustic-resolution photoacoustic imaging setup based on raster-scanning of a single focused transducer and images of phantoms. A second acoustic-resolution photoacoustic imaging setup based on a linear array probe and a commercial ultrasound scanner is then presented, followed by experimental results obtained *in vivo* with gold nanoparticles injected on xenograft tumors.

4.1 Raster-scanned focused transducer

4.1.1 Imaging system

A conventional photoacoustic imaging system was built based on the raster scanning of a single high frequency focused transducer (8 mm focal distance, 4 mm diameter, 27.6 MHz central frequency, 95 % bandwidth, SNX110509 HFM13, Sonaxis, France). The sample to be imaged is immersed in a water tank and is illuminated by the output of a 4 ns pulse duration, 10 Hz repetition rate and 532 nm wavelength Q-switched laser (Brilliant, Quantel, France). The combination of a divergent lens, a convergent lens and an engineered diffuser is used to provide homogeneous circular illumination of about 3 cm diameter on the lower side of the sample. The photoacoustic waves are detected by the transducer at the other side of the sample in a transmission configuration. The transducer is raster scanned and at each position, the generated photoacoustic waves from the focal region are detected, converted into an electric signal, amplified by a low noise amplifier (5900PR, Olympus, Japan), displayed on an oscilloscope (DLM2024, Yokogawa, Japan), transferred and stored on a computer. The collection of all the acquired signals, each of which represents a depth profile (or A-line) which envelope is then computed and processed to provide either a

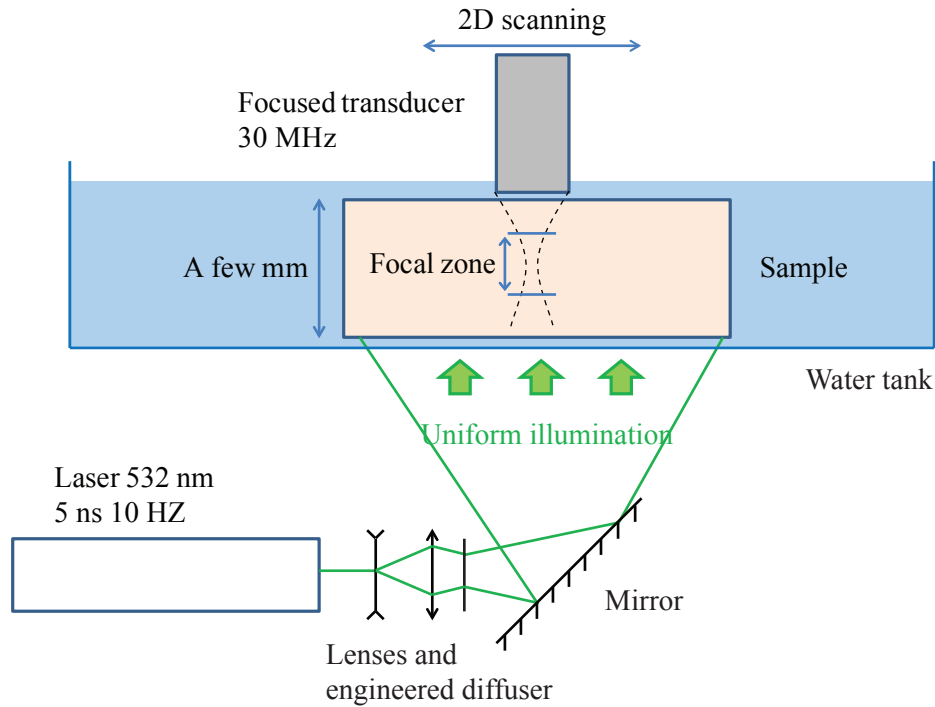


Figure 4.1 – Acoustic-resolution photoacoustic imaging setup based on a single element focused transducer.

two dimensional B-mode image, a three dimensional image or the maximum amplitude projection in a given direction of a three dimensional image.

The image acquisition speed could be limited by the speed of the motorized translation stage (M122.2DD, PI, Germany) that enables the lateral raster scanning of the transducer, the data transfer rate from the oscilloscope to the computer and the repetition rate of the laser. In practice, it was limited by the low repetition rate of the laser (10 Hz). Although the synchronization of the laser pulses and the oscilloscope acquisition is achieved by use of a delay generator (BNC575, Berkeley Nucleonics Corporation, USA) that trigger both devices, the data transfer and the step-by-step motion of the translation stage is controlled by a computer on Matlab. The lateral resolution of the images obtained is dictated by the frequencies of the detected signals and the transducer aperture, while their resolution is dictated by the bandwidth and the aperture of the transducer. The thickness on which the sample is imaged without introducing any axial scanning of the transducer is dictated by the frequencies of the detected signals and the aperture of the transducer (depth of field). Traditional ultrasound images can also be acquired by raster scanning of the transducer thanks to the emission/reception mode of the amplifier.

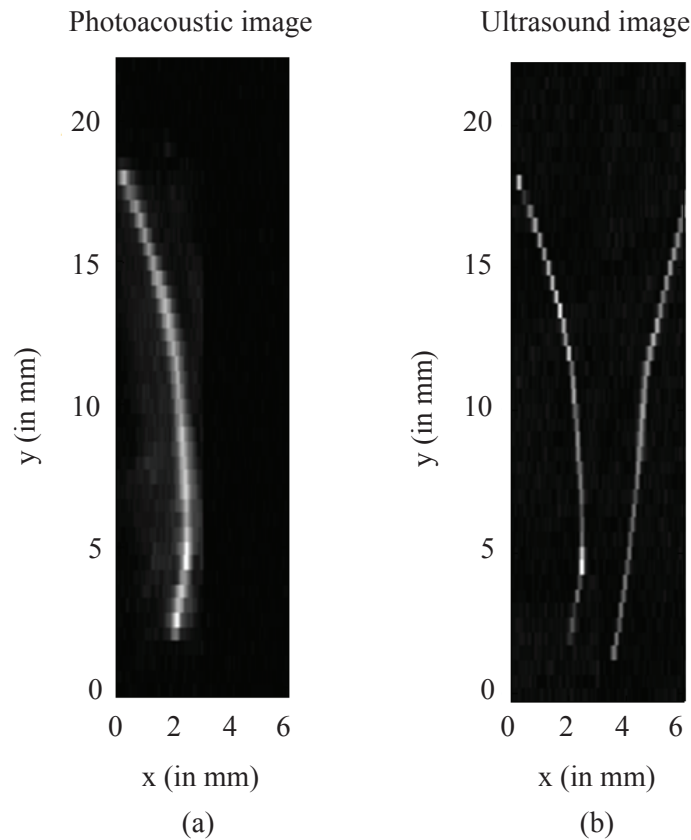


Figure 4.2 – Images of two polycarbonate tubes embedded at 0.5 cm depth inside a 1 cm thick $\mu'_s = 10 \text{ cm}^{-1}$ agar gel. The polycarbonate tube on the left is painted in black, the one on the right is transparent. No averages were performed. The fields of view are 61×45 pixels or 3×22 mm. (a) Photoacoustic image. (b) Ultrasound image.

4.1.2 Phantom images

Images acquired with phantoms designed to test the setup are presented in this section. The phantoms were made of a mixture of water, agar and Intralipid 10% (respectively about 89.5%, 1% and 9.5% of the mixture mass), with a reduced optical scattering coefficient $\mu'_s \sim 10 \text{ cm}^{-1}$, close to that of biological tissues. In a first phantom, two polycarbonate tubes with inner diameter of $24 \mu\text{m}$ diameter and outer diameter of $32 \mu\text{m}$ were embedded almost parallel to each other. The tubes are transparent and filled with air. One of them however is painted with black India ink. Therefore, as can be seen on figure 4.2, the two tubes will appear alike on the ultrasound image while only the one painted in black will clearly be seen on the photoacoustic image. This illustrates the different types of contrast

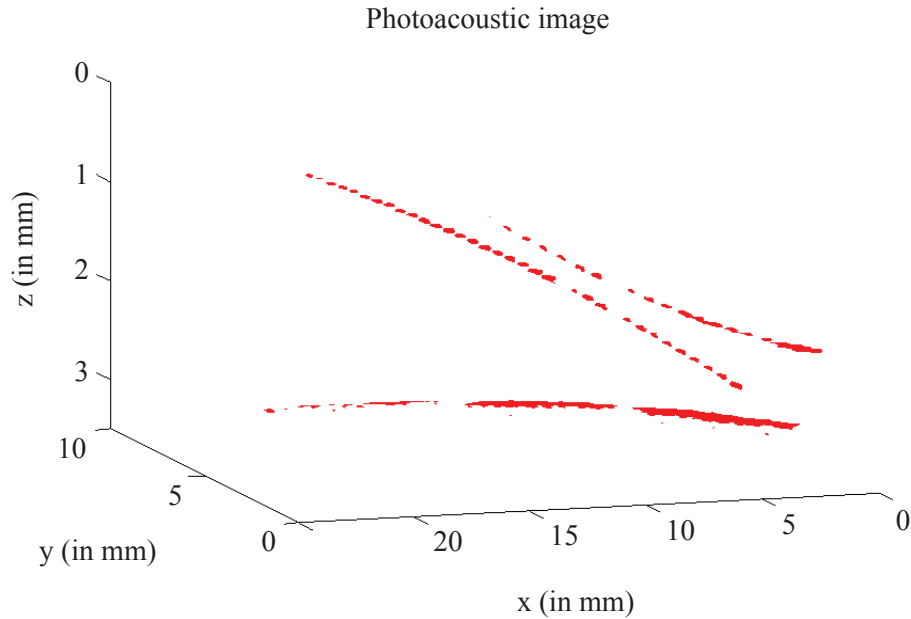


Figure 4.3 – Three dimensional photoacoustic image of three nylon threads embedded in a 1 cm thick $\mu'_s = 10 \text{ cm}^{-1}$ agar gel. The field of view is 96×45 pixels or 9.5×22 mm.

provided by photoacoustic and ultrasound images.

In a second phantom, three nylon threads $170 \mu\text{m}$ in diameter were embedded one above another at different depths and with different orientations, as can be seen on the three dimensional photoacoustic image presented in figure 4.3.

4.2 Linear array probe and commercial ultrasound scanner

4.2.1 Imaging system

A photoacoustic system was developed based on a linear array probe (20 mm focal distance, 7.5 MHz central frequency, 95 % bandwidth, SuperLinear SL15-4, SuperSonic Imagine, France) and a commercial ultrasound scanner (Aixplorer, SuperSonic Imagine, France). The software part of the system on the commercial ultrasound scanner was developed by Dr. Jérôme Gateau in our research group. The use of a linear array instead of a single

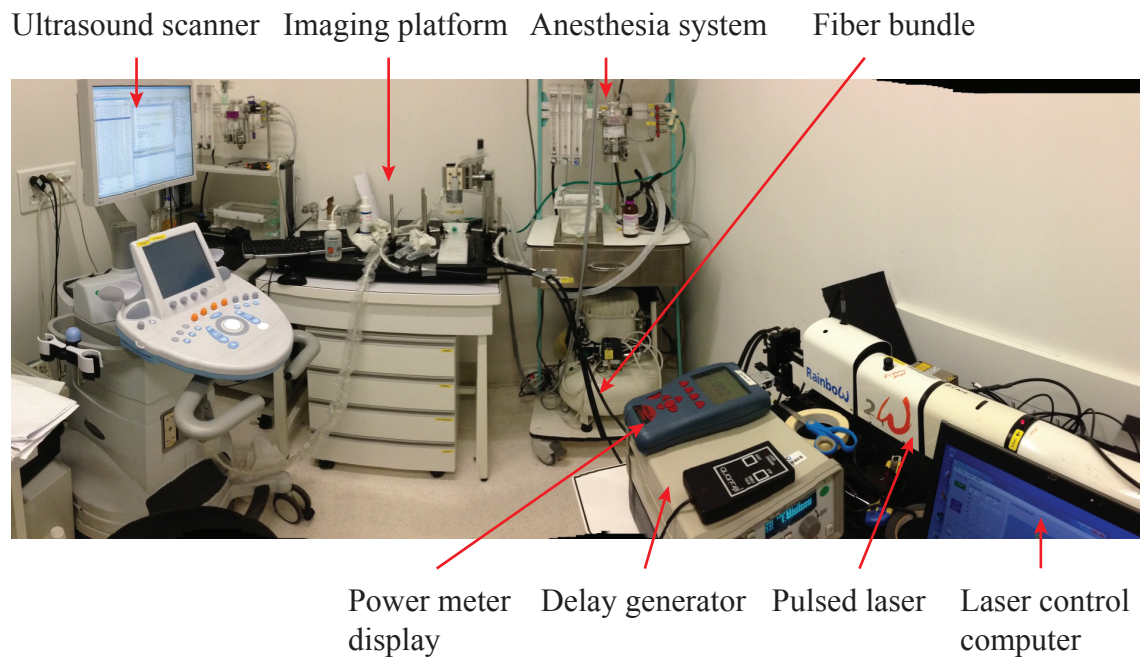


Figure 4.4 – Acoustic-resolution photoacoustic imaging setup based on a linear array probe and a commercial ultrasound scanner.

focused transducer enables the acquisition of images at a high frame rate, limited here by the repetition rate of the laser (10 Hz, Brilliant, Quantel, France). The wavelength of the laser output could be tuned in the 700 to 900 nm range thanks to an optical parametric oscillator (MagicPrism, Oportek, USA) controlled by a computer. A two arm fiber bundle (WF6-HPQ2-2.5-4.3, Ceramoptec, USA) was used to guide the output of the laser to an imaging platform dedicated to small animal imaging. An anesthesia system was available next to the imaging platform for *in vivo* studies. The optical power at the input of the 80% transmission fiber bundle was measured thanks to a thermal power meter. The laser pulses and the data acquisition on the ultrasound scanner were synchronized thanks to a delay generator that provided trigger signals for both of them. Traditional ultrasound images were acquired by the ultrasound scanner between the laser pulses and were displayed at the same time along with the photoacoustic images to provide additional information on the imaged sample.

4.2.2 In vivo imaging of mice tumors after injection of gold nanoparticles

Experimental protocol

The photoacoustic imaging system described in the previous section (4.2.1) was used to image tumors on living mice to which gold nanorods (15 nm diameter and 45 nm length, Nanospectra, USA) and gold nanoshells (150-180 nm diameter silica core, 15-30 nm thick gold coating, Nanospectra, USA) were injected. This was done with the help of Dr. Mariana Varna from our laboratory and approved by the local ethic comity. The objective was to understand how these gold nanoparticles are distributed in tumors in living mice. In particular, gold nanoparticles of different sizes were chosen to investigate the impact of this parameter on the gold nanoparticles distributions in tumors. It was for example believed that the gold nanorods would more deeply penetrate the tumor thanks to their smaller size.

Seven 4-to-6-week-old Swiss nude mice to which human kidney tumors had been xenotransplanted were studied. Four of them were injected in the tail vein with 100 μ L of an aqueous solution of gold nanorods with optical density about 2, while the other three were injected in the tail vein with 100 μ L of an aqueous solution of nanoshells with similar optical density about 2. Photoacoustic images of the tumors were acquired before the injection, during the injection and 5 minutes, 15 minutes, 30 minutes, 1 hour and 20 hours after the injection.

The practical implementation of the image acquisition is illustrated on figure 4.5. The mouse was anesthetized by an isoflurane and oxygen gaseous mixture and kept warm thanks to a water heating pad. The laser output wavelength was tuned to 800 nm as it was close to the plasmon resonance wavelength of the two types of gold nanoparticles used (about 780 nm for the gold nanorods and about 820 nm for the gold nanoshells). The tumors were illuminated from both sides by each arm of the fiber bundle by an optical energy of about 40 mJ per pulse on an area of about 2 cm², thus remaining within the maximum permissible exposure safety limits. An ultrasound coupling gel was used between the tumor and the ultrasound probe. The imaging plane of the probe array was first aligned with the tumor by use of the ultrasound imaging mode and a manual translation stage (Fig.4.5). The output of the fiber bundle were then adjusted in order to optimize the quality of the photoacoustic image that was displayed in real time on the ultrasound scanner display. Once everything

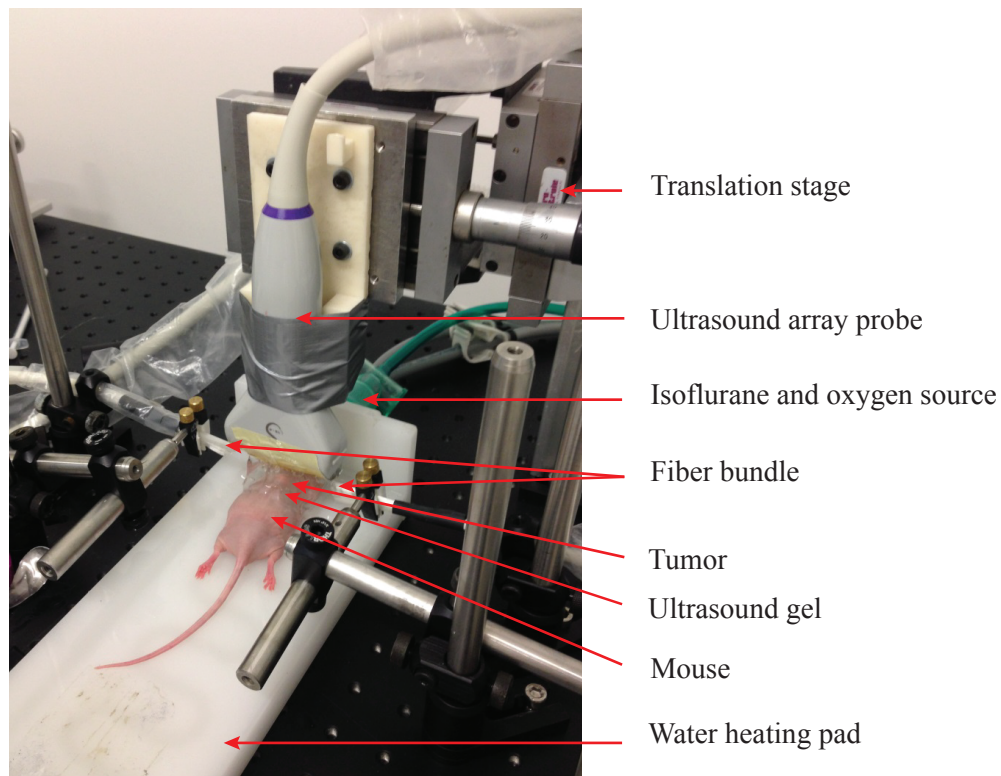


Figure 4.5 – Acoustic-resolution photoacoustic imaging setup used for tumor imaging on living mice.

was correctly aligned, at each image acquisition steps before and after gold nanoparticles injection, 400 images were acquired. The corresponding raw photoacoustic signals were then first filtered between 2 and 20 MHz by use of a third order Butterworth filter to improve the signals ratio and then processed using a classic delay and sum algorithm. To overcome the issue of motion caused by breathing, among the 400 acquired images, only the 30 most correlated were selected and averaged to form the final images such as these presented in figure 4.6 and 4.7.

Results

Among all the mice studied only the images corresponding to two of them are presented here, as typical illustrations of what was obtained with these experiments. Figure 4.6 presents the tumor images acquired on mice 1 before gold nanorods intravenous injection and 30 min and 20 h after. A photoacoustic image taken just after a direct injection of gold nanorods next to the tumor. The mouse was kept anesthetized until at least 30 min after

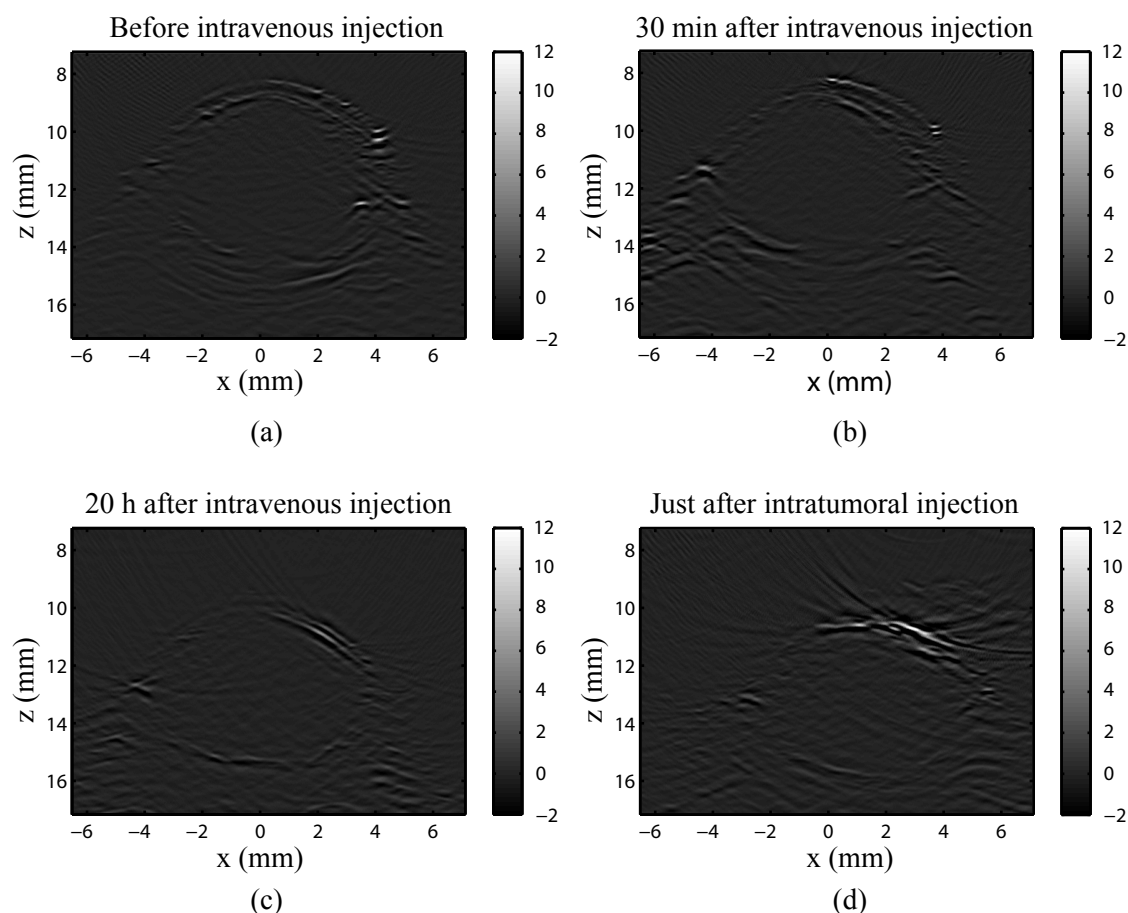


Figure 4.6 – Photoacoustic images of a tumor on a living mouse injected with gold nanorods. (a) before injection in the tail vein, (b) 30 min after injection in the tail vein, (c) 20 h after injection in the tail vein, and (d) just after direct injection next to the tumor. The color of the image represents the amplitude of the photoacoustic signals normalized by the average power of the laser output beam to take into account the laser fluctuations between the different acquisition times. The images are all represented with a common arbitrary unit and were saturated by fixing the lower and upper bounds of the color bar respectively to -2 and 12.

injection but had of course been awoken before the third presented image was acquired 20 h later. As can be seen on this figure, the mouse tumor can clearly be seen however no change were observed after gold nanorods had been injected in the tail vein. The same type of results were obtained on the five other mice. The main reason for this lack of results concerning the localization of gold nanoparticles inside the mice tumors is most likely due to the fact that, as was later shown during histology analysis, the tumors were

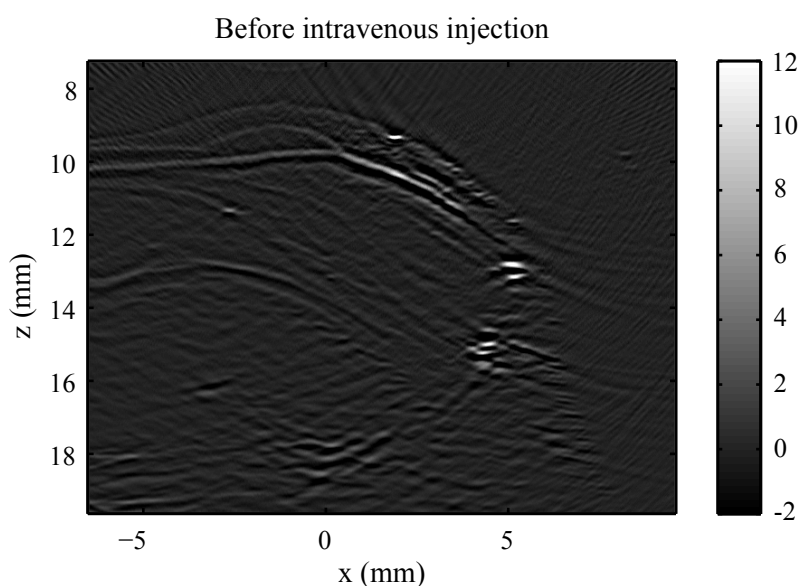


Figure 4.7 – Photoacoustic image of a tumor on a living mice before any gold nanoparticles injection. The tumor was partly viable and some blood vessels probably irrigating the tumor can be seen for example on its upper part. The color on the image represents the amplitude of the photoacoustic signals normalized by the average power of the laser output beam. The image is represented with the same arbitrary unit as in figure 4.6 and was saturated by fixing the lower and upper bounds of the color bar respectively to -2 and 12.

very necrotic. Gold nanorods were thus directly injected inside the tumor of mice 1 to make sure the imaging system would then have the ability to detect the injected gold nanorods, which was indeed the case as can be seen on figure 4.6(d) where a strong photoacoustic signal is observed in the upper right part of the tumor.

Figure 4.7 presents the image of a tumor acquired on mice 2 before any injection of gold nanoparticles. It is presented here because the histology later revealed that this tumor, unlike all the tumors of the other mice, was only partially necrotic and had a viable part. Some photoacoustic signal increase might have been observed in some part of the tumor after gold nanoshells injection in the tail vein but were not convincing enough to draw any firm conclusion. However, it is interesting to see that that some blood vessel probably going to the tumor can be seen on this photoacoustic image, for example close to the top of the tumor.

4.3 Conclusion

Two different acoustic-resolution photoacoustic imaging systems were presented. The first one, based on raster scanning a single element high frequency focused transducer was used to image optical absorbers embedded in optically scattering phantoms. Both two dimensional and three dimensional photoacoustic images of tubes and cylinder with different sizes were acquired. An ultrasound image of one of the samples was also acquired illustrating the image contrast difference in photoacoustic and ultrasound imaging. The second imaging system was based on the use of a linear array probe and a commercial ultrasound scanner. It was used to investigate the distribution of gold nanorods and gold nanoshells of different sizes in the tumor of a living mouse. Tumor images could be acquired and gold nanorods detected when directly injected close to the tumor. However, because the tumors were almost all entirely necrotic as a further histology analysis revealed, no photoacoustic signal from gold nanoparticles could be detected after their injection in the mouse tail vein.

There are several limitations to the work presented here. First, only phantoms were imaged using the focused transducer system, and not biological tissues. In particular, these phantoms were not acoustically attenuating. Concerning the system itself, its transmission configuration strongly limits its potential applications. Moreover, it has a slow imaging speed mainly because of the low 10 Hz repetition rate of the laser. Second, gold nanoparticles could not be detected in the tumors of living mice using the linear array system after their injection in the tail veins of the mice. Although this was most probably due in part to the fact that the xenografted tumors were necrotic, some aspects of the system made the measurements difficult. Mainly, because a needle and a syringe were used for the injection of the gold nanoparticles in the tail vein, movement of the mice during the injection were almost inevitably induced thus preventing the real time monitoring of the tumor during the injection and making the comparison with images after the injection more hazardous. Concerning the system itself, the illumination strategy used here made it very difficult to provide an identical illumination on the mice from an imaging session to another.

To improve the imaging performance of the focused transducer based system, the light delivery system should be modified so that imaging in reflection mode is possible. In order to do so, different light delivery methods based on solutions described in the literature, such as the use of an optical condenser, a light ring or an optical fiber fixed to the transducer have already been developed but were not presented in the thesis or applied to biological tissue

imaging because our work was then orientated towards a different objective presented in the following chapter 5. To study the distribution of gold nanoparticles in tumors in living, the use of a catheter for the injection may provide a useful help. The system should also be slightly modified to enable the imaging under more reproducible conditions. Unfortunately the biologist with whom we were collaborating on this work, Dr. Mariana Varna, moved to another laboratory before we could make new experiments.

In the following chapter, the photoacoustic imaging system based on a single element high frequency focused transducer is slightly modified to experimentally investigate photoacoustic thermal nonlinearity.

Chapter 5

Experimental investigation of photoacoustic thermal nonlinearity

Contents

5.1	Background and principle	103
5.1.1	Photoacoustic generation by a gold nanosphere	103
5.1.2	Photoacoustic generation by a collection of gold nanospheres	109
5.2	Materials and methods	114
5.2.1	Experimental setup	114
5.2.2	Practical considerations	116
5.3	Results	118
5.3.1	Results as a function of fluence	118
5.3.2	Influence of the equilibrium temperature	120
5.4	Conclusion	121

In the previous chapter, a high frequency acoustic-resolution photoacoustic imaging setup was built and used to image phantoms. Here, this setup is slightly modified and used to study the photoacoustic generation by aqueous solutions of different types of absorbers at various temperatures between 2 °C and 4 °C and fluences well below the 20 mJ cm⁻² safety limit. The objective of this chapter is to demonstrate the ability to discriminate between different types of absorbers, an organic dye and gold nanospheres, based on thermal nonlinearity, that is in a regime that precludes phase transitions such as involved in bubble formation. This could lead to the development of a new type of contrast in photoacoustic imaging, thermal nonlinearity contrast, to an increased accuracy of the photoacoustic temperature measurement involving gold nanospheres, and to gold nanospheres considered as having the ability to thermally probe their environment at nanometers scale.

We first give an introduction to the so-called thermal nonlinearity and to the photoacoustic generation by gold nanospheres and to its difference with that by an organic dye, based on theoretical predictions by Prost [2014]. The experimental setup used to discriminate between an organic blue dye and a 40 nm gold nanospheres aqueous solution based on this thermal nonlinearity is then described. Finally, the experimental results are presented and qualitatively compared with the predictions from [Prost, 2014].

5.1 Background and principle

5.1.1 Photoacoustic generation by a gold nanosphere

Physical and numerical simulation model

The mathematical description of the photoacoustic generation by a gold nanosphere immersed in water and illuminated by a nanoseconds light pulse is quite complex. Indeed, because the gold nanosphere has a dimension of typically several tens of nanometers, neither the stress nor the heat confinement conditions are verified. Moreover, illumination

of such a nanosphere at its plasmon resonance optical wavelength may induce significant temperature rise in its vicinity at optical fluences of only several mJ cm^{-2} because of its strong optical absorption. This might lead to several phenomena inducing a nonlinear relationship between the incident fluence on the gold nanosphere and the amplitude of the generated photoacoustic wave, for example the creation of nano or microbubbles or the variations of the mechanical and thermodynamic parameters. At low fluences, below the skin irradiation safety limits of about 20 mJ cm^{-2} , only this last type of phenomena, that will be called thermal nonlinearity, is susceptible to be observed as the induced temperature rises are not sufficient for phase transition to take place. It is however worth noticing that nucleation due to absorption of nanoseconds light pulses is a complex process that require the particle surrounding water temperature to exceed a threshold on the order of 590 K [Pustovalov et al., 2008]. Thus water temperatures higher than 373 K in the gold nanosphere vicinity are not incompatible with the absence of phase transitions due to the light pulse. The only type of photoacoustic nonlinearity considered in this chapter will be the thermal nonlinearity, related to the temperature-dependence of the thermal expansion coefficient in the following equation [Prost, 2014]:

$$\Delta p(\mathbf{r}, t) - \frac{1}{c_s^2} \frac{\partial^2 p}{\partial t^2}(\mathbf{r}, t) = -\rho_0 \frac{\partial}{\partial t} \left(\beta(T) \frac{\partial T}{\partial t}(\mathbf{r}, t) \right) \quad (5.1)$$

From a theoretical point of view the prediction of the photoacoustic wave emitted by a gold nanosphere requires to first solve the heat diffusion equation 1.9 in order to compute the temperature field $T(\mathbf{r}, t)$, and then to solve the acoustic wave equation 1.10 with this temperature field in the source term. Taking into account the temperature dependence of the mechanical and thermodynamic parameters makes this problem very complex and analytically intractable. A numerical resolution method was thus developed during a recent PhD thesis in our group to solve this photoacoustic generation problem [Prost, 2014]. The heat diffusion equation is solved analytically for an impulse laser illumination $\delta(t)$. The temperature field is then computed analytically by the convolution of the temperature field induced by the impulse illumination with a function dictated by the temporal profile of the illumination. This is achieved numerically. Finally the acoustic wave equation, with the previously computed temperature field in the source term, is solved by a finite-difference time-domain approach. The pressure waveform p_{surf} in water at the nanosphere surface is computed as the final result.

The heat diffusion equation and the acoustic wave equation are solved in both the gold nanosphere and in the surrounding water with the appropriate boundary conditions but several approximations were made to simplify the equations resolution. The optical absorption of water was neglected as negligible compared to absorption in the gold nanosphere. The elastic wave equation in the gold nanosphere was written based on Hooke's law in solid undergoing small deformations. The temperature inside the gold nanosphere was considered to be homogeneous because the typical times it would take for heat to diffuse over the volume of several tens of nanometers diameters gold nanospheres are very small compared to the nanoseconds duration of the light pulses considered here. These times, $\tau_{th,g} = \frac{D^2}{\chi_g}$ where D is the gold nanosphere diameter and $\chi_g \approx 1.27 \times 10^{-4} \text{ m}^2 \text{ s}^{-1}$ is the thermal diffusivity of water, are indeed of the order of picoseconds. More importantly, the temperature was assumed to be continuous at the gold nanosphere/water boundary, thus neglecting the interface thermal resistance which might have a significant impact on the photoacoustic generation according to recent experimental works [Chen et al., 2011]. Only the temperature dependence of the water thermal expansion coefficient was taken into account. Indeed, among all the gold and water mechanical and thermodynamic parameters, it was shown that its temperature dependence is the one that most significantly affects the photoacoustic generation in the thermal nonlinear regime. The temperature dependence of the other gold and water mechanical and thermodynamic parameters can be neglected without introducing significant errors [Prost, 2014]. The numerical simulations showed that, in good agreement with previous experiments [Chen et al., 2012], in the case of nanoseconds light pulses, more than about 90% of the emitted photoacoustic wave is generated by the surrounding water rather than by the gold nanosphere itself. This is due to the fact that thermal expansion coefficient of water is about one order of magnitude greater than that of gold, and to the several tens of nanometers over which temperature has time to diffuse during the nanoseconds duration of the light pulse. The temperature dependence of the water thermal expansion coefficient β is represented on figure 5.1 [Lide, 2007]. It is interesting to note that this coefficient vanishes at a temperature of 4°C and that its variations are significant in the represented temperature range.

Predictions from the numerical simulations

Influence of the fluence on the photoacoustic amplitude It was predicted that the impact on the photoacoustic generation of the temperature variation of the water ther-

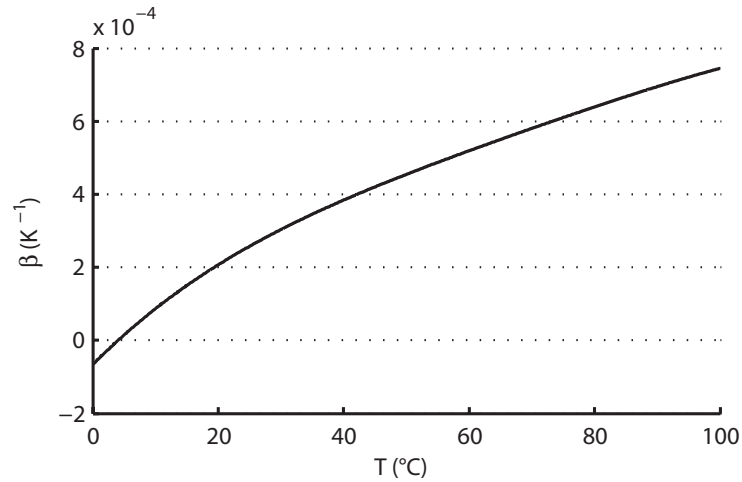


Figure 5.1 – Water thermal expansion coefficient β as a function of temperature, taken from [Prost, 2014].

mal expansion coefficient β would be the strongest for gold nanospheres diameters in the 40 to 120 nm range [Prost, 2014] for nanoseconds light pulses. For example, for a 40 nm gold nanosphere illuminated by a 5 ns and 5 mJ cm^{-2} light pulse, the expected temperature increase of 120 K in the gold nanosphere would significantly affect the value of β in its vicinity. This can be seen for example on figure 5.2 which represents the amplitude of the photoacoustic wave generated by a 40 nm gold nanosphere, immersed in a $T_0 = 20^\circ\text{C}$ water solution and illuminated by a 532 nm, 5 ns and 5 mJ cm^{-2} light pulse, in the linear regime, where β is taken as a constant, and in the nonlinear regime, where $\beta(T(\mathbf{r}, t))$ is taken as a function of the temperature field. When the temperature variations of the thermal expansion coefficient are taken into account, a nonlinear dependence of the generated photoacoustic wave amplitude with the incident fluence is observed. Figure 5.2 predicts that thermal nonlinearity has a significant impact on the photoacoustic amplitude dependence with the incident fluence and should thus be observable even at low fluences of a few mJ cm^{-2} .

Impact in the frequency domain The thermal nonlinearity not only impacts the amplitude of the generated photoacoustic wave but also the shape of its temporal profile which changes from a bipolar shape in the linear regime to a tripolar shape in the nonlinear regime. The spectrum of the generated photoacoustic wave is thus affected by thermal nonlinearity. It was shown that it is in fact shifted towards the high frequencies in the

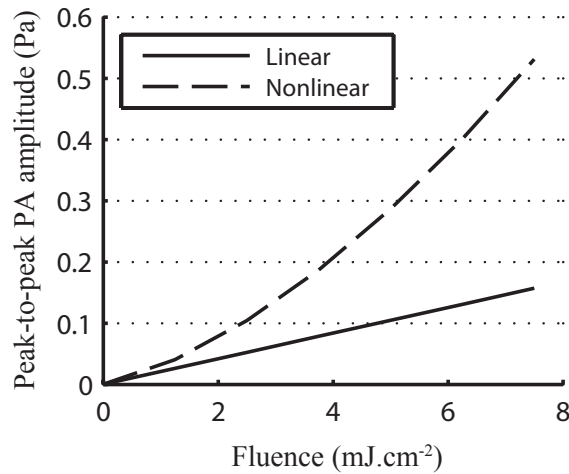


Figure 5.2 – Peak-to-peak amplitude of the photoacoustic wave generated by a 40 nm diameter gold nanosphere, immersed in a $T_0 = 20^\circ\text{C}$ water solution and illuminated by a 532 nm and 4 ns light pulse, as a function of the incident fluence in the linear (β taken as a constant) and nonlinear regime.

nonlinear regime [Prost, 2014]. This can be seen on figure 5.3 which represents the spectra, normalized by the incident fluence, of the photoacoustic waves generated by a 40 nm gold nanosphere, immersed in a $T_0 = 20^\circ\text{C}$ water solution, and illuminated by a 532 nm and 5 ns light pulse, in the linear regime and in the nonlinear regime for incident fluences of 6.5, 32.5 and 65 mJ cm^{-2} . The nonlinear dependence of the generated photoacoustic waves amplitude on the incident fluence is illustrated by the fact that the functions do not coincide. It can be seen that, in the nonlinear regime, the spectra are shifted towards high frequencies as fluence increases indicating that thermal nonlinearity is stronger for high frequencies.

Influence of the temperature on the photoacoustic amplitude The thermal expansion coefficient can be written as:

$$\beta(T(\mathbf{r}, t)) = \beta(T_0 + \delta T(\mathbf{r}, t)) \quad (5.2)$$

where T_0 is the medium equilibrium temperature and $\beta(\mathbf{r}, t)$ is the temperature increase due to the optical absorption. Thus, the thermal expansion coefficient is a function of both the medium equilibrium temperature and the incident fluence through the temperature increase. This is illustrated on figure 5.4 where the amplitude of the generated photoacous-

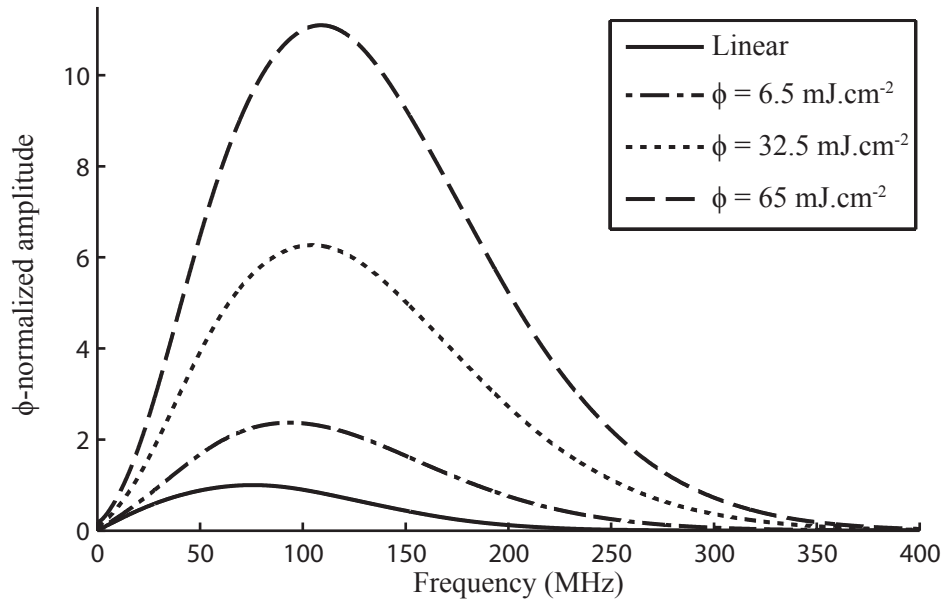


Figure 5.3 – Spectra, normalized by the incident fluences Φ , of the photoacoustic signal generated by a 40 nm gold nanosphere, immersed in a $T_0 = 20^\circ\text{C}$ water solution and illuminated by a 532 nm and 5 ns light pulse, in the linear regime (β taken as a constant) and for three different fluences Φ in the nonlinear regime, taken from [Prost, 2014].

tic waves, normalized at 40°C , are represented as a function of the medium equilibrium temperature, for different incident fluences ranging from $0.1 \mu\text{J cm}^{-2}$ to 10 mJ cm^{-2} . The water thermal expansion coefficient is also represented as a function of the water equilibrium temperature. At low fluences, the thermal expansion coefficient is not significantly affected by the small temperature rises around the gold nanosphere during the light pulse and the generated photoacoustic waves amplitude dependence on the medium equilibrium temperature follows that of the thermal expansion coefficient of water. At higher fluences, the thermal expansion coefficient is significantly affected by the temperature rises around the gold nanosphere during the light pulse and the generated photoacoustic waves amplitude dependence on the medium temperature differ significantly from that of the water thermal expansion coefficient. For a water equilibrium temperature of 4°C in water, the value of the water thermal expansion coefficient is zero and thus there should be no generated photoacoustic waves in the linear regime. Thus, at this temperature the photoacoustic generated waves are due only to the thermal nonlinearity and the significant temperature rises around the gold nanosphere. This is in good agreement with the fact that there are some generated photoacoustic signals only at sufficiently high fluences. It is interesting to

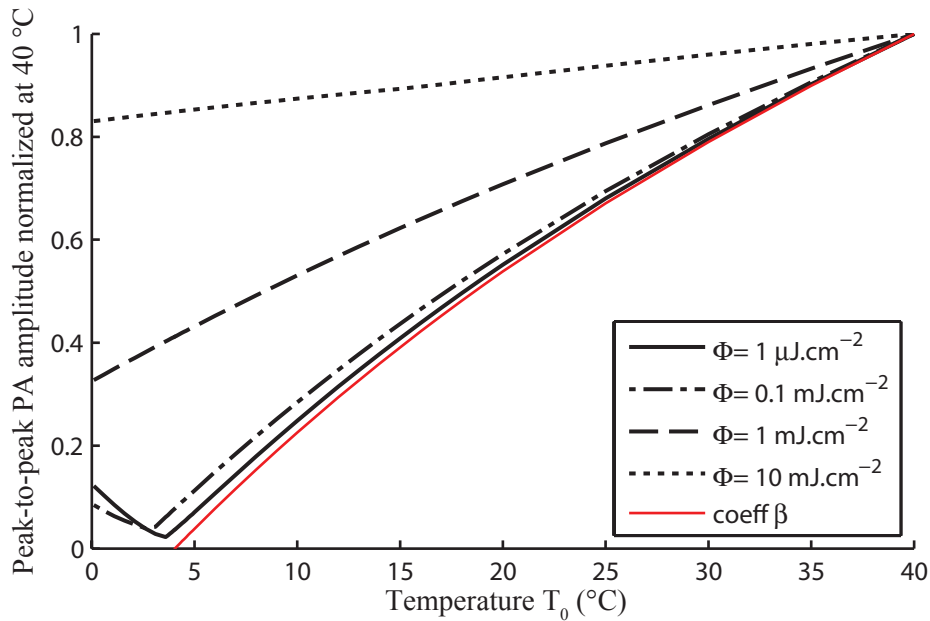


Figure 5.4 – Peak-to-peak amplitude, normalized at $T_0 = 40\text{ °C}$, of the photoacoustic waves generated by a 40 nm diameter gold nanosphere, immersed in a T_0 water solution and illuminated by a 532 nm and 5 ns light pulse, as a function of the water equilibrium temperature T_0 for four different fluences Φ . The values of the thermal expansion coefficient of water, normalized at $T_0 = 40\text{ °C}$, are also represented as a function of the temperature T_0 to compare their variations with these of the peak-to-peak amplitudes of the generated photoacoustic waves. Taken from [Prost, 2014].

observe that even at low fluences at $T_0 = 4\text{ °C}$ there are some very low amplitude photoacoustic waves generated. These photoacoustic waves are due to the contribution of the gold nanosphere itself, which is negligible at room temperature but that can be seen as the thermal expansion coefficient of water reaches zero while the one of gold remains finite.

5.1.2 Photoacoustic generation by a collection of gold nanospheres

Generalization from the results for a single gold nanosphere

Photoacoustic imaging usually involves not a single gold nanosphere as was considered in the previous section 5.1.1, but generally a collection of gold nanospheres (except for some photoacoustic microscopy setups designed for detecting single nanoparticles). The photoacoustic wave generated by a collection of nanospheres might be quite different from the photoacoustic waves generated by each individual gold nanosphere. We consider a water

volume Ω_1 of characteristic dimension L_1 , with a speed of sound c_s , containing a collection of N identical gold nanospheres of optical absorption cross-section σ_a , radius R_s , and illuminated by a light pulse of duration τ_p . It is considered that the medium acoustic and thermal properties are homogeneous and that its optical absorption coefficient $\mu_a = \frac{N}{V}\sigma_a$ is sufficiently small so that $\frac{1}{\mu_a} \gg L_1$ and the fluence in the medium is homogeneous. Provided that the characteristic distance between the gold nanospheres $l_1 = \frac{V_1}{N}^{1/3}$ is large compared to the spatial extension of the photoacoustic waves generated by each individual gold nanosphere $l_{ac} = c_s\tau_p$, the photoacoustic waves generated by the volume Ω_1 is the sum of all the photoacoustic wave generated by each individual gold nanosphere, and can be written as a continuous integral:

$$\begin{aligned} p(\mathbf{r}, t) &= \frac{\mu_a}{\sigma_a} \iiint_{\mathbf{r}' \in \Omega_1} \frac{R_s}{\|\mathbf{r} - \mathbf{r}'\|} p_{\text{surf}} \left(t - \frac{\|\mathbf{r} - \mathbf{r}'\|}{c_s} \right) d^3\mathbf{r}' \\ p(\mathbf{r}, t) &= 4\pi R_s \frac{\mu_a}{\sigma_a} \int_{t \in \mathbb{R}_+} \left[\iiint_{\mathbf{r}' \in \Omega_1} \frac{1}{4\pi\|\mathbf{r} - \mathbf{r}'\|} \delta \left(t' - \frac{\|\mathbf{r} - \mathbf{r}'\|}{c_s} \right) d^3\mathbf{r}' \right] p_{\text{surf}}(t - t') dt' \end{aligned} \quad (5.3)$$

Equation 5.3 can also be written as:

$$p(\mathbf{r}, t) = 4\pi R_s \frac{\mu_a}{\sigma_a} H(\mathbf{r}, t) *_t p_{\text{surf}}(t) \quad (5.4)$$

where

$$H(\mathbf{r}, t) = \iiint_{\mathbf{r}' \in \Omega_1} \frac{1}{4\pi\|\mathbf{r} - \mathbf{r}'\|} \delta \left(t - \frac{\|\mathbf{r} - \mathbf{r}'\|}{c_s} \right) d^3\mathbf{r}' \quad (5.5)$$

Equation 5.4 shows that the photoacoustic wave generated by the collection of gold nanospheres in the volume Ω_1 is the filtered version of the photoacoustic waves generated by each individual gold nanosphere, the filtering function $H(\mathbf{r}, t)$ being dictated by the geometrical properties of the collection volume Ω_1 .

If the collection volume Ω_1 is a sphere of diameter L_1 $H(\mathbf{r}, t)$ reduces to:

$$H(\mathbf{r}, t) = \frac{c_s}{4\|\mathbf{r}\|} \left(\frac{L_1^2}{4} - (\|\mathbf{r}\| - ct)^2 \right) \quad (5.6)$$

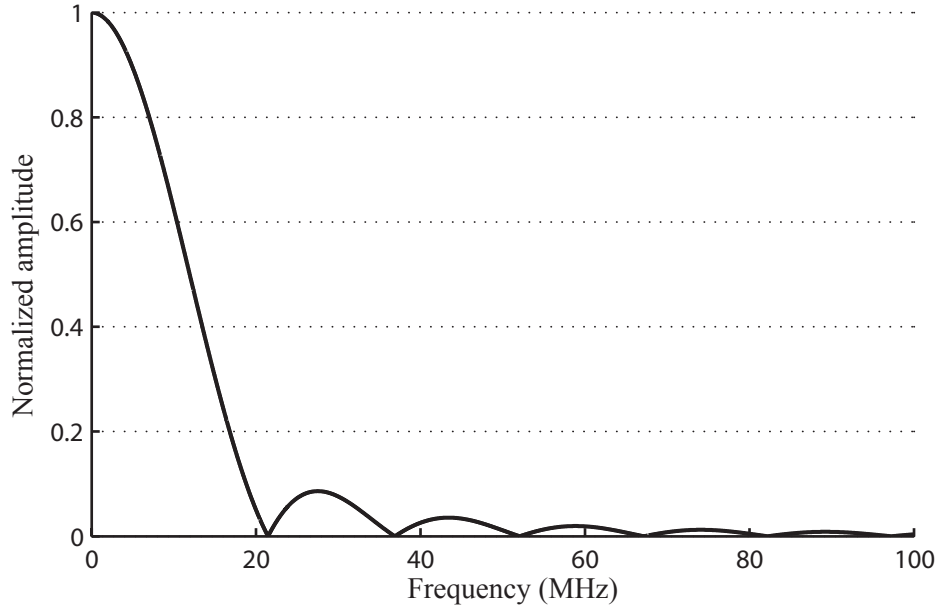


Figure 5.5 – Normalized amplitude of the filtering function $\tilde{H}(\mathbf{r}, \hat{q})$ as a function of the frequency ν in the case of a water spherical volume of diameter $L_1 = 100 \mu\text{m}$ with a speed of sound $c_s = 1500 \text{ m s}^{-2}$, taken from [Prost, 2014].

The Fourier transform of this function is:

$$\tilde{H}(\mathbf{r}, \hat{q}) = \frac{L_1^3}{8\|\mathbf{r}\|} e^{-i\hat{q}\frac{2\|\mathbf{r}\|}{L_1}} \left(\frac{\sin(\hat{q})}{\hat{q}^3} - \frac{\cos(\hat{q})}{\hat{q}^2} \right) \quad (5.7)$$

where $\hat{q} = \frac{\pi\nu L_1}{c_s}$.

The normalized amplitude of the function $\tilde{H}(\mathbf{r}, \hat{q})$ is presented on figure 5.5 as a function of the frequency ν in the case of a water spherical volume of diameter $L_1 = 100 \mu\text{m}$ with a speed of sound $c_s = 1500 \text{ m s}^{-2}$.

It is interesting to observe that the function $H(\mathbf{r}, t)$ is equivalent to the antiderivative of the function describing the photoacoustic pressure wave generated by an absorbing sphere of diameter L_1 in the stress confinement regime given by equation 1.19. This is easily understood when using the Green's function approach to solve the equations 1.9 and 1.10 using the Green's function approach [Prost, 2014].

The filtering by the function $H(\mathbf{r}, t)$ has a significant impact on the photoacoustic wave generated by a collection of gold nanospheres compared to that of a single gold nanosphere. Indeed, as can be seen on figure 5.5 the filtering function $H(\mathbf{r}, t)$ significantly attenuates the

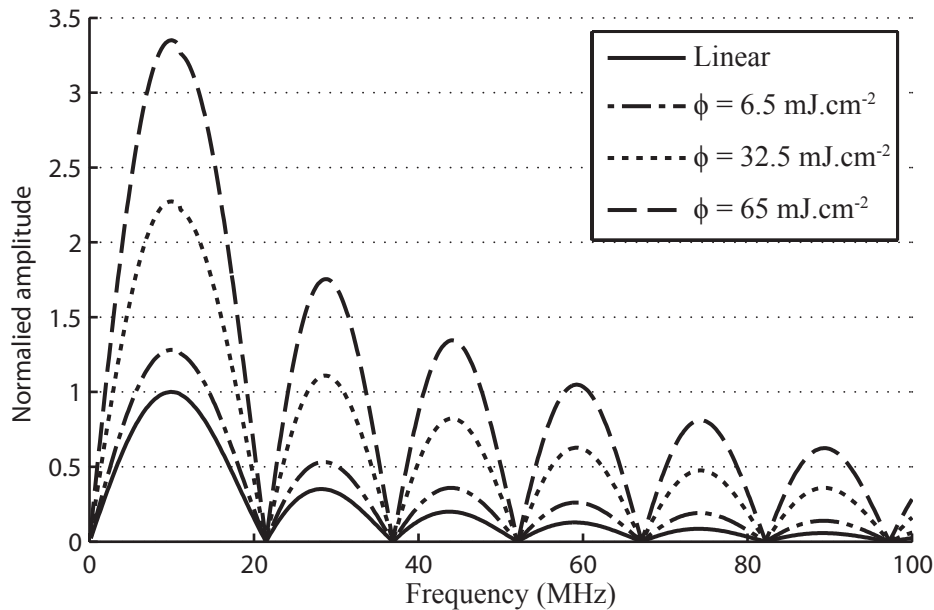


Figure 5.6 – Spectra, normalized by the incident fluence Φ , of the photoacoustic signals generated by a $L_1 = 100 \mu\text{m}$ diameter spherical collection of 40 nm gold nanospheres, immersed in a $T_0 = 20^\circ\text{C}$ water solution and illuminated by a 532 nm and 5 ns light pulse, in the linear regime (β taken as a constant) and for three different fluences in the nonlinear regime. These spectra were obtained by filtering the spectra represented on figure 5.3 for a single 40 nm gold nanosphere with the filtering function $\tilde{H}(\mathbf{r}, \hat{q})$ represented on figure 5.5. Taken from [Prost, 2014].

photoacoustic waves high frequencies generated by a single gold nanosphere. This is particularly important in the context of thermal nonlinearity which effects are stronger at high photoacoustic waves frequencies as mentioned in section 5.1.1 and shown in figure 5.3. The thermal nonlinearity effects are thus expected to be weaker when the photoacoustic wave is generated by a collection of gold nanospheres rather than by a single gold nanosphere. Figure 5.6 represent the spectra of figure 5.3 for a single gold nanosphere filtered by the function of figure 5.5 for a water spherical collection volume of diameter $L_1 = 100 \mu\text{m}$. It can be seen on figure 5.6 that only the low frequencies in the ten to several tens of MHz range are still present in the spectrum of the photoacoustic waves generated by the collection of gold nanospheres. At these frequencies the nonlinear amplitude increase is lower than at the high frequencies generated by a single gold nanosphere. Therefore, the filtering by the spatial extension of the absorbing solution strongly attenuates the thermal nonlinearity impact on the photoacoustic signal.

Comparison with the photoacoustic generation by a molecular organic dye

In the linear regime, the photoacoustic waves generated by a solution of organic dye molecules or of gold nanospheres will be the same if the solutions spatial extension are the same, the distance between the particles are small compared to $\frac{c_s}{\tau_p}$ and the macroscopic optical absorption coefficients of the solutions are identical. In the thermal nonlinear regime, taking into account the temperature dependence of the thermal expansion coefficient, this will not be the case anymore. Indeed, because the optical absorption cross-section of gold nanospheres is orders of magnitudes higher than that of the organics dye molecules [Jain et al., 2006], the temperature rise around the gold nanoparticles will be much higher than around the organic dye molecules, thus inducing strong thermal nonlinearity in the case of the gold nanospheres but not in the case of the organic dye molecules. In fact, at the optical densities used in this chapter, around 10, the distance between the gold nanospheres in the solution is about 1 μm , considering gold nanospheres optical absorption cross-sections of about $3.3 \times 10^{-15} \text{ m}^{-2}$. Therefore, because this is much greater than the distance over which heat has time to diffuse during a 5 ns light pulse, about $l_{th} = \chi\tau_p \approx 50 \text{ nm}$, the temperature field inside the gold nanospheres solution during the light pulse is highly heterogeneous with significant temperature peaks in the vicinity of the gold nanospheres. This will not be the case in an organic dye solution of identical optical density where the light pulse will be absorbed by a much larger number of organic dye molecules with as much lower absorption cross-sections. Because of the reduced distance between the organic dye molecules, a homogeneous temperature field is induced during the 5 ns light pulse with a maximum temperature rise on the order of $\Delta T \approx 10 \text{ mK}$ for a 5 mJ cm^{-2} and 5 ns light pulse. This is much lower than the about 120 K maximum temperature rise induced around the gold nanospheres under the same illumination conditions close to their plasmon resonance.

The main objective of this chapter is to discriminate between a solution of organic dye molecules and a solution of gold nanospheres of identical macroscopic optical properties, based on thermal nonlinearity through the differences in the temperature rises induced for the two types of solutions. On the one hand, in the case of gold nanospheres, strong nanoscale temperature rise may take place in the absorbers vicinity inducing significant thermal nonlinear effect. On the other hand, in the case of the organic dye solution only a weak homogeneous temperature rise should take place, inducing negligible thermal expansion coefficient variations, and the solution thus behaving as expected in the linear

regime.

5.2 Materials and methods

5.2.1 Experimental setup

The acoustic-resolution photoacoustic imaging setup described in section 5.2.1 was adapted to detect photoacoustic signals from a polycarbonate tube filled with aqueous solutions. This setup indeed enables the use of a high frequency transducer chosen to favor the observation of photoacoustic nonlinearities, as suggested by the simulations predictions presented in section 5.1. The experimental setup is illustrated in figure 5.7. Nanoseconds pulses from a Q-switched laser (wavelength 532 nm, pulse duration 4 ns, repetition rate 10 Hz, Brilliant, Quantel, France) were directed towards the sample. The beam was shaped by the combination of a lens ($f' = 75$ mm, LA1608, Thorlabs, USA) and an engineered diffruser (EDC-10, RPC Photonics, USA) so that the laser illumination was homogeneous on the tube in the focal region of the transducer. The photoacoustic signals were detected with a 20 MHz spherically focused transducer (20.8 MHz central frequency, 14.5–27.0 MHz –6 dB bandwidth, 12.7 mm focal distance, 6.3 mm diameter, PI20-2-R0.50, Olympus, Japan), amplified (DPR500, remote pulser RP-L2, JSR Ultrasonics, USA) and digitized with an oscilloscope (DLM 2024, Yokogawa, Japan).

Polycarbonate tubes with a 100 μm inner diameter (200 μm outer diameter, CTPC100-200, Paradigm Optics, USA) were used to approximately match the frequency of the emitted photoacoustic waves to that of the transducer. The tubes were filled with aqueous solutions of either 40 nm diameter gold nanospheres (HD.GC40.OD10, BBI Solutions, UK) or an organic blue dye (colorant E133, acidifier E330, preservative E202, ScrapCooking, France). The dilutions for each type of absorbers were set to obtain similar optical densities of about 10 (± 0.1) at 532 nm. 532 nm was chosen as the excitation wavelength as it is close to the absorption peak of gold nanospheres with diameters on the order of a few tens of nanometers.

For both samples, the peak-to-peak amplitude of the photoacoustic signal was studied as a function of either the incident fluence or the equilibrium temperature. The tubes were immersed in a large water tank providing a slow varying equilibrium temperature

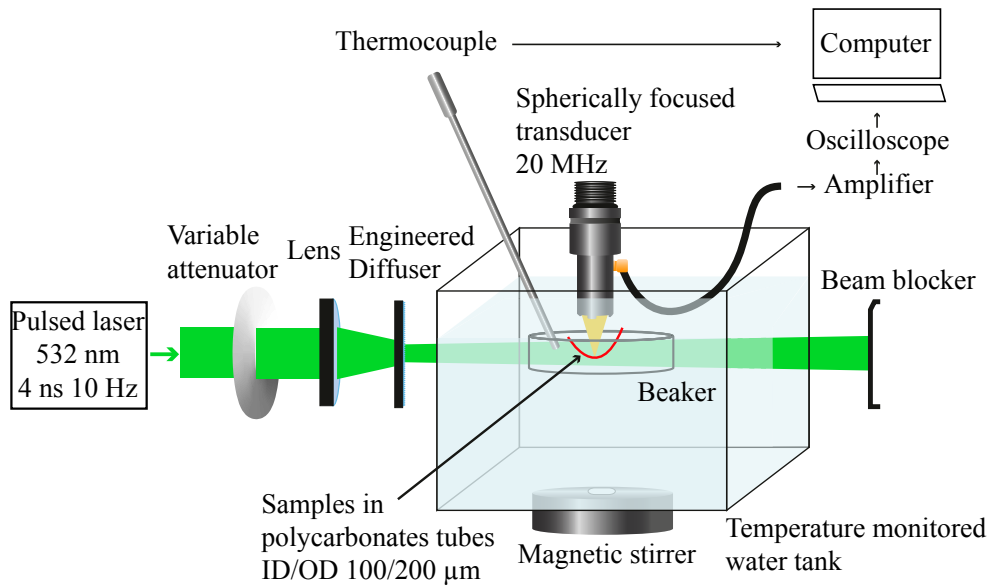


Figure 5.7 – Experimental setup used to investigate photoacoustic thermal nonlinearity from various absorbing solutions as a function of fluence and equilibrium temperature.

T_0 when the water temperature was different from the room temperature. Temperature was monitored using a thermocouple (type K, RS Components, UK) placed in the vicinity of the tube, and connected to a computer via a thermocouple data logger (TC-08, Pico Technology, UK). A magnetic stirrer was used to maintain a homogeneous temperature distribution in the water tank. The tube was fixed on a beaker to prevent motion induced by water convection. A hot air flow was used to prevent condensation to form and perturb the laser beam on the entrance wall of the water tank. The incident fluence was controlled using a laser-integrated variable attenuator. For each position of the attenuator, the fluence values on the sample were deduced from a prior calibration and direct measurements of the average laser output powers using a thermal power meter. From a sample to the other, only the position of the tube was adjusted so as to be in the focus of the transducer and within the area where the calibration for the fluence remained valid. To improve the signal-to-noise ratio, the signals were coherently averaged on the oscilloscope ($N_{av} = 32$ or 64 depending on the experiment, see section 5.3), before the peak-to-peak value computed on the scope was transferred to the computer. The system noise was estimated from measurements with no illumination on the samples.

For two equilibrium temperature $T_0 = 4^\circ\text{C}$ and $T_0 = 20^\circ\text{C}$, the fluence was varied from 0 up to approximately 7 mJ cm^{-2} . For $T_0 = 4^\circ\text{C}$, water cooled in a freezer was used,

the temperature of the tank remained around 4 ± 0.5 °C during the few minutes of the experiment over which the incident fluence was varied. The experiments at $T_0 = 20$ °C were done at room temperature. To study the evolution of the photoacoustic signal as a function of T_0 from 2 °C to 20 °C, the incident fluence was fixed at 5 mJ/cm², and the water tank initially filled with water from a freezer (at $T_0 < 2$ °C). As the temperature slowly raised towards room temperature, both the water temperature and the photoacoustic signals were simultaneously measured and stored in the computer every 30 seconds. The same protocol was used for the two types of absorbing solutions (dye and gold nanospheres). For both samples, each type of experiment was repeated at least 3 times, and turned out to be reproducible.

5.2.2 Practical considerations

The experimental setup described in the previous section 5.2.1 is quite simple however there are a few aspects of this setup that were only briefly mentioned but that are of significant importance in practice.

The use of a magnetic stirrer proved to be essential in order to maintain a homogeneous temperature in the water tank. This was especially true at low temperature, below and around 4 °C where strong temperature temporal fluctuations were measured most probably because of the water convection movements induced by the increasing density of water between 0 °C and 4 °C.

The drawback of using a magnetic stirred was that the created water movements induced significant oscillations of the polycarbonate tubes inside the small focal region of the transducer. The use of a small beaker on which the polycarbonate tube were fixed was thus necessary to prevent these oscillations from perturbing the measurements of the photoacoustic signals.

The use of an hot air flow to prevent condensation formation on the laser entrance wall of the water tank was also essential when cold water significantly below ambient temperature was used. Indeed, it appeared that the formed condensation induced strong laser beam deviations and thus perturbations of the incident fluences.

The use of a microlens array enabled the laser illumination on the polycarbonate tubes to be homogeneous. This was very important, despite the small size of the observed region

of the absorbers limited to the focal region of the transducer because of the presence of strong hot spots in the beam profile of the laser used.

The absorbers dilutions to obtain similar optical densities of about 10 were based on extinction measurement made with a spectrometer. These measurements could be approximated as being optical absorption measurements because of the negligible optical scattering of both absorbers compared to their optical absorption. This could be seen for the organic blue dye by the transparent aspect of the solution. For the 40 nm diameter gold nanospheres solution it was due to their negligible optical scattering cross-section compared to their optical absorption cross-section for this small diameter [Jain et al., 2006]. The measurement of the optical absorption spectra of the gold nanospheres solution enabled to verify that no aggregation had occur in the samples prior to their injection inside the polycarbonate tubes.

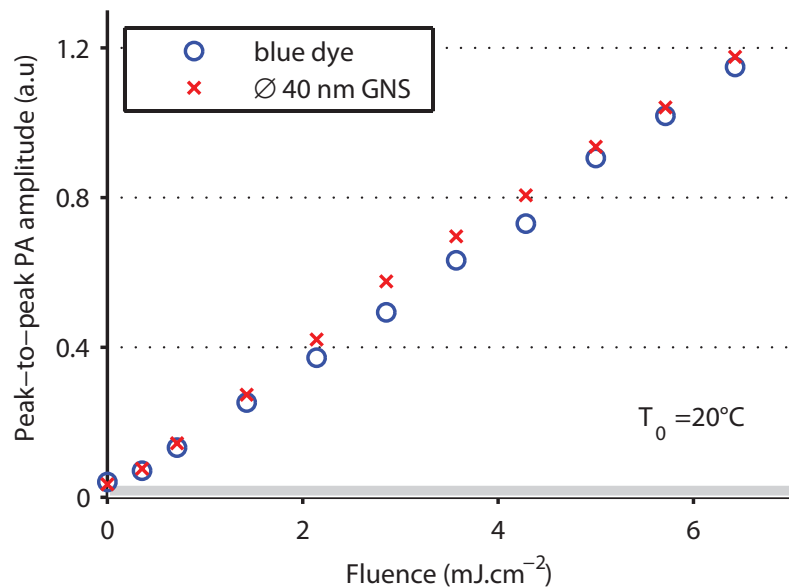


Figure 5.8 – Peak-to-peak photoacoustic amplitude measured as a function of the incident fluence Φ , at an equilibrium temperature of $T_0 = 20^\circ\text{C}$, using the setup described in section 5.2.1, for an organic blue dye aqueous solution and a 40 nm gold nanospheres aqueous solution. The grey bar indicates the noise level.

5.3 Results

5.3.1 Results as a function of fluence

Experiments at $T_0 = 20^\circ\text{C}$

Figure 5.8 represent the peak-to-peak amplitude of the photoacoustic waves generated by the organic blue dye and the gold nanospheres solutions, for an equilibrium temperature of the water tank of 20°C , as a function of the incident fluence. The detected signals were averaged 32 times to improve the signal-to-noise ratio. The noise level, defined as the peak-to-peak amplitude of the detected signals when the samples were not illuminated, is represented by a grey bar. The noise level will be defined identically in the following figures 5.9 and 5.10. The signal-to-noise ratio for an incident fluence of 5 mJ cm^{-2} was about 25 for both solutions as can be seen on figure 5.8.

The fluence dependence of the photoacoustic signals detected from the organic blue dye aqueous solution is linear as expected. The signals detected from the gold nanospheres solution also varies linearly with the incident fluence, as opposed to what was predicted by figure 5.2. However 5.2 predicts the peak-to-peak amplitude of the unfiltered signals, whereas in the experiment the photoacoustic signals were filtered by both the detection bandwidth and the spatial extension of the absorbing excited solution. The fact that a linear behavior was observed is possibly due to the fact that the frequencies of the detected signals were not high enough to observe a significant nonlinear contribution. As explained in section 5.1.2 figure 5.6 indeed shows that a $100\text{ }\mu\text{m}$ diameter aqueous spherical solution of 40 nm diameter gold nanospheres principally emits photoacoustic waves at low frequencies in the few tens of MHz range at which the thermal nonlinearity is weaker than at the high several tens of MHz to hundreds of MHz frequencies emitted by a single gold nanosphere. In fact, in the experiment the illuminated absorber region is not a sphere but rather a cylinder because of the large centimeter scale illumination on the polycarbonate tubes. This is however of small importance because the filtering function $H(\mathbf{r}, \hat{q})$ of $100\text{ }\mu\text{m}$ diameter cylindrical volumes are very close to that of a $100\text{ }\mu\text{m}$ spherical volume. The filtering function $\tilde{H}(\mathbf{r}, \hat{q})$ of a $100\text{ }\mu\text{m}$ diameter infinite cylinder can be found in [Prost, 2014]. Its shape is essentially the same as for a spherical volume of identical diameter although with a slightly stronger high frequency attenuation and lower lobes peak frequencies. Another

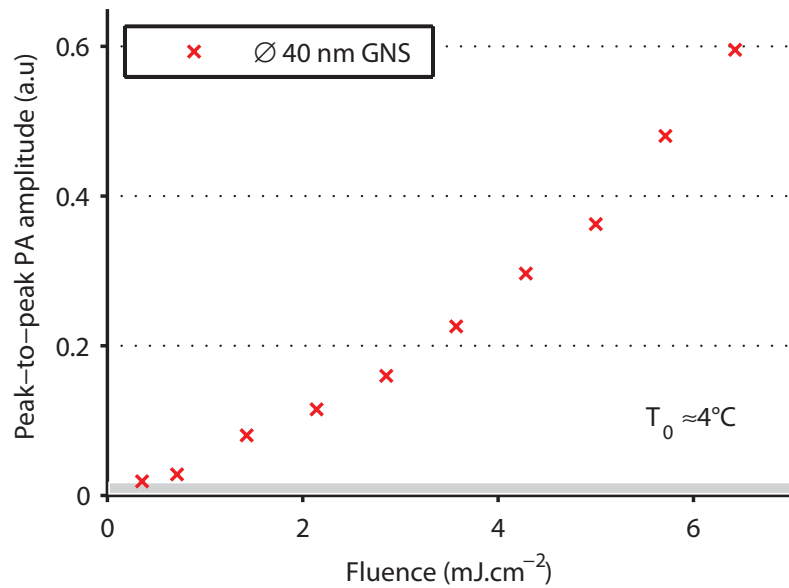


Figure 5.9 – Peak-to-peak photoacoustic amplitude measured as a function of the incident fluence Φ , at an equilibrium temperature of $T_0 \approx 4^\circ\text{C}$, using the setup described in section 5.2.1, for a 40 nm gold nanospheres aqueous solution. No photoacoustic signal was detected from the organic blue dye aqueous solution at this equilibrium temperature. The grey bar indicates the noise level.

possible reason for the observed discrepancy could be the assumption about the continuity of the temperature field at the nanosphere interface is too strong, and that the theoretical predictions overestimate the thermal nonlinearity.

Experiments at $T_0 = 4^\circ\text{C}$

Figure 5.9 represents the peak-to-peak amplitude of the photoacoustic signals from the gold nanospheres solution, for an equilibrium temperature of the water tank of 4°C , as a function of the incident fluence. The detected signals were averaged 64 times to improve the signal-to-noise ratio. The noise level is represented by a grey bar. As expected, no photoacoustic signals were detected from the organic blue dye solution because of the vanishing value of the water thermal expansion coefficient β around 4°C . The behavior from the solution of gold nanospheres was different from that of the organic blue dye solution. First, a photoacoustic signal well above the noise level could be detected from the gold nanospheres solution. Second, the photoacoustic peak-to-peak amplitude from the gold nanospheres solution shows a clear nonlinear dependence with the incident fluence.

These two behaviors are compatible with the expected significant temperature rise during the light pulse in the vicinity of each individual gold nanosphere. In this case, the water thermal expansion coefficient $\beta(\mathbf{r}, t)$ dynamically changes during the light pulse and in the vicinity of each individual gold nanosphere, thus taking a value that is not zero even if the water tank equilibrium temperature T_0 is 4 °C, enabling the generation of photoacoustic waves and inducing a nonlinear relationship between the incident fluence and the peak-to-peak amplitude of the generated photoacoustic waves. The nonlinear dependence with the incident fluence could be observed at $T_0 = 4$ °C, and not at $T_0 = 20$ °C, because although the nonlinear generation was also predominantly centered at much higher frequency than the detected frequencies, the vanishing linear contribution around 4 °C makes the nonlinear contribution detectable. For $T_0 = 20$ °C the nonlinear contribution is probably too small compared to the linear one.

5.3.2 Influence of the equilibrium temperature

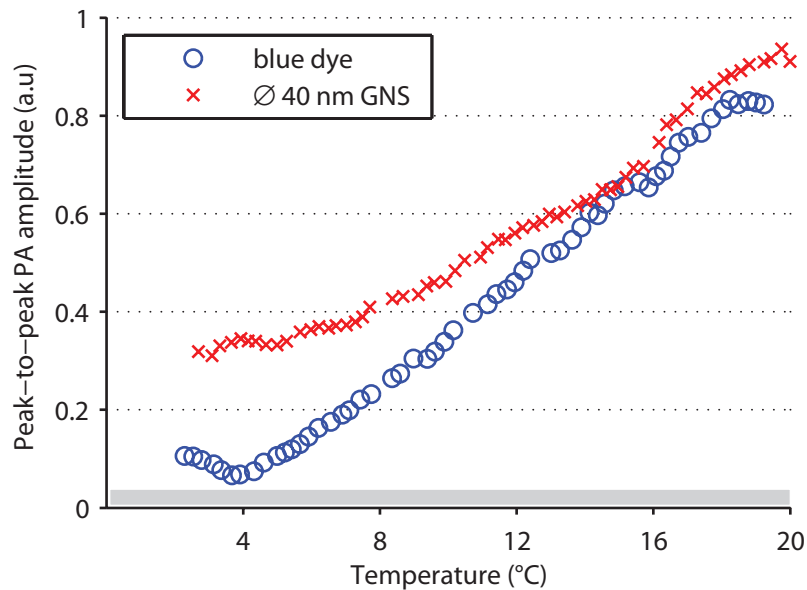


Figure 5.10 – Peak-to-peak photoacoustic amplitude measured as a function of the equilibrium temperature T_0 , for an incident fluence $\Phi = 5 \text{ mJ cm}^{-2}$, using the setup described in section 5.2.1, for an organic blue dye aqueous solution and a 40 nm gold nanospheres aqueous solution. The grey bar indicates the noise level.

Figure 5.10 represents the peak-to-peak amplitude of the photoacoustic signals from the

organic blue dye and the gold nanospheres solutions, for an incident fluence of 5 mJ cm^{-2} , as a function of the water tank equilibrium temperature T_0 . The detected signals were averaged 32 times to improve the signal-to-noise ratio. The behavior of the organic blue dye and the gold nanospheres solutions were very different in good agreements with the predictions from figure 5.6. The temperature dependence of the photoacoustic signals peak-to-peak amplitude detected from the organic blue dye solution closely resemble that of the water thermal expansion coefficient β , while the temperature dependence of the photoacoustic signals peak-to-peak amplitude detected from the gold nanosphere solution was significantly affected by the nanoscale local heating of the water surrounding the gold nanospheres.

5.4 Conclusion

It was shown that two absorbing media, an organic blue dye aqueous solution and a 40 nm diameter gold nanospheres aqueous solution, with the same optical density could be discriminated either from the dependence of photoacoustic amplitude with the incident fluence, at low equilibrium temperature, around 4°C , or from its dependence with the equilibrium temperature. This was possible thanks to the significant change of the water thermal expansion coefficient that took place during the laser illumination for the gold nanospheres solution and which reflects the temperature rise at the nanoscale in their vicinity. A photoacoustic nonlinearity could easily be observed with the gold nanospheres solution, with a detection frequency bandwidth centered around 20 MHz and relatively low fluences below 7 mJ cm^2 , for an equilibrium temperature close enough to 4°C so that the linear contribution is negligible. With the same detection frequency bandwidth and fluences, no photoacoustic nonlinearity could be observed with the gold nanospheres solution for an equilibrium temperature of 20°C . This is possibly due, according to the simulation predictions by [Prost, 2014] presented in section 5.1, to the insufficiently high detection frequencies and the limited fluences used. It might also be that the simulation model is too simple, for example because of the assumption of temperature continuity at the water/gold boundaries which is too strong. To determine the origin of the observed discrepancies between the simulation predictions and the experimental results, the filtering effects by the spatial distribution of gold nanospheres and the detection bandwidth of the transducer should be taken into account in the simulation predictions. Unfortunately

we did not have the time to do it. On the other hand, for a fluence of 5 mJ cm^{-2} , the temperature dependence of the photoacoustic signal peak-to-peak amplitude from the gold nanospheres solution was in qualitative agreement with the theoretical predictions, and allowed to clearly discriminate the two types of absorbing solutions. Partial agreements were thus obtained with the simulation predictions by [Prost, 2014], whereas no thermal nonlinearity effects had been observed in this previous work because of the low detection frequency setup that had been used.

The main limitation of our work is the inability to observe photoacoustic thermal nonlinearity with the gold nanospheres solution at room or physiological temperatures. This could limit the potential *in vivo* applications. It should also be underlined that the experiments presented in this work were done with gold nanospheres diluted in water. Biological tissues might behave differently than water. To observe photoacoustic thermal nonlinearity at room or physiological temperatures, higher fluences could be used, in combination with the detection of higher photoacoustic frequencies. The use of higher fluences was tested with the setup presented in section 5.2.1, it was however observed that in these conditions the polycarbonate tubes would darken and deteriorate, thus perturbing the experiment. The polycarbonate tubes were therefore replaced by glass tubes of similar inner diameter. These new tubes could easily handle fluences of several tens of mJ cm^{-2} . However, for reasons that are not yet understood, the gold nanospheres solution was then modified when illuminated by light pulses at such high fluences. This was observed both visually, through a color change of the solution and with a spectrometer, through a modification of its optical absorption spectrum. Further studies are required to better understand the phenomenon at stake here. The detection of higher photoacoustic frequencies would require the use of a higher frequency transducer and probably of smaller diameters tubes for the signal-to-noise ratio to be sufficient at the high photoacoustic frequencies targeted. In the setup presented in section 5.2.1, the polycarbonate tubes were filled by use of a thin needle and a syringe. This technique proved to be difficult to use to fill very thin tubes of a few tens of micrometer of inner diameter. Another type of setup could be developed to enable the detection of thermal nonlinearity at high acoustic frequencies by use of a high frequency transducer and the detection of photoacoustic signals generated by small volumes of gold nanospheres. Experiments with biological tissues need to be done to study their behavior in regard to photoacoustic thermal nonlinearity. *In vitro* configurations would then benefit from their potential ability to control the temperature of the studied samples.

Conclusion

In this PhD work, results have been obtained on different aspects of photoacoustic imaging.

In the first part, the work was aimed at providing contributions for the development of optical-resolution photoacoustic endoscopy. Because this requires both to scan a focused spot at depth in the imaged sample and to detect the generated photoacoustic waves, we investigated these two aspects of the imaging process. Concerning the first aspect, we proposed to apply digital phase conjugation to scan a focused spot at the distal tip of a multimode fiber in the context of photoacoustic endoscopy. The digital phase conjugation technique was well mastered by Dr. Ioannis Papadopoulos, Dr. Salma Farahi, Prof. Christophe Moser and Prof. Demetri Psaltis at École Polytechnique Fédérale de Lausanne with whom we collaborated and adapted the technique to photoacoustic imaging. By use of digital phase conjugation optical-resolution photoacoustic images of a knot composed of two 30 μm diameter nylon thread were generated at the distal tip of a multimode fiber with a resolution greater than 1.5 μm over a $201 \times 201 \mu\text{m}$ field of view. This promising first step was however only achieved with the sample in water rather than biological tissues. Even if the technique could be used to generate an optical-resolution image at depth in a biological tissue, the detection of the generated photoacoustic waves would remain a challenge. Indeed, the acoustic attenuation in biological tissues is very strong at the high acoustic frequencies generated in optical-resolution photoacoustic imaging. We proposed to use a water-filled silica capillary as an acoustic guide to transmit the photoacoustic waves generated at depth inside a tissue to its surface for remote detection thus avoiding the strong acoustic attenuation inside the tissue. The ability of such a capillary to guide optical-resolution photoacoustic images through several centimeter of highly acoustically absorbing tissue was demonstrated experimentally. Experiments were carried out with an adapted setup to further characterize the guiding properties of the capillary, in particular its transmission efficiency. It was found that a strong attenuation took place during the

propagation of the photoacoustic waves in the capillary, resulting in a transmitted amplitude that decayed exponentially with the capillary length. A simple guided propagation model taking into account the viscosity of water predicted behavior and orders of magnitude concerning the losses in the tube that are compatible with the measured data. According to this model, the low-pass filtering and amplitude attenuation observed on the transmitted signals are due to viscous losses resulting from shear induced at the water/silica boundaries of the capillary tube. It was then further shown experimentally that a capillary tube could be used to guide *both* the excitation light on the way in and the photoacoustic waves on the way out, providing the first demonstration of remote photoacoustic sensing through a simple dual waveguide free of any optical or acoustical component at its imaging tip. This was however achieved without optical wavefront shaping, with a resolution therefore limited by the aperture of the capillary.

Because fiber bending compensation is still out of reach of wavefront shaping by digital phase conjugation, a rigid endoscope configuration should first be considered. Phase conjugation could be used to generate an optical-resolution photoacoustic image at the distal tip of a water-filled capillary thanks to its ability to guide light. This image could then be transmitted by the same capillary through a few centimeters of highly acoustically absorbing tissues for remote detection at its surface thanks to the ability of the capillary to guide acoustic waves. An optical-resolution photoacoustic image could thus most likely be acquired by this technique at depths of a few centimeters inside tissues. Work towards this objective is currently being done as a collaboration with the groups of Prof. Christophe Moser and Prof. Demetri Psaltis at École Polytechnique Fédérale de Lausanne. Some experiments and technological developments should be done first to optimize the ability of the capillary to guide both optical and acoustic waves and then to reduce the attenuation of the transmitted photoacoustic waves inside the tube while preserving the small footprint of the capillary. Slightly increasing the inner diameter of the capillary could for example reduce the acoustic attenuation of the transmitted photoacoustic waves. The capillary could also be considered as a liquid-core optical waveguide. A low viscosity liquid (649 Engineered Fluid, 3M Novec, USA, for example) could also be used to fill the capillary, although then probably requiring an appropriate sealing of the capillary core for *in vivo* imaging.

In the second part, two acoustic-resolution photoacoustic imaging setups were initially developed for small animal imaging. Some preliminary results were obtained, in particular with the setup based on a linear array probe and a commercial ultrasound scanner. Both

two and three dimensional images of absorbing samples embedded in optical scattering agar gels were acquired with the single element imaging setup. Tumors of living mice were then imaged with the linear array setup before and at different times up to 20 h after gold nanorods or gold nanoshells were injected in the mice tail veins. Although the tumors were clearly seen, no photoacoustic signal could be detected from the gold nanoparticles. It was verified, through direct intratumoral injection that they could be detected if at strong concentrations inside the tumor. The main reason why no photoacoustic signal could be detected from the gold nanoparticles after injection in the tail vein is most likely that almost all of the seven tumors imaged were necrotic as histology later revealed. One of the tumor was partially viable and probably irrigated by blood vessel as could be seen on the acquired photoacoustic images. On this tumor a slight increase of the photoacoustic signal was observed in some regions of the tumor after injection of gold nanorods in the tail vein, but further investigation would be required to confirm these preliminary results. Using an adapted version of the high-frequency photoacoustic-microscope developed initially for tissue characterization, we focused our work on the experimental investigation of photoacoustic thermal nonlinearity, to confront experimental results to theoretical predictions from an earlier PhD work. The amplitude of the photoacoustic signals generated by two aqueous solutions of organic dye and 40 nm diameter gold nanospheres of identical optical densities at the 532 nm illumination wavelength were compared and studied as a function of the illumination fluence and the solutions equilibrium temperatures. In qualitative agreement with theoretical predictions, the dependence of the photoacoustic amplitude with the equilibrium temperature allowed to discriminate between the two absorbing solutions, and for an equilibrium temperature 4 °C where the thermal expansion coefficient of water vanishes, a nonlinear relationship between the incident fluence and the photoacoustic amplitude was observed for the solution of gold nanospheres, while the relationship was linear for the organic dye solution. However, for equilibrium temperatures of about 20 °C, no nonlinear relationship could be observed between the photoacoustic amplitude and the incident, as opposed to what was suggested from theoretical simulations. This discrepancy was either due to the fact that the detection frequency was not high enough, as it had been predicted by the numerical simulations that the thermal nonlinearity effects would be the stronger at high frequencies, or to inaccurate predictions from the theory, for example because the assumption that the temperature is continuous at the gold/water boundaries is too strong.

The two acoustic-resolution imaging setups developed and tested can be improved. In particular, the single element transducer setup should be modified for the illumination to be scanned at the same time as the transducer in a reflection configuration. Such improvements have been initiated in the course of the PhD work, mostly based on different solutions already described in the literature, however further work is required to finalize an end-user prototype to perform experiments in tissue. Preliminary results not presented in the manuscript were obtained for the characterization of tissue lesion created with therapeutic ultrasound (see related presentations in appendix A). The linear array probe setup would need to be slightly modified to improve its efficiency for the tumors imaging study started during this PhD work. The illumination on the tumors has to be made more reproducible for measurements made at different times on the same mice. More importantly catheter should be used to ease the injection of gold nanoparticles and reduce the mice movements involuntarily induced during the injection that make the acquired images comparisons more difficult. Thermal nonlinearities should be investigated at higher illumination fluences and higher frequencies. Investigation at higher illumination fluences has been tried but for reasons not yet understood the gold nanospheres solutions were modified when illuminated by fluences higher than the ones used in this work. This very limiting issue should be investigated. The detection of high frequencies in the several tens to hundred of MHz would probably require not only the use of a high frequency transducer but also the detection of small volumes of gold nanospheres to limit the low-pass filtering effect associated with large absorbers volumes. Numerical simulation predictions also have to be further refined for example by taking into account the thermal interface at the water/gold boundaries. This is currently being done by a PhD student in our group. Photoacoustic thermal nonlinearities could finally be studied in biological tissue samples *ex-vivo* to determine whether thermal nonlinearity effects similar to those measured in water can be expected.

Appendix A

Publications and communications

A.1 Publications in international peer-reviewed journals

1. I.N. Papadopoulos*, O. Simandoux*¹, S. Farahi, J.-P. Huignard, E. Bossy, D. Psaltis, and C. Moser, "Optical-resolution photoacoustic microscopy by use of a multimode fiber", [Applied Physics Letters](#) 102, 211106 (2013).
2. O. Simandoux, A. Prost, J. Gateau, and E. Bossy, "Influence of nanoscale temperature rises on photoacoustic generation: discrimination between optical absorbers based on thermal nonlinearity at high frequency", [Photoacoustics](#) (in press).
3. O. Simandoux, J. Gateau, J.-P.Huignard, C. Moser, D. Psaltis, and E. Bossy, "Optical-resolution photoacoustic microscopy across thick tissue through an acoustic waveguide", [Applied Physics Letters](#) (in press).

A.2 International conferences as speaker

1. O. Simandoux, J.-M. Chassot, E. Fort, and E. Bossy "Development of an acoustic-resolution photoacoustic microscope.", Acoustics 2012, Nantes, France, April 23-27 2012.

¹*Equally contributing authors

2. O. Simandoux, A. Prost, and E. Bossy "Photoacoustic thermometry: influence of the absorbers on temperature measurements.", European Conferences on Biomedical Optics, Munich, Germany, May 12-16 2013.
3. O. Simandoux, A. Prost, and E. Bossy "Photoacoustic generation by gold nanospheres in the nanosecond regime: from the individual nanoparticle to ensembles of nanoparticles.", 3rd International Symposium on Laser Ultrasonics and Advanced Sensing, Yokohama, Japan, June 25-28 2013.
4. O. Simandoux, A. Prost, and E. Bossy "Dependence of photoacoustic amplitude-temperature curves with the absorbers and illumination conditions.", IEEE-International Ultrasonics Symposium, Prague, Czech Republic, July 21-25 2013.
5. O. Simandoux, I.N. Papadopoulos, S. Farahi, J.-P. Huignard, C. Moser, D. Psaltis, and E. Bossy "Feasibility of optical-resolution photoacoustic microscopy through a multi-mode optical fiber.", IEEE-International Ultrasonics Symposium, Prague, Czech Republic, July 21-25 2013.

A.3 International conferences as co-author

1. A. Prost, O. Simandoux, J.-M. Chassot, E. Fort and E. Bossy, "Photoacoustic microscopy of tissue lesions induced by high-intensity focused ultrasound", Acoustics 2012, 163rd meeting of the Acoustical Society of America, 8th meeting of the Acoustical Society of China, Hong-Kong, 13-18 May 2012.
2. A. Prost, O. Simandoux, and E. Bossy, "Non-Linear Generation of Photoacoustic Signals from Gold Nanospheres in the Thermoelastic Regime", European Conferences on Biomedical Optics, Munich Germany, May 12-16 2013.

A.4 National conference as speaker

1. O. Simandoux, I.N. Papadopoulos, S. Farahi, J.-P. Huignard, C. Moser, D. Psaltis, and E. Bossy "Microscopie photoacoustique avec résolution optique : nouvelle ap-

proche endoscopique.", Neuvième colloque national OptDiag, Paris, France, May 14-16 2014.

A.5 National conference, poster

1. O. Simandoux, I.N. Papadopoulos, S. Farahi, J.-P. Huignard, C. Moser, D. Psaltis, and E. Bossy "Microscopie photoacoustique avec résolution optique : nouvelle approche endoscopique.", poster, 9ème Journées Imagerie Optique Non-Conventionnelle, Paris, France, March 19-20 2014.

Bibliography

- P. Beard. Biomedical photoacoustic imaging. *Interface Focus*, 1(4):602–631, 2011. [viii](#), [ix](#), [3](#), [19](#)
- P. C. Beard, F. Perennes, and T. N. Mills. Transduction mechanisms of the fabry-perot polymer film sensing concept for wideband ultrasound detection. *Ieee Transactions on Ultrasonics Ferroelectrics and Frequency Control*, 46(6):1575–1582, 1999. [22](#)
- A. G. Bell. On the production and reproduction of sound by light. *American Journal of Science*, Series 3 Vol. 20(118):305–324, 1880. [7](#)
- I. G. Calasso, W. Craig, and G. J. Diebold. Photoacoustic point source. *Physical Review Letters*, 86(16):3550–3553, 2001. [27](#)
- A. M. Caravaca-Aguirre, E. Niv, D. B. Conkey, and R. Piestun. Real-time resilient focusing through a bending multimode fiber. *Optics Express*, 21(10):12881–12887, 2013. [50](#)
- T. Chaigne, O. Katz, A. C. Boccara, M. Fink, E. Bossy, and S. Gigan. Controlling light in scattering media non-invasively using the photoacoustic transmission matrix. *Nature Photonics*, 8(1):59–65, 2014. [23](#)
- Y.-S. Chen, W. Frey, S. Kim, P. Kruizinga, K. Homan, and S. Emelianov. Silica-coated gold nanorods as photoacoustic signal nanoamplifiers. *Nano Letters*, 11(2):348–354, 2011. [105](#)
- Y.-S. Chen, W. Frey, S. Aglyamov, and S. Emelianov. Environment-dependent generation of photoacoustic waves from plasmonic nanoparticles. *Small*, 8(1):47–52, 2012. [105](#)
- S. V. Egerev and A. A. Oraevsky. Optothermoacoustic phenomena in highly diluted suspensions of gold nanoparticles. *International Journal of Thermophysics*, 29(6):2116–2125, 2008. [27](#), [28](#)

- S. Farahi, D. Ziegler, I. N. Papadopoulos, D. Psaltis, and C. Moser. Dynamic bending compensation while focusing through a multimode fiber. *Optics Express*, 21(19):22504–22514, 2013. [50](#)
- W. Göbel, J. N. D. Kerr, A. Nimmerjahn, and F. Helmchen. Miniaturized two-photon microscope based on a flexible coherent fiberbundle and a gradient-index lens objective. *Optics Letters*, 29(21):2521–2523, 2004. [23](#)
- A. O. Govorov and H. H. Richardson. Generating heat with metal nanoparticles. *Nano Today*, 2(1):30–38, 2007. [16](#), [28](#)
- I. S. Grigoriev and E. Z. Meilikhov. *Handbook of Physical Quantities*. Taylor & Francis, 1997. [54](#), [55](#)
- P. Hajireza, W. Shi, and R. Zemp. Label-free in vivo grin-lens optical resolution photoacoustic micro-endoscopy. *Laser Physics Letters*, 10(5), 2013. [26](#)
- M. J. Holmes, N. G. Parker, and M. J. W. Povey. Temperature dependence of bulk viscosity in water using acoustic spectroscopy. *Journal of Physics: Conference Series*, 269(1):012011, 2011. [54](#)
- S. Hu, K. Maslov, and L. V. Wang. Second-generation optical-resolution photoacoustic microscopy with improved sensitivity and speed. *Optics Letters*, 36(7):1134–1136, 2011. [19](#)
- V. N. Inkov, A. A. Karabutov, and I. M. Pelivanov. A theoretical model of the linear thermo-optical response of an absorbing particle immersed in a liquid. *Laser Physics*, 11(12):1283–1291, 2001. [27](#)
- P. K. Jain, K. S. Lee, I. H. El-Sayed, and M. A. El-Sayed. Calculated absorption and scattering properties of gold nanoparticles of different size, shape, and composition: Applications in biological imaging and biomedicine. *Journal of Physical Chemistry B*, 110(14):7238–7248, 2006. [27](#), [113](#), [117](#)
- J. C. Jung and M. J. Schnitzer. Multiphoton endoscopy. *Optics Letters*, 28(11):902–904, 2003. [25](#)

- C. Kim, E. C. Cho, J. Chen, K. H. Song, L. Au, C. Favazza, Q. Zhang, C. M. Cobley, F. Gao, Y. Xia, and L. V. Wang. In vivo molecular photoacoustic tomography of melanomas targeted by bioconjugated gold nanocages. *Acs Nano*, 4(8):4559–4564, 2010a. 24
- C. Kim, K. H. Song, F. Gao, and L. V. Wang. Sentinel lymph nodes and lymphatic vessels: Noninvasive dual-modality in vivo mapping by using indocyanine green in rats—volumetric spectroscopic photoacoustic imaging and planar fluorescence imaging. *Radiology*, 255(2):442–450, 2010b. 20
- R. A. Kruger, R. B. Lam, D. R. Reinecke, S. P. Del Rio, and R. P. Doyle. Photoacoustic angiography of the breast. *Medical Physics*, 37(11):6096–6100, 2010. 18, 19
- L. D. Landau and E. M. Lifshitz. *Fluid Mechanics*. Elsevier Science, 1959. 54, 55, 74
- I. V. Larina, K. V. Larin, and R. O. Esenaliev. Real-time optoacoustic monitoring of temperature in tissues. *Journal of Physics D: Applied Physics*, 38(15):2633, 2005. 20
- M. J. Levene, D. A. Dombeck, K. A. Kasischke, R. P. Molloy, and W. W. Webb. In vivo multiphoton microscopy of deep brain tissue. *Journal of Neurophysiology*, 91(4):1908–1912, 2004. 25
- C. Li and L. V. Wang. Photoacoustic tomography and sensing in biomedicine. *Physics in Medicine and Biology*, 54(19):R59–R97, 2009. 16
- D. R. Lide. *CRC Handbook of Chemistry and Physics, 88th Edition*. Taylor & Francis, 2007. 105
- K. Maslov, H. F. Zhang, S. Hu, and L. V. Wang. Optical-resolution photoacoustic microscopy for in vivo imaging of single capillaries. *Optics Letters*, 33(9):929–931, 2008. 19
- I. McMichael, P. Yeh, and P. Beckwith. Correction of polarization and modal scrambling in multimode fibers by phase conjugation. *Optics Letters*, 12(7):507–509, 1987. 43
- Momentive. Mechanical properties of fused quartz. <http://www.momentive.com/products/main.aspx?id=20347>. 58, 76
- P. M. C. Morse and K. U. Ingard. *Theoretical Acoustics*. Princeton University Press, 1968. 58

- M. T. Myaing, D. J. MacDonald, and X. Li. Fiber-optic scanning two-photon fluorescence endoscope. *Optics Letters*, 31(8):1076–1078, 2006. [25](#)
- S. Y. Nam, L. M. Ricles, L. J. Suggs, and S. Y. Emelianov. Nonlinear photoacoustic signal increase from endocytosis of gold nanoparticles. *Optics Letters*, 37(22):4708–4710, 2012. [27](#)
- N. C. Nicholson and W. N. McDicken. Mode propagation of ultrasound in hollow waveguides. *Ultrasonics*, 29(5):411–416, 1991. [26](#)
- N. C. Nicholson, W. N. McDicken, and T. Anderson. Waveguides in medical ultrasonics: an experimental study of mode propagation. *Ultrasonics*, 27(2):101–106, 1989. [26](#)
- NIST. Nist chemistry webbook. <http://webbook.nist.gov/chemistry/>. [54](#), [58](#), [76](#)
- I. N. Papadopoulos. *Dynamic control of light transmission through multimode fibers*. PhD thesis, École Polytechnique Fédérale de Lausanne, 2014. [32](#), [36](#), [37](#)
- I. N. Papadopoulos, S. Farahi, C. Moser, and D. Psaltis. Focusing and scanning light through a multimode optical fiber using digital phase conjugation. *Optics Express*, 20(10):10583–10590, 2012. [25](#), [40](#), [41](#), [42](#)
- I. N. Papadopoulos, S. Farahi, C. Moser, and D. Psaltis. Increasing the imaging capabilities of multimode fibers by exploiting the properties of highly scattering media. *Optics Letters*, 38(15):2776–2778, 2013a. [41](#)
- I. N. Papadopoulos, S. Farahi, C. Moser, and D. Psaltis. High-resolution, lensless endoscope based on digital scanning through a multimode optical fiber. *Biomedical Optics Express*, 4(2):260–270, 2013b. [41](#), [42](#), [50](#)
- A. D. Pierce. *Acoustics: An Introduction to Its Physical Principles and Applications*. Acoustical Society of America, 1989. [54](#), [55](#), [74](#)
- M. Pramanik and L. V. Wang. Thermoacoustic and photoacoustic sensing of temperature. *Journal of Biomedical Optics*, 14(5):054024–054024–7, 2009. [20](#)
- A. Prost. *Photoacoustic imaging: application to ultrasound therapy control and generation by gold nanoparticles*. PhD thesis, Université Paris VI, 2014. [7](#), [27](#), [28](#), [103](#), [104](#), [105](#), [106](#), [107](#), [108](#), [109](#), [111](#), [112](#), [118](#), [121](#), [122](#)

- V. K. Pustovalov, A. S. Smetannikov, and V. P. Zharov. Photothermal and accompanied phenomena of selective nanophotothermolysis with gold nanoparticles and laser pulses. *Laser Physics Letters*, 5(11):775–792, 2008. [104](#)
- D. R. Rivera, C. M. Brown, D. G. Ouzounov, I. Pavlova, D. Kobat, W. W. Webb, and C. Xu. Compact and flexible raster scanning multiphoton endoscope capable of imaging unstained tissue. *Proceedings of the National Academy of Sciences*, 108(43):17598–17603, 2011. [25](#)
- D. Royer and E. Dieulesaint. *Elastic Waves in Solids I: Free and Guided Propagation*. Springer, 2000. [59](#)
- B. E. A. Saleh and M. C. Teich. *Fundamentals of Photonics*. Wiley, 2007. [38](#), [39](#), [43](#)
- J. Shah, S. Park, S. Aglyamov, T. Larson, L. Ma, K. Sokolov, K. Johnston, T. Milner, and S. Y. Emelianov. Photoacoustic imaging and temperature measurement for photothermal cancer therapy. *Journal of Biomedical Optics*, 13(3):034024–034024–9, 2008. [20](#), [24](#)
- C. Sheaff and S. Ashkenazi. A fiber optic optoacoustic ultrasound sensor for photoacoustic endoscopy. In *Ultrasonics Symposium (IUS), 2010 IEEE*, pages 2135–2138. [26](#)
- A. Shibukawa, A. Okamoto, Y. Goto, S. Honma, and A. Tomita. Digital phase conjugate mirror by parallel arrangement of two phase-only spatial light modulators. *Optics Express*, 22(10):11918–11929, 2014. [43](#)
- K. H. Song, E. W. Stein, J. A. Margenthaler, and L. V. Wang. Noninvasive photoacoustic identification of sentinel lymph nodes containing methylene blue in vivo in a rat model. *Journal of Biomedical Optics*, 13(5), 2008. [20](#)
- L. Song, C. Kim, K. Maslov, K. K. Shung, and L. V. Wang. High-speed dynamic 3d photoacoustic imaging of sentinel lymph node in a murine model using an ultrasound array. *Medical Physics*, 36(8):3724–3729, 2009. [20](#)
- T. L. Szabo. *Diagnostic Ultrasound Imaging: Inside Out: Inside Out*. Elsevier Science, 2004. [18](#), [54](#), [55](#), [58](#)
- L. V. Wang and S. Hu. Photoacoustic tomography: In vivo imaging from organelles to organs. *Science*, 335(6075):1458–1462, 2012. [viii](#), [ix](#), [19](#)

- L. V. Wang and H. Wu. *Biomedical Optics: Principles and Imaging*. Wiley, 2007. [17](#)
- J. Xu, X. Ren, W. Gong, R. Dai, and D. Liu. Measurement of the bulk viscosity of liquid by brillouin scattering. *Applied Optics*, 42(33):6704–6709, 2003. [54](#)
- J.-M. Yang, R. Chen, C. Favazza, J. Yao, C. Li, Z. Hu, Q. Zhou, K. K. Shung, and L. V. Wang. A 2.5-mm diameter probe for photoacoustic and ultrasonic endoscopy. *Optics Express*, 20(21):23944–23953, 2012. [24](#)
- J. Yao, K. I. Maslov, Y. Shi, L. A. Taber, and L. V. Wang. In vivo photoacoustic imaging of transverse blood flow by using doppler broadening of bandwidth. *Optics Letters*, 35(9):1419–1421, 2010. [24](#)
- M. K. Yapici, C. Kim, C. C. Chang, M. Jeon, Z. J. Guo, X. Cai, J. Zou, and L. H. V. Wang. Parallel acoustic delay lines for photoacoustic tomography. *Journal of Biomedical Optics*, 17(11), 2012. [26](#)
- E. Zhang, J. Laufer, and P. Beard. Backward-mode multiwavelength photoacoustic scanner using a planar fabry-perot polymer film ultrasound sensor for high-resolution three-dimensional imaging of biological tissues. *Applied Optics*, 47(4):561–577, 2008. [22](#)
- E. Z. Zhang and P. C. Beard. A miniature all-optical photoacoustic imaging probe. *Photons Plus Ultrasound: Imaging and Sensing 2011*, 7899, 2011. [26](#)
- E. Z. Zhang, J. G. Laufer, R. B. Pedley, and P. C. Beard. In vivo high-resolution 3d photoacoustic imaging of superficial vascular anatomy. *Physics in Medicine and Biology*, 54(4):1035–1046, 2009. [24](#)
- V. P. Zharov. Ultrasharp nonlinear photothermal and photoacoustic resonances and holes beyond the spectral limit. *Nature Photonics*, 5(2):110–116, 2011. [27](#)